ABSTRACT

SHA ZHANG. Study of Finite-Rate Chemistry Effects on Turbulent Jet Diffusion Flames and Non-homogeneous Autoignition Using the One-Dimensional Turbulence Model (Under the direction of Dr. Tarek Echekki).

In current study Numerical simulation of turbulent combustion process is approached using One Dimensional Turbulence (ODT) model to study the finite-rate chemistry effect in it. The ODT model is based on the coupling of molecular processes (reaction and diffusion) with turbulent transport in a spatially- and temporally-resolved fashion over a one-dimensional domain. The domain corresponds to a transverse (or radial) direction; while the transient evolution of the thermo-chemical scalars on the 1D domain represents the spatial evolution downstream of the jet inlet. The linear-eddy approach for modeling molecular mixing in turbulent flow involves stochastic simulation on a 1D domain with sufficient resolution to predict all relevant physical length scales properly. The finite-rate chemistry effect is investigated through hydrogen and air jet diffusion flame with helium dilution and hydrogen-air autoignition process using ODT model. Firstly ODT is carried out to study the fast chemistry effect, which dominates major species and temperature generation, and slow chemistry effect, which dominates minor species generation in jet diffusion flames. The comparison with existing experimental data was made for the numerical result of ODT simulation of jet diffusion flames in both conditional means and rms of scalars of measurements and computational results.

The finite-rate chemistry effect of transient problem involving chemistry is concentrated in non-homogeneous autoignition process of hydrogen-air turbulence flow. Another application of ODT was made in present work to verify the capability of prediction of autoignition (self-ignition) of one of free shear layer flow – jet diffusion flow. Different range of pressure and Reynolds number are set to identify the effects of turbulence intensity and mixture properties on the self-ignition chemistry. Autoignition delay time was studied based on these different conditions. At the same time the ability of the prediction of mixture temperature and species mass fraction profile were tested. A principle numerical result is expected and discussed. Conditional pdf and progress variable were used to analyze the computational result of ODT. Analysis was focus on the temperature growth and the mass fraction distribution of intermediate species and product.

Study of Finite-Rate Chemistry Effects on Turbulent Jet Diffusion Flames and Non-homogeneous Autoignition Using the One-Dimensional Turbulence Model

by

Sha Zhang

A thesis submitted to the Graduate Faculty of
North Carolina State University
in partial fulfillment of the
requirements for the Degree of
Master of Science

MECHANICAL AND AEROSPACE ENGINEERING
NORTH CAROLINA STATE UNIVERSITY

Raleigh, NC
2003

APPROVED BY:

Advisory Committee Chair

To

My Dear Parents,

Zhang, Shaoping

and

Lin, Li

BIOGRAPHY

Sha Zhang was born in Beijing, China and grew up there, got her bachelor's degree from Tsinghua University in China in 1999. She came to US to pursue advanced degree at the University of Kentucky, Lexington, in 2001 under the advisement of Dr. Jim M. McDonough in Department of Mechanical Engineering. Then she joined North Carolina State University to continue her study and research on MS degree in August 2002 under the advisement of Dr. Tarek Echekki. She worked on turbulent combustion simulation and computational fluid dynamics field in the two year's graduate study. She graduated in August 2003 with her master degree.

ACKNOWLEDGEMENTS

I would like to thank so many people for helping me in the construction of my master's degree. Firstly I would like to thank my advisor, Dr. Tarek Echekk for his invaluable guidance, motivation, encouragement and giving me the great opportunity to work with him. I want to thank Dr. Kevin, M. Lyons and Dr. Andrey V. Kuznetzov for serving on my advisory committee. Also, I am grateful to Dr. Jim M. McDonough, the advisor of mine when I was in University of Kentucky, who gave me a lot of help and instruction in my research.

I want to express my deepest gratitude to my parents and my brother, who have always been there with love and support for me. Thanks for always believing in me and always helping me through any tough time. Also thanks to my friend, Peng Geng. You are so kind, patient and understanding to me. Without your help I could not finish my study here. And all the friends standing with me, whether you are in Raleigh, Lexington, or China I can feel your love and friendship and remember it for ever.

Table of Contents

List of Tables

List of Figures

Chapter 1

Introduction

1.1 Overview

Fossil fuels remain the significant source of energy for domestic heating and power generation, particularly in transportation, and the combustion of fossil fuels is still a key technology for the foreseeable future. It is well known that combustion not only generates heat, which can be converted into power, but also produces pollutants such as oxides of nitrogen (NO_x), soot, and unburnt hydrocarbons (UHC). Even more stringent regulations are forcing manufacturers of automotives and power plants to reduce pollutant emissions, for the sake of our environment. These emissions will be reduced by improving the efficiency of the combustion process, thereby increasing fuel economy. Moreover, emissions of CO_2 are believed to contribute to global warming. It is, therefore, important that we understand the mechanisms of combustion and, for the reasons listed below, the role of turbulence within this process.

In technical processes, combustion always takes place within a turbulent flow field because turbulence increases the mixing process and enhances combustion. At the same time combustion releases heat, which generates flow instability through gas expansion and buoyancy, thus enhancing the transition to turbulence. This provides sufficient reasons to emphasize turbulent combustion in combustion research. Investigations of turbulent combustion reveal a noticeable gap between fundamental and applied research. The fuel

combustion devices have reached high levels of development and further improvement of their performance is not feasible without thorough analysis of the fluid dynamic features of combustion chambers, in particular, the characteristics of turbulence in these devices. On the other hand, the theory of turbulence has lately progressed considerably. Naturally, an adequate quantitative description of all turbulent flows is not presently available. However, the available qualitative understanding of many features of turbulence, and the accumulated experimental data and dimensional considerations allow sufficiently accurate estimates to be made of the characteristics of turbulence in a wide class of flows. Furthermore, many features of the combustion of gases in laminar flow are well understood. Therefore, there is increasing opportunity to understand the important mechanism of turbulent combustion.

In general, with regard to turbulence alone, three main classes of numerical analysis methods are currently being studied: *i*) direct numerical simulation (DNS); *ii*) large eddy simulation (LES); and *iii*) Reynolds averaged Navier-Stokes (RANS) approaches. When chemistry is to be considered we must also a combustion sub-model, such as the laminar flamelet model, conditional moment closure (CMC), or Monte-Carlo PDF methods, among others.

Several methods have been proposed to account for turbulent flows in one or more combination of above models. One such method is the large-eddy, laminar flamelet model (LELFM) of Cook, *et al.* (1997). In this approach a filtered mixture-fraction and filtered dissipation rate are resolved using LES at each LES grid cell. The model filtered the data from DNS of turbulence in prediction of non-premixed reacting flows. A similar approach

using filtered DNS data and LES result combined with the LELFM to predict non-premixed turbulent combustion is represented by Bruyn Kops and Riley (1999). A methodology termed the "filtered density function" (FDF) (Colucci, Jaberi & Givi 1998) is developed and implemented for LES of chemically reacting turbulent flows by including the effect of chemical reactions in a closed form in a derived transport equation of FDF. Another application of CMC for LES of non-premixed turbulent reacting flows was tested against DNS data (Bushe & Steiner 1999), in which closing chemical source terms in filtered governing equations of motions is proposed. The filtered means of the chemical source terms are obtained by integrating their conditional filtered means over the filtered density function of the conditioning variables. The various alternatives currently available for solving problems in turbulent combustion have been covered with a fair degree of thoroughness in the recent monograph by Peters (2000) adding to the existing literature of this topic as found, *e.g.*, in Libby & Williams (1994) and elsewhere.

1.2 Introduction to the One-Dimensional Turbulence (ODT) Model

Turbulent combustion usually involves a strong coupling of fluid mixing and chemical reaction. Turbulence is unsteady, three-dimensional, and covers a wide range of length and time scales. The difficulty of treating turbulence and detailed chemistry simultaneously cannot be overstated. Both phenomena, separately, are extremely difficult to simulate. Traditionally, the strategy of modeling turbulent mixing have concentrated on the large scales where most of the energy resides and implemented more simplified descriptions of the fine scales. In fact this approach is more difficult to apply to turbulent combustion. It

focuses on large time and length scale solely, which give a critical limitation in the models of turbulence-chemistry interaction, which are coupled to traditional turbulence modeling approaches.

Recently, representation of three-dimensional (3D) turbulent flows by models of lower spatial dimensionality has proven to be an effective method for obtaining reduced descriptions of turbulence (Kerstein 1989). Useful 2D formulations may include the 2D Navier-Stokes and Euler equations and the discrete-vortex model. Most current turbulent models are based on a 2D solution, which is much cheaper than 3D computation and have relatively similar acceptable results. Then 1D formulations have been proven useful, though a little narrower in scope. One-dimensional models describe the time evolution of ensemble-averaged statistical quantities, analogous to higher dimensional moment-closure methods. 1D representations of the evolution of individual flow realizations have also been formulated. Chekhlov (1995) obained the Kolmogorov turbulence driven by one-dimensional randomly forced Burgers equation, where the experimental data based on 3D turbulence is surprisingly similar to the result obtained from the simple one-dimensional formulation. Earlier, a 1D version of the Biot-Savart formula governing inviscid flow evolution has been formulated and has reproduced important features of 3D flow (Constantin, Lax & Majda 1985). A later formulation to the viscous flow and the application to the numerical computation of 3D flows were represented (De Gregorio 1990). These investigations reveal the possibility of 1D formulation of turbulence modeling, and for turbulent combustion.

The linear-eddy model (LEM), introduced by Kerstein (1988) is an earlier development based on 1D formulations turbulence model, which likewise involves temporally and spatially fully resolved simulation of the coupling between mixing and chemistry at all scales. The model is based on a deterministic formulation for molecular processes (molecular transport of scalars and chemistry) on a 1D domain, implemented concurrently with a random sequence of stirring events representing turbulent eddies. In the LEM, flow properties are specified empirically by assigning parameters governing the random event sequence. However, there is no provision for feedback of local flow properties to the random process governing subsequent events. This model has been successfully implemented for a wide variety of applications involving mixing in shear flows (Kerstein 1991A, 1992, McMurtry, Menon & Kerstein 1992). Another application of LEM is investigated in the microstructure of diffusive scalar mixing fields (Kerstein 1991B). The model captures many key features of turbulent mixing in micro-structure. Kerstein believed that many properties of the flow, such as single-point scalar properties, spectral and higher-order multipoint scaling properties, fractal geometry and Lagrangian scaling, can be treated as various manifestations of a single postulated scaling property of high-Reynolds number turbulence. Similarly, the LEM has been tested in turbulent combustion simulations with other combustion sub-models (Desjardin & Frankel 1996, 1997), which shows great agreement with the result of other models, such as Stationary Laminar Flamelet Model (SLFM) and Conditional Moment Closure (CMC) method.

In contrast, One-Dimensional Turbulence (ODT) model (Kerstein 1999A), which is an out-growth of LEM formulation, is a self-contained formulation that captures this feedback

with minimal empiricism. As an outgrowth of the LEM, ODT maintains the distinct implementation of turbulent stirring and molecular diffusion and reaction on a 1D domain. But ODT has the distinction from the LEM in the solution of the components of the velocity vector, which provides information about the shear field, thereby a mechanism for driving the turbulence. Therefore, ODT is not only a mixing model but also a methodology for fully resolved simulation of pure mixing, chemical reaction, and related scalar processes in turbulence. This is the key feature that distinguishes the ODT model from other conventional turbulence models that require the incorporation of mixing sub-models in order to treat scalar processes.

A distinct feature of ODT is at a wide range of phenomena may be addressed within a simple framework involving minimal empiricism with a very limited number of model parameters. Many normalized properties are insensitive to the value of these parameters. On the other hand, ODT is a fully resolved model, which set a broader range of statistics than conventional closure methods, such as single-point and multipoint moment of any order, multivariate probability density functions, conditional statistics, power spectra, Lagrangian statistics and *etc*.

ODT prediction of shear flow and buoyant stratified flows was implemented by Kerstein (1999A). This study illustrated the extension of the application of ODT capability for different flows, in addition to shear-driven flows. For buoyancy-driven flows with no applied shear, Monin-Obukhov similarity, important features of double-diffusion convection (Kerstein 1999B) and associated properties are reproduced with ODT. The

computed fluxes across heat-salt and salt-sugar interfaces reproduced the experimental observation of a variable regime in a single flow realization, which has not previously been achieved computationally or experimentally. Accordingly, it is verified that ODT can be used to decouple multi-component diffusion effects, applied shear, property variation, and related flow and fluid properties that happen in many technological and naturally turbulent combustion.

Recently Echekki, *et al.* have applied ODT to the temporal simulation of simple reacting mixing layer flows, such as jet and shear layers in hydrogen or methane flames (Echekki, Kerstein, Dreeben & Chen 2001, Zhang & Echekki 2003). Moreover, they reproduced the extinction and re-ignition in piloted methane jet diffusion (Echekki, Kerstein & Chen 2003) flames as well. All the applications reveal good agreement with experiments.

1.3 Scope of the Present Work

The present study will explore in more detail one key important feature, and at the same time a common key deficiency in existing turbulent combustion models, which is the prediction of finite-rate chemistry effects in turbulent flames. Finite-rate chemistry effects are associated with the departure of important scalar statistics from the fast chemistry limit due to the coupling of chemistry and transport time and length scales. It is implicit in this statement that this coupling may also occur at length and time scales that are not resolved by a coarse-grained approach such as RANS or LES using a conventional closure model for combustion, such as the flamelet model or the CMC approach. The previous simulations

using LEM and ODT have demonstrated the ability of these models, which resolve all time and length scales in the continuum limit, to predict finite-rate chemistry effects. These effects may be associated with the concentration of NO at the inlet of a turbulent jet resulting from its chemistry, and molecular and turbulent transport. They may also be associated to important reductions in intermediates in a turbulent flame, leading to extinction, or the eventual evolution of a mixture to ignition. The studies that are outlined below illustrate the application of ODT to the prediction of finite-rate chemistry effects using two important applications: turbulent jet diffusion flames and the phenomenon of autoignition in non-homogeneous mixtures.

1.4 Turbulent Jet Diffusion Flames

The finite-rate chemistry effect on hydrogen jet flames, especially to nitric oxide (NO) is important from an environmental and industrial viewpoint. A detailed knowledge of NO formation mechanisms in simple turbulent jet diffusion flames, such as hydrogen-air flames, is of importance to predict and minimize NO formation in practical combustion devices. Our work has concentrated on hydrogen because of its relatively simple kinetics and its importance as a subset of any hydrocarbon chemistry.

Our approach has been to compare model results with experimental data from a set of well-documented hydrogen jet flames (Barlow 2003, Barlow & Carter 1994, 1996). These experiments have provided conditionally averaged temperature, major species, OH and NO data. We have made simulations of radial profiles at several corresponding stream wise

locations in an undiluted hydrogen jet flame with a jet Reynolds number of 10,000 and in two helium-diluted hydrogen flames with 20% and 40% dilution, respectively using the ODT model. Dilution with helium reduces the radiative fraction to low levels, allowing for independent evaluation of turbulence-chemistry sub-models.

1.5 Autoignition in Turbulent Diffusion Mixture

Autoignition (self-ignition) of non-homogenous mixtures plays a significant role in the turbulent combustion. While more and more progress has been recently made in coupling chemistry and fluid mechanics, such as turbulence and molecular transport, the study of the spatial & temporal evolution of autoignition sites is still lacking. Therefore, it is of interests to predict autoignition of hydrogen and air in convective and diffusion environment. Autoignition of hydrogen in non-premixed environments is a complicated process for which a thorough understanding is not yet available. The difficulty lies in the complex and evolving coupling of dominant chemistry and turbulent transport, and the variety of combustion modes present (autoignition kernels in diffusion-flame environment to propagating premixed flame fronts). In this process the fuel ignition is governed by low-to-high temperature chemistry.

Investigations of ignition in non-homogeneous media reveal that the complex interaction between detailed chemistry and transport is likely to play a significant role in the autoignition process. In many combustion devices, such as in diesel engine, autoignition is achieved by injecting a relatively cold fuel into hot oxidizer (usually air). Therefore, the

chemical events and turbulent mixing are strongly coupled, and both of them are of importance during the induction period. Moreover, ignition takes place in a spatially non-uniform mixture in which the characteristic flow time is expected to play an additional and essential role in the ignition event. This influence becomes especially significant for a non-premixed system due to the need for mixing. During the autoignition process of non-premixed turbulent flow, the ratio of the characteristic chemical time scale to mixing time scale changes significantly. The first stage of ignition is characterized by chemical chain branching reactions in the absence of heat release. In this stage, chemical reactions are slow compared to mixing during low temperature ignition process. The second stage leads to the subsequent high-temperature combustion stage, which is characterized by thermal runaway and the establishment of a premixed flame front, in which chemical reactions are fast compared to mixing and diffusion.

In the present study, the finite-rate chemistry effects on transient coupling between chemistry and transport is studied in non-homogeneous autoignition process using One-Dimensional Turbulence. ODT implementation has already been illustrated earlier. The capability to predict autoignition of a turbulent jet of hydrogen with air in a co-flow is investigated in the present work. An understanding of autoignition in the hydrogen-air system is relevant to more complex chemistry involving hydrocarbon fuels, such as diesel and aircraft jet engines.

Autoignition based on simple chemistry was studied previously by Mastorakos, *et al*. (1997) which revealed that autoignition always occurs at mixture fractions very close to the most

reactive mixture fraction. This mixture fraction corresponds to the required temperature, and always occurred at sites along the most reactive mixture fraction contour that had the lowest values of the dissipation rate of the mixture fraction. Kreutz, *et al*. obtained a similar result in a study of forced ignition (Kreutz & Law 1996). They showed that in a laminar non-premixed counter-flow configuration, the reduced two step mechanism can be used to obtain sufficiently accurate predictions of the structure and critical extinction and ignition for hydrogen heated-air system by less than 20% difference with detailed chemistry for the undiluted flames (Balakrishnan, Smooke & Williams 1995). In the present study, we will show that initial autoignition kernels reside in fuel-lean mixtures and at conditions of low dissipation rates.

Ignition delay time is of significant interests in certain ignition kernel (radical pool), which is dominated by several aspects such as temperature, scalar dissipation rate, as well as turbulence intensity. Hilbert & Thévenin (2002) found that the effect of the turbulence intensity on the ignition time is non-monotonic. At the same time Im, Chen & Law (1998) show at certain conditions turbulence variation has a very small effect on autoignition delay. It may be stated that, as ignition is a local event, for the wide range of initial turbulence fields studied, the ignition delay appears to be quite insensitive to the turbulence intensity. However, global statistics of the autoignition process may still be dependent on turbulent condition.

Blouch and Law (2003) studied the detailed effects of turbulence on the temperature of a heated air with cold hydrogen jet required in a counter-flow configuration, in which

turbulence is generated using perforated plates on both sides of the flow. Turbulence generation at fuel and air sides was found to produce noticeable effects on ignition temperature while turbulence generated only on fuel side yields little effect on ignition. It shows that in the second ignition limit (below 3-4 atm), the lowest turbulent intensity resulted an autoignition temperatures lower than laminar ones, while increasing in turbulence intensity leads to rising ignition temperatures. Similar trends of temperature in proportion to turbulent intensity are observed up to 7 to 8 atm as the extension of the second limit, although within this region the ignition temperature is higher than the laminar ones.

Recently, a simulation of *n*-Decane combustion and autoignition in a laminar premixed flame was performed (Bikas & Peters 2001). The attention is directed towards an accurate description of species relevant to pollutant formation and, low temperature effect was considered as well. The low temperature reaction mechanism reproduces different radicals and then leads to different dominant reaction compared with the high temperature reaction mechanism. This phenomenon is especially important for the autoignition model.

The primary scope of the present work is to study finite-rate chemistry effects on the autoignition process from ignition kernel formation to final burn-out of the mixture. Initially, ignition kernels are established without heat release based on build-up radical. Then high-temperature combustion follows with strong coupling between turbulent transport and reaction & diffusion. Finally ignition kernels evolve into propagating front which acted as premixed flames. In this non-homogeneous self-ignition process, turbulence

affects the ignition delay time. The ignition kernels locations and propagation are characterized by mixed temperature and mixture fraction as well.

1.6. Outline of the Thesis

This thesis is organized as follows. In the next chapter, the numerical methods are described. Then, ODT simulation results and comparisons with experimental data for jet diffusion flame are presented in Chapter 3. In particular, the results will be presented in terms of conditional means and rms of scalars, particularly for intermediate species, NO and OH. In Chapter 4, results from the autoignition simulations are discussed for different simulation conditions considered. These conditions include: a) homogeneous ignition studies to determine a mix of oxidizer preheat temperature and mixture pressure for the turbulent simulations, and 2) a set of turbulent simulations based on different oxidizer preheat temperatures, pressures, and jet Reynolds numbers. Results will be presented in terms of the evolution of conditional means and conditional probability density functions (PDFs) of temperature, species and the progress variable for different ranges of the mixture fraction, and at different stages of the autoignition process. Finally the conclusions are summarized in Chapter 5.

Chapter 2

Numerical Methods

The numerical simulation of both the jet diffusion flames – a simple reacting mixing layer flow and the autoignition of nonpremixed turbulent mixing flows are employed by ODT model.

A detailed description of One-Dimensional Turbulence model formulation is given in Kerstein (1999A) and Echekki, Kerstein, Dreeben & Chen (2001). The ODT model is based on deterministic implementation of molecular processes (reaction and diffusion) and turbulent advection in a time-resolved simulation on a 1D domain. It fully resolves the turbulent combustion temporally and specially by coupling the mixing and transport and the chemical reaction. The 1D domain corresponds to the transverse direction of mean flow rate. Here, molecular process, which includes reaction and diffusion, can be computed from the unsteady reaction-diffusion equations, which are continuous, momentum, energy and species equations. We will discuss these unsteady equations in the next subsection. For the turbulent advection, a stochastic implementation is used.

2.1 Governing Equations for Molecular Transport and Reaction

Governing equations for the stream wise momentum, species and energy (temperature) equation are solved using the unsteady planar boundary layer equations without the advection or fluctuating pressure terms, which will be addressed in the turbulent advection

processes in the following subsection. These governing equations can be applied to the mixing layer, Couette and channel flows. The flow type is determined by the initial and boundary condition.

The temporally-developing governing equations are the momentum equation:

$$\frac{\partial u}{\partial t} = \frac{1}{\rho}\frac{\partial}{\partial y}\left(\mu \frac{\partial u}{\partial y}\right), \tag{2.1}$$

the species equations,

$$\frac{\partial Y_k}{\partial t} = -\frac{1}{\rho}\frac{\partial}{\partial y}\left(\rho V_k Y_k\right) + \frac{\dot{\omega}_k W_k}{\rho}, \tag{2.2}$$

and the energy equations,

$$\frac{\partial T}{\partial t} = \frac{1}{\rho \bar{c}_p}\sum_{k=1}^{N} c_{p,k} Y_k V_k \frac{\partial T}{\partial y} + \frac{1}{\rho \bar{c}_p}\frac{\partial}{\partial y}\left(\lambda \frac{\partial T}{\partial y}\right) - \frac{1}{\rho \bar{c}_p}\sum_{k=1}^{N} h_k \dot{\omega}_k W_k. \tag{2.3}$$

In the above equations, u is the mixture stream wise velocity which is in the radial direction of the 1D domain; ρ is the mixture density; Y_k, V_k, h_k, $C_{p,k}$, ω_k and W_k are, respectively, the mass fraction, the diffusion velocity, the total enthalpy (chemical and sensible), the heat capacity, the production rate and the molecular weight of the kth species; T is the mixture temperature; λ is the mixture heat conductivity; $\bar{c}_p$ is the mixture heat capacity. The thermodynamic pressure, P, is assumed to be spatially uniform. The equation of state is:

$$P = \rho R T \sum_{k=1}^{N} \frac{Y_k}{W_k} \tag{2.4}$$

which can be used to compute the mixture density, ρ. Here, R is the universal gas constant.

The governing equations for the molecular transport and reaction are solved by using a simple splitting of the diffusive and reactive contributions to the unsteady term. The unsteady-diffusion term is integrated using forward Euler method with second order spatial finite difference method. Then the source term is integrated in time step by using a stiff solver for systems of ordinary differential equations. Transport properties and the reaction mechanism are computed by coupling the model to Sandia's CHEMKIN (Kee, Miller & Jeferson 1983, Kee, Warnatz & Miller 1983, Kee, Grar, Smooke & Miller 1985) chemical-kinetic package.

2.2 Turbulent Advection

Advective transport is implemented through two contributions on the 1D domain:

- Dilatation, which is implemented as grid stretching commensurate with density decrease due to heat release,
- Instantaneous stirring events, which represent turbulent advection.

In the current representation, dilatation is accompanied by an expansion of the computational cells on the 1D domain proportional to the density decrease. This process conserves mass on the 1D domain and contributes to the lateral growth of the jet. In the same time the scalar gradient and rate of shear is reduced as well. Prior to stirring events, the 1D domain is already regridded to a uniform grid using a second order interpolation scheme. In principle, dilatation occurs in both stream wise and span wise directions to the jet, although is only explicitly implemented in the span wise direction. Model parameters,

described later in this section, subsume some of dilatational effects in the stream wise direction in the context of an analogy between temporally and spatially evolving jets.

Turbulent advection is carried out stochastically with mapping events, each involving the application of a 'triplet map' to a randomly selected segment (eddy) of size $\hat{l}$ and left boundary location, $\hat{y}$, so that the triplet map is applied to the eddy of span range of $\left[\hat{y}, \hat{y}+\hat{l}\right]$ in the computed 1D scalar field. The triplet map is a conservative rearrangement event which consists of the replacement of 1D profile on the size $\hat{l}$ segment by three identical copies compressed to one-third of their original size as shown in Fig. 2.1. The middle copy is inverted to get the continuity value of the model in the new converted profile.

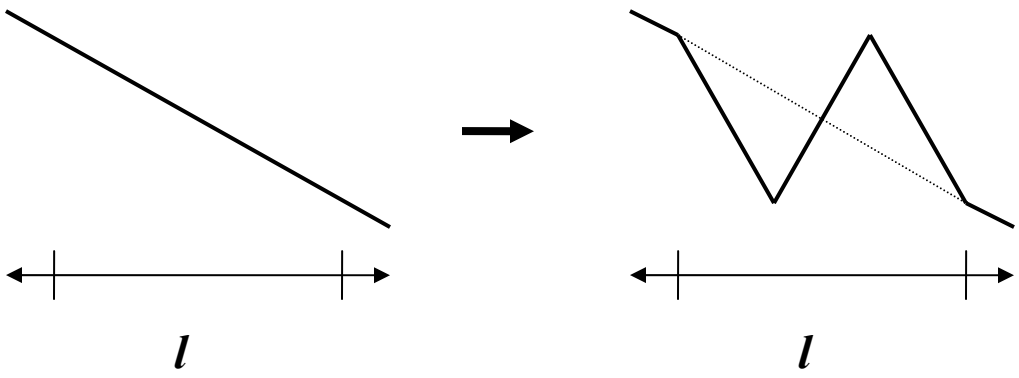

Figure 2.1 Triplet map events

The frequency of stirring events is governed by an eddy rate distribution:

$$\lambda_r\left(\hat{l};\hat{y},t\right)=\frac{1}{\hat{l}^2\tau\left(\hat{l};\hat{y},t\right)} \tag{2.5}$$

where $\tau\left(\hat{y},\hat{l};t\right)$ is a characteristic eddy time scale. Event parameters are selected by sampling from a rate distribution that is determined by associating the time scale $\tau\left(\hat{y},\hat{l};t\right)$ with every possible event at a given instant. τ is specified by the relation:

$$\left(\frac{\hat{l}}{\tau}\right)^2 = \left[A\left(U_L - U_R\right)\right]^2 - \left(\frac{\hat{l}}{\tau_d}\right)^2, \text{ where, } \tau_d = \frac{\hat{l}^2}{16\,\bar{\nu}}. \tag{2.6}$$

In this equation, τ_d represents a characteristic viscous diffusion time associated with an eddy of size $\hat{l}$. The eddy mean viscosity is expressed as

$$\bar{\nu} = \left[\frac{1}{\hat{l}}\int_{\hat{y}}^{\hat{y}+\hat{l}} \frac{dy}{\nu(y)}\right]^{-1}. \tag{2.7}$$

which corresponding to the effective viscosity of a lamellar variable-viscosity configuration. The first term on the right-hand side of Eq. (2.6) is a measure of shear the eddy experiences on the length scale $\hat{l}$. The characteristic velocities, U_L and U_R are averages over the left and right halves of the segment, $\hat{l}$:

$$U_L = \frac{2}{\hat{l}}\int_{\hat{y}}^{\hat{y}+\left(\hat{l}/2\right)} u(y,t)\,dy, \text{ and } U_R = \frac{2}{\hat{l}}\int_{\hat{y}+\left(\hat{l}/2\right)}^{\hat{y}+\hat{l}} u(y,t)\,dy. \tag{2.8}$$

Eq. (2.6) provides a mechanism for estimating the characteristic eddy turnover time, $\tau(\hat{l};\hat{y},t),$ that is used to compute the eddy rate distribution. It also contains one of two main parameters of the simulation, *A*, which relates the inverse of the rate of shear to the eddy characteristic time. The parameter, *A*, is of order unity. The viscous penalty (last term at the right-hand side of Eq. (2.6) provides a mechanism for the attenuation of small eddy stirring and turbulence in low shear regions. If the right-hand side of Eq. (2.8) is negative, then τ is taken to be infinite, which means the eddy events are prohibited. A similar mechanism for

the large eddies is also specified by non-stationary flows.

Another mechanism for exclusion of eddy stirring events is applied in the temporal simulation because of the non-stationary nature of the flow. In ODT model, a stirring event can be interpreted as the completion of an eddy turn-over. Therefore eddies with characteristic times, τ, that are long relative to the elapsed temporal evolution of the jet, t, are prohibited. Namely the acceptance criterion

$$t \geq \beta\tau \tag{2.9}$$

is adopted only. Here, β is another parameter of order unity, which must be specified in the model. The introduction of β is because the eddy lifetime scales is relevant with, but is not identical to, the inverse eddy frequency, τ. This condition prevents near-field implementation of relatively large eddy events for jets and shear-layers, which on average are characterized by longer eddy turnover times.

ODT model applies the temporal simulation with Eqs. (2.7) and (2.8) governing the random stirring events. This procedure is implemented numerically by a sampling process applied at a successive time step Δt_s. The choice for the time step is critical for several requirements. If Δt_s is too small, there is an extra cost for the calculation related to the over-sampling of eddy sizes and locations. At the same time, over-sampling causes a large number of stirring events prohibited by both viscous penalty and time history effects in non-stationary flows. On the other hand if Δt_s is too large it is more critical since under-sampling would result in an inaccurate numerical calculation in the physical model. We can follow Eq. (2.7) to evaluate the proper sampling frequency. Alternatively, there is a less costly implementation

including the "eddy number distribution" which is expressed in terms of guessed probability distribution functions (pdf's) for eddy parameters $\hat{l}$ and $\hat{y}$:

$$\lambda_r\left(\hat{l},\hat{y},t\right)\Delta t_s = p\left(\hat{l},\hat{y},t,\Delta t_s\right)f\left(\hat{l}\right)g\left(\hat{y}\right) \tag{2.10}$$

Here, $\hat{l}$ and $\hat{y}$ are guessed by sampling values from the pdf's f and g, respectively. In the turbulent flow, especially when the flow is not stationary, the total stirring rate requires an integration of the eddy rate distribution over the allowed ranges of $\hat{l}$ and $\hat{y}$. Therefore it is not known a priori. The integration repeated reconstruction of this rate distribution as the solution field evolves in time. From the Eq. (2.10), which presents one probability, p for the stirring event, the repeated adjustments of Δt_s are generated during the simulation based on the statistics of calculated values of p to maintain a target maximum probability. Here Δt_s must be chosen small enough to yield a value of p below unity. The algebraic form of f and g is not necessarily unique. In the current simulation for the jet diffusion flames, we still used the same distributions outlined in the original work on ODT:

$$f\left(\hat{l}\right) = B\hat{l}^{-2} \tag{2.11}$$

and $\hat{y}$ is chosen to be uniform everywhere. Here we should notice that both f and g should satisfy pdf normalization over the allowed ranges of $\hat{l}$ and $\hat{y}$.

In summary, the choice of f and g presents, and only presents the guesses of the actual distributions which are corrected by the rate of adjustment of eddies. It would not affect the actual size and location of stirring events which is determined by the initial and boundary

conditions of the specific problem. But, in the model the higher the sampling rate is, the more accurate is this predictor-corrector approach to eddy selection.

2.3 ODT Model Parameters

These two basic free parameters describe the characteristic flow in the temporal simulations of the reacting jet concurrently. Firstly, β assures the progressive growth of the mixing layer between the coflowing jets, while A determines the frequency of the stirring events (shown in Eq. (2.7)) and thereby the rate of entrainment and mixing in the jet. The viscous penalty gives a lower limit on eddy sizes comparing with the predominance of the viscous penalty term for small eddies while the time constraint, Eq. (2.9) limited the size of entraining eddies. In the near field, where self-similar profiles not developed, the limitation is especially strong. This time constraint is governed by the ratio of β to A. When β/A decreases, the limitation is looser.

The adjustment of these parameters is required to obtain the reasonable result of simulation when compares with experimental data. Key assumptions for the model are needed here for parameters adjustment.

- The model can be applied to a temporal flat jet diffusion model.
- Despite the thermal expansion can be in stream wise and transverse direction, only transverse (y) direction is considered in the implementation.
- The temporal evolution of one-dimensional profiles can be interpreted as a downstream evolution of radial profiles.

In addition to these assumptions, the choice of the value for the parameters also needs to match the height and initial evolution of major species in the hydrogen-air jet flame (Echekki, Kerstein, Dreeben & Chen 2001). No additional tuning of these parameters is attempted in current procedure from the simulation work by ODT before. The values of A and β are 0.344 and 1.45, respectively. The value of parameters has been verified to reasonably match the length scale of a number of turbulent diffusion flames including hydrogen-air jet diffusion flames, which we considered in present study. The present simulations and the ones presented in (Echekki, Kerstein, Dreeben & Chen 2001) suggest that the parameter, A, is important throughout the jet and governs the overall rate of mixing and entrainment. The parameter, β, is of particular importance in the first diameters of the jet and governs the growth of the shear layers.

2.4 Temporal To Spatial Mapping

The solution of the temporally developing planar jet is determined by the governing equations, (2.1) to (2.3), the implementation of the turbulent advection, and the initial and boundary conditions. Further requirements of comparison between computed and experimental results are related to (i) the choice of the model parameters A and β, and (ii) a mechanism for mapping temporal evolution to spatial evolution of the jet downstream.

Another important implementation for the jet diffusion flame study is that of temporal to spatial mapping of the 1D profile for ODT. Temporally developing jets and spatially

developing jets are fundamentally different generally for their different conserved integral quantities in two flows. In the former flows, the mass flux is conserved, while the momentum flux is conserved in spatially developing flows. But in constant density flows, both conserved mass flux and momentum flux produce the same scaling of the characteristic velocity decay with the same jet characteristic width. This dominant aspect provides the possibility to compare the result calculated from ODT for planar jets in temporal evolution to the existing experimental data for round jets in spatial evolution. However, in these two evolutions scaling is not maintained with heat release, which may introduce distinct mechanisms for transverse flow expansion in the two flow geometries.

For comparison with experiment, the temporal evolution of the jet is interpreted as a spatial evolution downstream of the jet exit. In ODT simulation, the 1D domain at a given time, t, is corresponding to a radial line at a downstream location, x, of the simulated round jet. The temporal-to-spatial conversion is then implemented with the following transformation:

$$x(t) = \int_o^t \bar{u}(t')dt' \tag{2.12}$$

Here, $\bar{u}$ is a uniform bulk velocity along the 1D domain expressed as the ratio of a momentum flux integral to a mass flux integral across the 1D domain:

$$\bar{u} - u_\infty = \frac{\int_{-\infty}^{+\infty} \rho(u - u_\infty)^2 dy}{\int_{-\infty}^{+\infty} \rho(u - u_\infty)dy} \tag{2.13}$$

where u_∞ is the free stream velocity. Based on this relation, the 1D domain is advected

downstream at a velocity, $\bar{u}$, which satisfies the initial conditions at the inlet of the jet. An additional mapping of the planar simulation to a cylindrical flow involves matching the ratio of fuel to pilot mass fluxes at the jet exit (i.e. initial conditions).

In the temporal evolution, all elements on the 1D domain have experienced the same chemical residence time which is not true for the corresponding spatial element at 1D domain, especially for those with slow chemistry and residing away from the jet centerline. To adjust this difference, the chemistry integration step, Δt_c is adjusted with the diffusion time step to adept the local residence time:

$$\Delta t_c = \Delta t_d \frac{u(y)}{\bar{u}} \tag{2.14}$$

2.5 Diagnostics

It is of advantage to use conditional statistics in the function of mixture fraction as a conditioning variable in non-premixed combustion analysis. Here we use a modified Bilger definition of the mixture fraction (Bilger, Starner & Kee 1990):

$$\xi = \frac{\left(Y_H - Y_{H,o}\right)/2W_H - \left(Y_O - Y_{O,o}\right)/2W_O}{\left(Y_{H,f} - Y_{H,o}\right)/2W_H - \left(Y_{O,f} - Y_{O,o}\right)/2W_O}$$

Where Y's are the elemental mass fractions, W's are atomic weights and the second subscripts, f and o, are corresponding to the fuel jet and oxidizer, respectively. Here, only species that were measured in the experiments are included in the mixture fraction

computation. Mixture fraction, which measures the extent of mixing information, varies from 0 to 1, which corresponding to oxidizer and fuel side, respectively. The stoichiometric condition of mixture fraction is the condition where mixture is in right proportion of fuel and oxidizer for complete combustion.

Conditional statistics (means and rms) are implemented for bins of mixture fraction. It allows the comparison of results of non-premixed turbulent flames with laminar flames. At the same time, conditional statistics are widely used for comparison with experiments and validation of combustion sub-models.

Chapter 3

Finite-Rate Chemistry Effect on Hydrogen-Air Jet Diffusion Flames

In current work, the finite-rate chemistry effect will be investigated in hydrogen-air with helium dilution jet diffusion flames by studying statistics of major species and temperature where profiles are governed by fast chemistry and NO statistics whose profiles are governed by its slow chemistry, thereby strong coupling between its chemistry and transport. Three different volume of helium dilution cases with corresponding different Reynolds number are represented in this chapter. The dilution effect on scalar statistics, in particular NO concentration varied with different volume of dilutions and turbulent conditions is focused. There are three different events of comparison taken in the following discussion: Comparison between different dilution volume, different downstream locations and computational results and available experimental data taken at similar condition.

3.1 Experiment Database and Implementation

In present study, the model is implemented to simulate the structure of a simple hydrogen-air jet diffusion flames with helium dilution in the fuel (Barlow 2003, Barlow & Carter 1994, 1996). The experiment was carried out for a range of flow conditions corresponding to the three dilution rates of 0% (flame A), 20% (flame B) and 40% (flame C) with different Reynolds number. The burner was a straight tube with a squared-off end (the inner diameter

of the nozzle is d = 3.75 mm, outer diameter d=4.84 mm). Flow and mixture conditions for the three flames are summarized in Table 3.1.

Table 3.1 Flow and mixture conditions of jet diffusion flames

Flame	A	B	C
H_2 : He (by volume)	100:0	80:20	60:40
Fuel jet Reynolds number (Re_d)	10,000	9,800	8,300
Stoichiometric mixture fraction	0.028	0.035	0.047
H_2O mole fraction in coflow air	0.0115	0.013	0.013
H_2O mass fraction in coflow air	0.0072	0.0081	0.0081

The coflow air velocity is 1.0 m/s with initial temperature at 294 K, and the flames were attached and unconfined. Average values of the H_2O mole fraction and mass fraction in the coflow during measurements in each flame are listed in Table 3.1, in which the different humidity ratio in the coflow is found varied for each flame in experiments. Since the ambient humidity affects NO production, it is important to include exact amount of H_2O in the simulation model.

The database of experiment includes simultaneous point measurements of temperature using Rayleigh scattering, concentrations of H_2, O_2, H_2O and OH using Raman scattering, and NO concentrations using laser-induced fluorescence.

3.2 Numerical Implementation

In the hydrogen-air jet diffusion flame simulations, nine species are included, which are: H_2, O_2, OH, H, O, H_2O, NO, He and N_2. The chemistry is based on a five-step reduced mechanism for hydrogen-air chemistry (Chen, Chang & Koszyknwski 1995). The global reaction mechanism is listed here as:

$O_2 + H = OH + O$ (R1)

$H_2 + O = H + OH$ (R2)

$H_2 + OH = H + H_2O$ (R3)

$H + O = OH$ (R4)

$O_2 + N_2 = 2NO$ (R5)

The temporal discretization of the governing equations (2.1)-(2.3) is based on full splitting of diffusion and reaction in which diffusion is advanced using the first-order Euler method, while the source term is integrated using a stiff-integrator DVODE(Brown, Byrne & Hindmarsh 1989). The boundaries of the ODT computational domain are maintained at free-stream conditions throughout the jet. The initial profiles of the thermo-scalars fields are generated using a 1D profile from the OPPDIF code (Lutz, Kee, Grcar & Rupley 1996) with matched fuel and air side mixture conditions.

When we compare the numerical result of jet diffusion simulation with experimental data the main focus is the assessment of the capability of ODT to model the role of dilution on the prediction of intermediate species, in particular OH and NO. The proper prediction of

major species concentration and temperature, especially the rms (root mean square) is of importance as well.

The 2D rendering results in spatial for flame (corresponding to temporal result in the model) is separate for each realization. We place the emphasis on the conditional statistics result of thermochemical scalars in turbulence combustion of present study, so that we need post processor to "average" the realizations. Generally, looking at statistics result of temperature and mass fractions of species is the most practical view to study. The post processor provides a means for clear visualization of results in ODT calculation result. Conditional statistics analysis is a useful tool for investigating the influence of turbulent mixing on thermochemical states in flames. Processing the conditional data on the instantaneous mixture fraction yields quantitative information on turbulence-chemistry interactions which cannot be extracted from time- or Favre-averaging approaches.

The experimental data is based on radial measurements of temperature and major and intermediate species at different downstream distances. The conditional statistics results are implemented from the radial scalar profiles in the experiment, and the numerical results of ODT in the simulations based on about 300 realizations to provide enough data to predict proper Reynolds-averaged conditional means and rms of all themochemical scalars. Rms simulation of scalars is of great significance in physical meaning in turbulent combustion analysis since it is a characteristic of fluctuation in the turbulence flow. Therefore, it is of importance for a turbulence model to simulate the rms of the flow properly. A handful of combustion sub-models produce rms statistics as part of model implementation.

3.3 ODT Computational Result and Comparison with Experimental Data

To compare easily and clearly between experimental and computational data, both results are set in same range and put in the same figure of all the figures shown in chapter 3 with experimental data in solid lines and ODT result in dashed lines. Because of the limitation of provided experimental data, scalar radial profiles of flame A and B at four different downstream locations, flame C at two locations are represented for both measurements and calculations in this paper. The adiabatic equilibrium results of temperature and NO concentration are also included in the corresponding scalar plots as reference. Except with special explanation the downstream locations shown for each flame are selected as listed in Table 3.2. Where d is the diameter of the tube (=3.75mm), L_v is the approximate visible flame length. L_{stoic} is the stoichiometric flame length along the jet centerline.

Table 3.2 Measurement conditions and comparison locations

Flame	Sreamwise locations (x/L_v)	L_v/d	L_{stoic} (mm)
A	1/8, 1/4, 3/8, 1/2	180	475
B	1/8, 1/4, 3/8, 1/2	150	375
C	1/2, 3/4	100	270

In the following discussion the numerical results of conditional means and rms of thermochemical scalars, including temperature and species concentrations of H_2, O_2, H_2O, OH and NO profiles in the function of Bilger mixture fraction for three flames are tested to against the available experimental radial profiles. ODT predictions of flow entrainment and finite-rate chemistry effects are discussed, which provides a measure of the model's

capabilities in modeling turbulent reacting jet diffusion flames.

3.3.1 Conditional Means of Scalars

Fig. 3.1 shows comparison between experimental data (in solid red lines) and ODT simulation result (dashed black lines) conditional means of the temperature profiles for flames, A, B and C. Equilibrium adiabatic flame temperature, which is in color dashed line, is also included in plots of each location for three flames. The ODT simulations are plotted against experimental data at the identical downstream locations. The results show a reasonable overall agreement between computations and measurements for temperature profile along the stream wise. Similar structures of temperature profiles were reproduced for three flames between the experimental value and computational result. The peak values of both series of data are lower than peak temperature at equilibrium conditions in particular at upstream locations of x/L=1/8 and 1/4. This difference is smaller at downstream locations where finite rate chemistry effects are less prominent. At the same time finite-rate chemistry effects increase by dilution volume, which show as difference between equilibrium and actual temperature values are larger in flame C than flame B, than flame A. This is because that more helium dilution in fuel deduces the hydrogen concentration which results in a slower reaction rate and lower peak temperature. In Fig. 3.1 the largest difference between the measured and calculated profiles occur near the nozzle of x/L =1/8, where the agreement between them is not as good as at downstream locations. At different flame distances temperature profiles of measurements are observed to cover different range of mixture fraction, which is decreased with the downstream

distance due to reactant burning out. The numerical results of ODT reproduce the almost same range of mixture fraction as experimental data in the same locations as shown in figures. Same phenomena can be found for temperature profile for flame B and C. In the very near field of flame B, the ODT result represents a small fluctuation for temperature profile where experimental value does not. Going further to downstream a better agreement between both compared data is shown. Same result can be found in flame B and C. It is apparent that helium dilution substantially reduces temperature peak value while shifting the location of it to larger value of corresponding mixture fraction due to the shifting of stoichiometric condition. However, three flames with different volume dilution are observed in similar shape of conditional means temperature profiles, which means dilution does not significantly affect flame temperature. Moreover, ODT reproduces of quantitatively and qualitatively the structure of temperature profile for different dilution cases.

Fig. 3.2 shows a similar comparison of conditional means of H_2O at same downstream distances as Fig. 3.1. The model yields reasonable predictions of conditional means of H_2O mass fraction in terms of general shapes of the correlations and peak values as well. The local maximum product generation is occurred at the value of mixture fraction in stoichiometric conditions, where maximum temperature is also happened. Although a little under-prediction can be found in computational result for near nozzle field (x/L=1/8 and 1/4), model almost captured perfectly experimental result in both magnitude and the shape for far field simulations in desired flames.

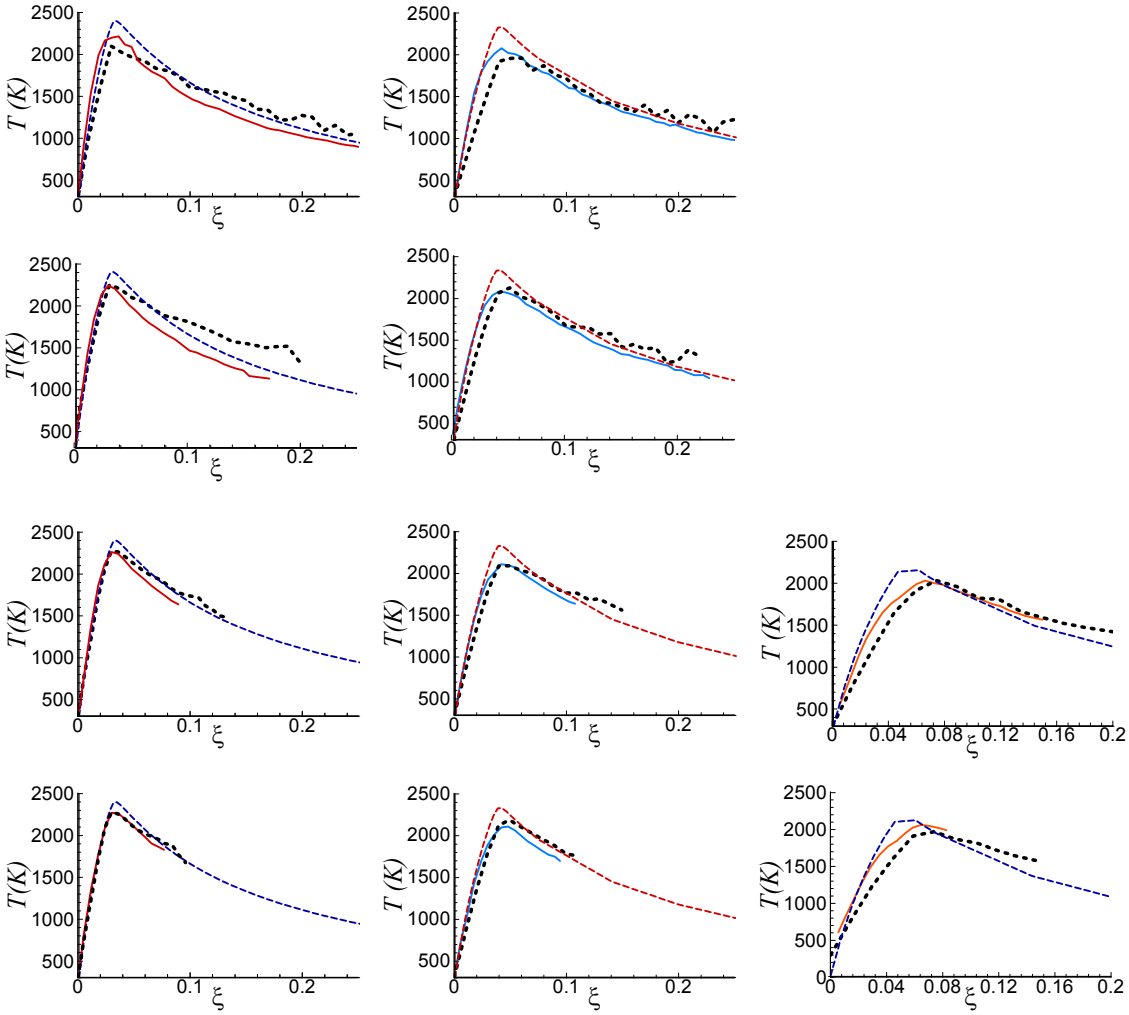

Figure 3.1 Conditional means of Temperature profile, ODT result against experimental data for flame A, B and C. (dashed line: ODT result; color solid line: experimental data; color long-dashed line: equilibrium adiabatic temperature)

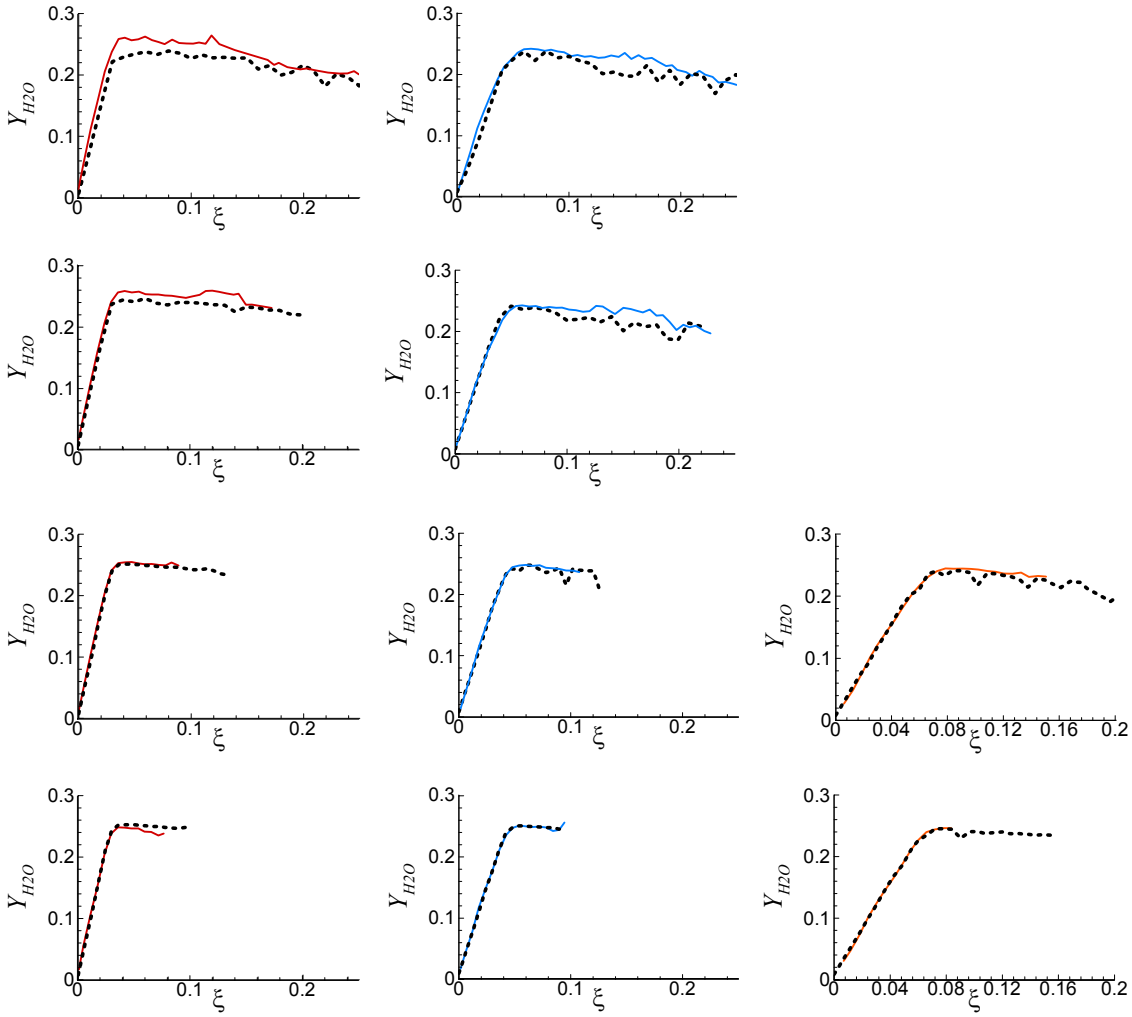

Figure 3.2 Conditional means of H_2O mass fraction profile, ODT result against experimental data for flame A, B and C. (dashed line: ODT result; color solid line: experimental data)

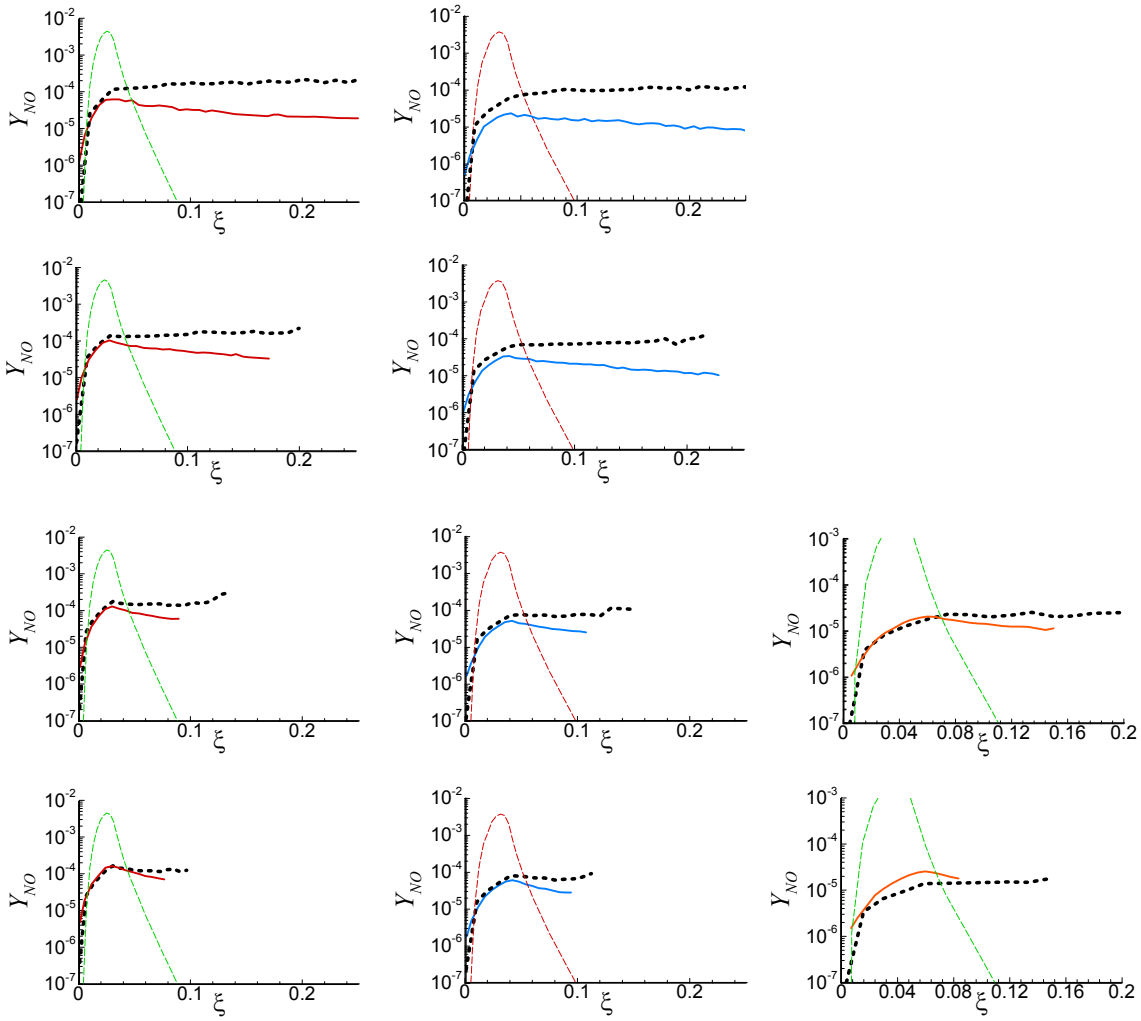

Figure 3.3 Conditional means of NO mass fraction profile, ODT result against experimental data for flame A, B and C. (dashed line: ODT result; color solid line: experimental data; color long-dashed line: equilibrium adiabatic temperature)

Next Emphasis would be placed on the intermediate species, in particular NO concentration in the function of mixture fraction. The sensitivity of NO production rate to local temperature, O atom concentration and residence times at the NO forming conditions makes NO a useful species for the evaluation of turbulent combustion models. The radial profiles of conditional means of NO mass fraction at different downstream distances of flame A, B and C are shown in Fig. 3.3. The adiabatic equilibrium NO mass fraction is also

included in plots as reference. Since NO formations are governed by slow chemistry actual result of NO concentration is much lower than the value in equilibrium condition, where finite-rate chemistry effect is more apparent than in major species.

Fig. 3.3 shows ODT results of NO mass fraction follows the experimental result at the very lean conditions, but over-predict the peak value of NO and the following quantity. This over-prediction is found mostly in the near field for both flame A and B. In overall view NO mass fraction has a higher jump in entire range of the simulation, which indicates that computed near field entrainment is faster than the experiment given the mapping from temporal to spatial evolution. In the other hand, computed NO mass fractions at further downstream of the jet exit are in better agreement with the experimental values, suggesting properly entrainment rates in the computations relative to the experiment in the far field. This is verified in computational value of NO in flame C, which shows a much improved agreement between computational and experimental value, since the location shown in flame C is x/L=1/2 and 3/4, which is equal or further than furthest locations shown in flame A and B. The computational results of flame A, B and C, particularly at the same distance x/L=1/2, indicates that helium dilution reduced NO formation. Here, NO production is associated with temperature, which decreases with dilution.

Simulation of the same flames was also carried out using CMC and PDF (Barlow, Smith, Chen & Bilger 1999), where radiation sub-model is included. Figs. 17, 18 and 12 in Barlow, *et al.* are corresponding to results listed in Fig. 3.3 of flame A, B and C, respectively. It is obvious that ODT result exhibits a better agreement with experimental data than in Barlow,

et al. result in conditional means of NO mass fractions prediction. Those models seriously under-predict the NO level in the whole range of upstream distance. The CMC and PDF simulation also under-predicted NO near the base of the flames at x/L=1/8. The authors attribute these under-predictions to the role of differential-diffusion effect, which is not presented in those CMC and PDF implementations but considered in current ODT model. The radiation effect has no contribution to this deficiency because the differences between the adiabatic and radiative results for each model are negligible at this upstream location. Moreover helium dilution also reduces the influence of flame radiation on NO formation. In current ODT model no radiation effect is considered, but the ODT models yields a reasonable prediction of NO concentration in near field. PDF model has problem in mixing model simulation and CMC model cannot produce rms prediction, where ODT will give out a reasonable rms simulation for all species particularly in intermediate species in the following part.

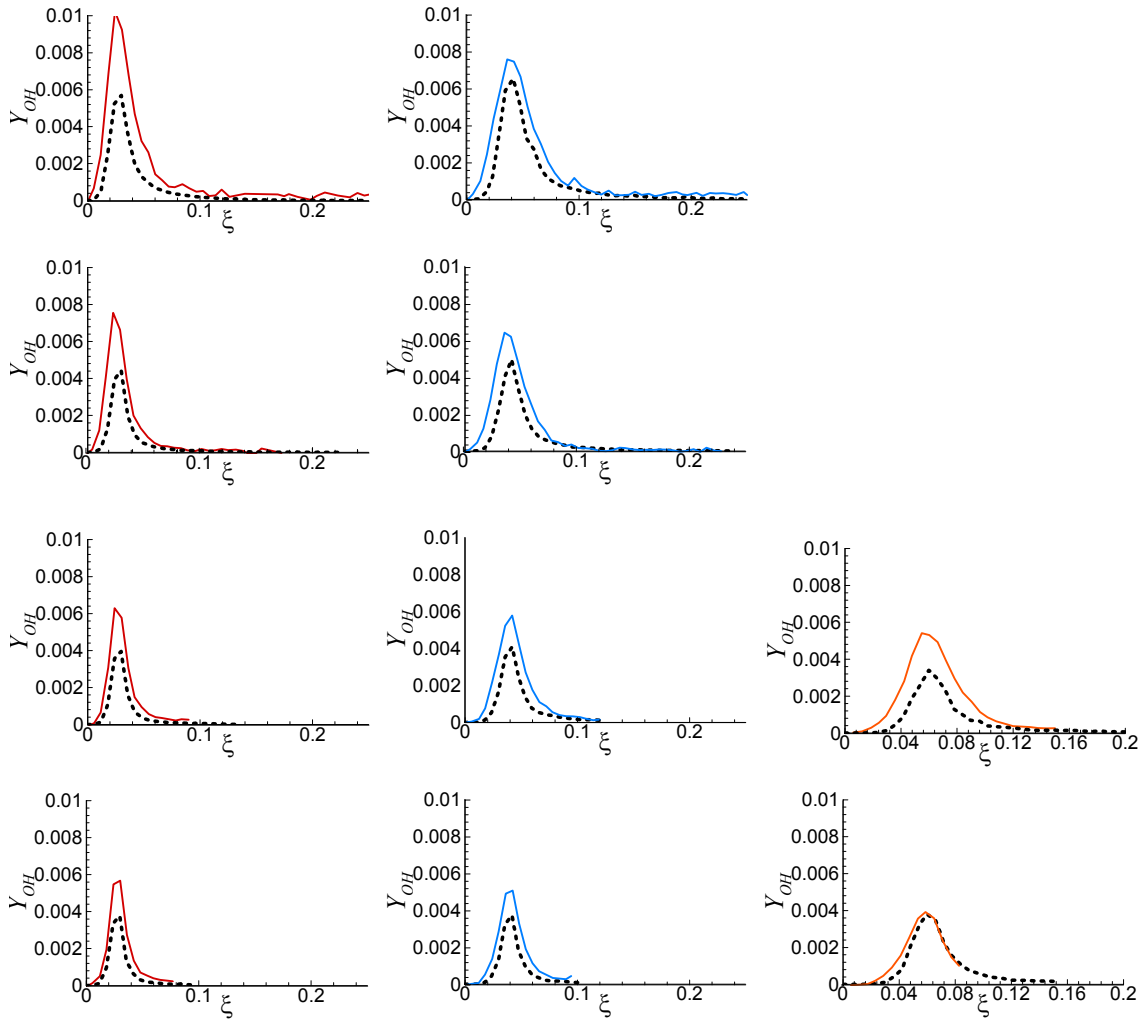

Figure 3.4 Conditional means of OH mass fraction profile ODT result against experimental data for flame A, B and C. (dashed line: ODT result; color solid line: experimental data)

Radial profile prediction of OH mass fraction for flame A, B and C is shown in Fig. 3.4. Figure shows that near the jet inlet, ODT does not capture accurately the magnitude of OH conditional means, in particular for flame A, but similar shapes are shown between computations and measurement. Again, prediction has improved in further downstream where ODT result shows a better agreement with experimental value. However, the shape of conditional means profiles of OH mass fraction is quite reasonable. The mixture fraction corresponding to the local peak value of OH mass fraction is consistent with the locations

where local peak temperature value is observed, where the most chemical activity exists. Therefore peak value of OH decreased with dilution as temperature decreased. OH levels decrease with downstream distance as well.

In Figs. 3.5 and 3.6 conditional means of reactants (H_2 and O_2) mass fractions for flame A, B and C are shown as a function of mixture fraction for different downstream distances. Fig. 3.5 shows good prediction in the computation for H_2 mass fraction. Both the experimental and computed means generated a reasonable trend for H_2. The figure shows that helium dilution reduces the peak H_2 mass fraction. Fig. 3.6 shows conditional means of O_2 mass fraction profile of flame A, B and C at different downstream locations. ODT results reproduce all experimental data at different flame downstream distance of each flame except in the near field of flame A and B, where the measurement of O_2 mass fraction show artificial increases in O_2 mean mass fraction, in particular for flame A. It is probably caused by experimental uncertainty for this unreasonable oxidizer concentration increasing in experiment. Here ODT simulation is more reasonable to maintain relatively decreasing profiles at such condition.

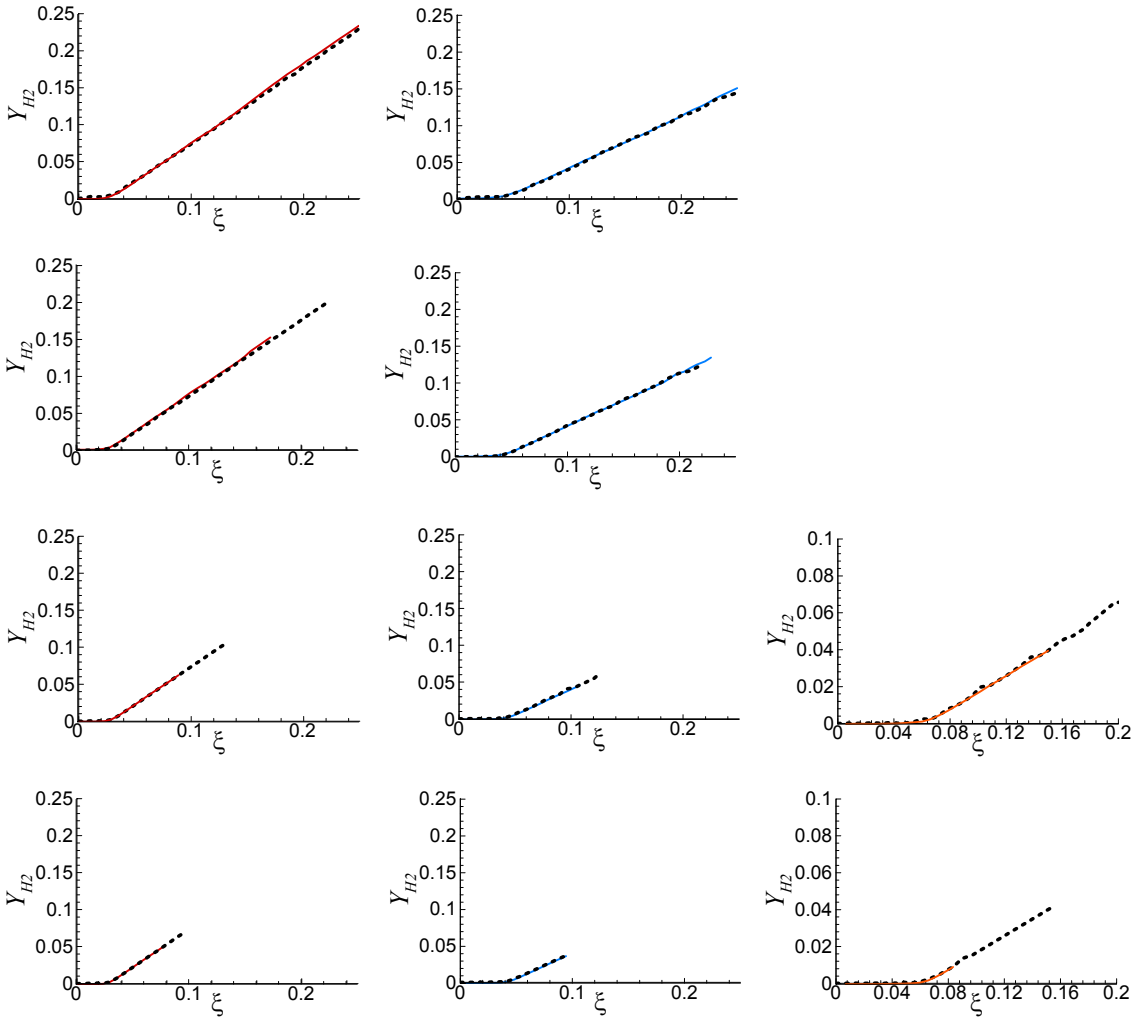

Figure 3.5 Conditional means of H_2 mass fraction profile, ODT result against experimental data for flame A, B and C. (dashed line: ODT result; color solid line: experimental data)

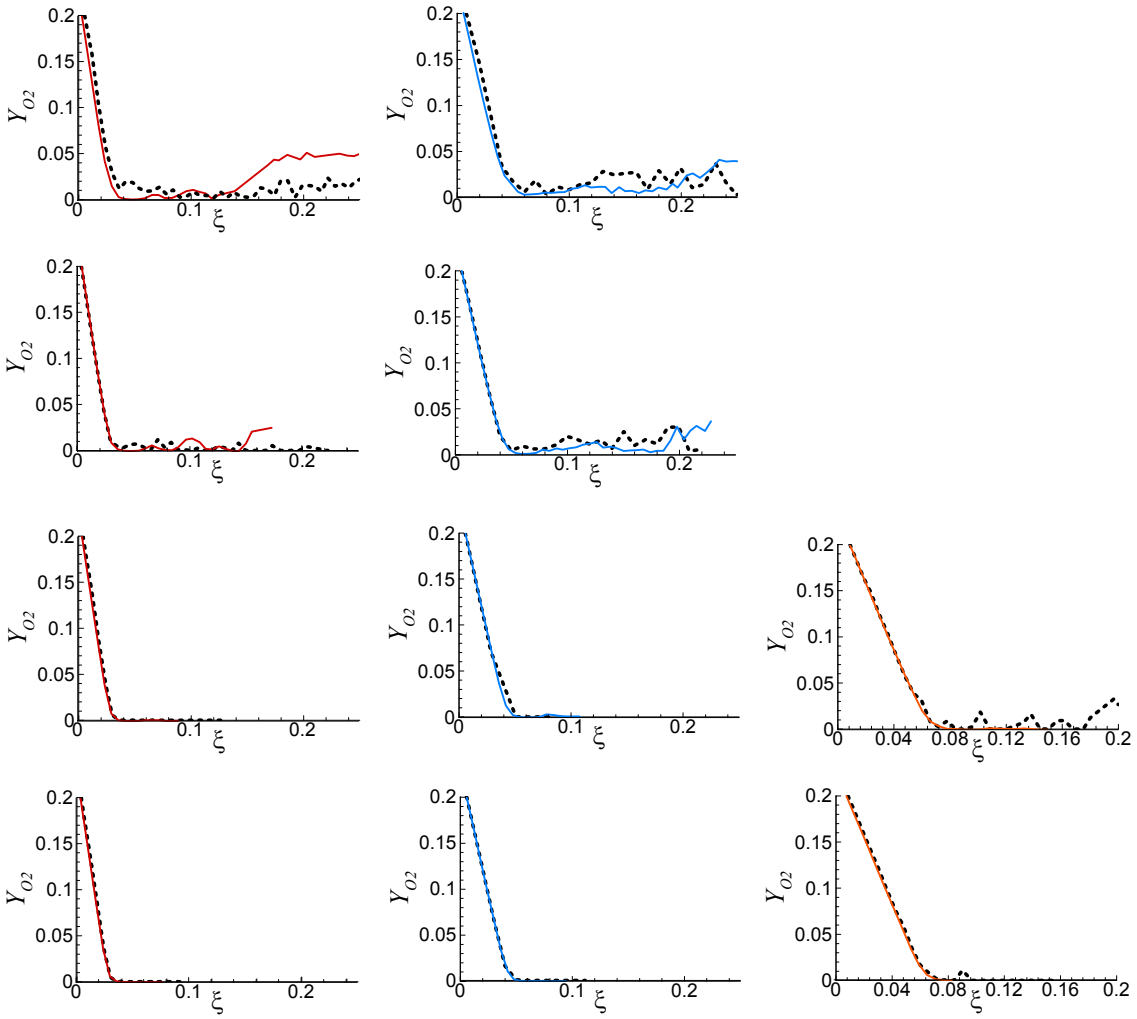

Figure 3.6 Conditional means of O_2 mass fraction profile, ODT result against experimental data for flame A, B and C. (dashed line: ODT result; color solid line: experimental data)

We have already studied the finite-rate chemistry effect on formation of temperature and intermediate species, which are governed by fast and slow chemistry, respectively. The capability of ODT model to predict the conditional means of scalars as a function of mixture fraction at different downstream location are tested as well. Generally speaking, agreements on the shape and magnitude of the conditional means scalar profiles are quite good for the range of dilution rates and downstream conditions. The calculation results indicate, neither in near field nor in far field, the mass fraction of reactive scalar profiles is

significantly different in magnitude at the different Reynolds number consideration and dilutions.

3.3.2 Conditional rms of scalars

As well as conditional means results provide straightforward path to learn about the scalar quantity and quality, conditional rms provides additional information about It shows the conditions of extinctions. It is few predicted by many of the state-of –the-art combustion models.

Fig. 3.7 shows the conditional rms of temperature profile as a function of Bilger mixture fraction for flame A, B and C. Both the experimental result (in solid line) and computational result (in dashed line) are shown in one plot for each downstream location. The similar magnitude is obtained in experimental and computational rms results. ODT result did not capture the local peak value of rms at most downstream distance as well as conditional means results. Some under-prediction for peak of rms is shown in temperature profiles, especially at the downstream locations. However, the overall agreement with measurements is reasonable. There are always some uncertainties in the experiments which lead to extra fluctuations in measurements. So that experimental result of rms is expected to be a little higher than actual fluctuations of flames. The temperature fluctuation is subject to this rule, particularly for the far field of flames. The peak values of the rms of temperature decrease with downstream distance, which is consistent with result of means. This is shown in both measurements and ODT results. In entrainment of flame A, a higher magnitude rms

is generated in ODT than experiments and two peaks are found in computational result. The first one is corresponding to large temperature gradient varying from initial to peak value. Near the stoichiometric conditions rms displays relatively lower value while second peak is responsible for temperature gradient after maximum value. A better agreement between ODT result and experimental data is shown in downstream locations for three flames.

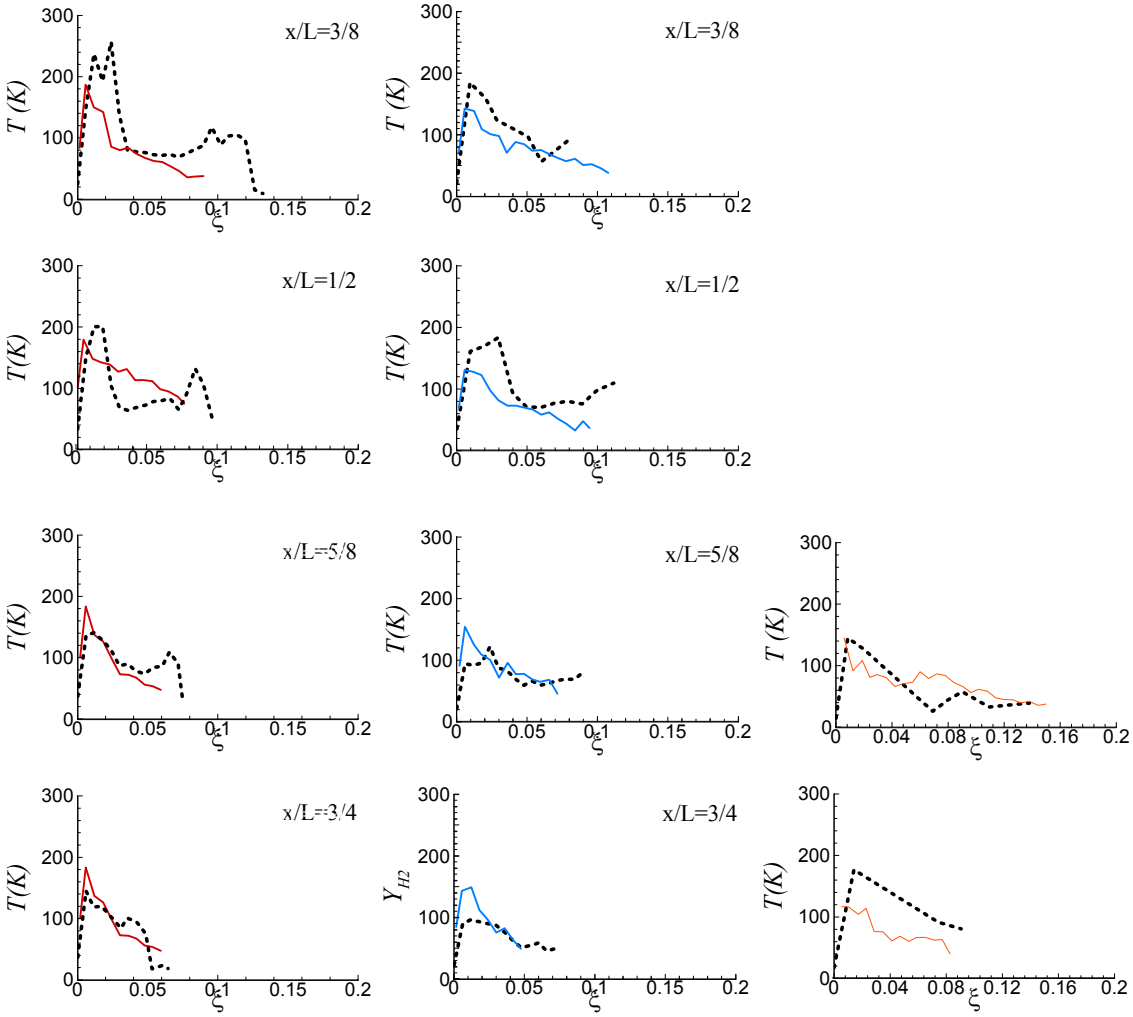

Figure 3.7 Conditional rms of temperature profile, ODT result against experimental data for flame A, B and C. (dashed line: ODT result; color solid line: experimental data)

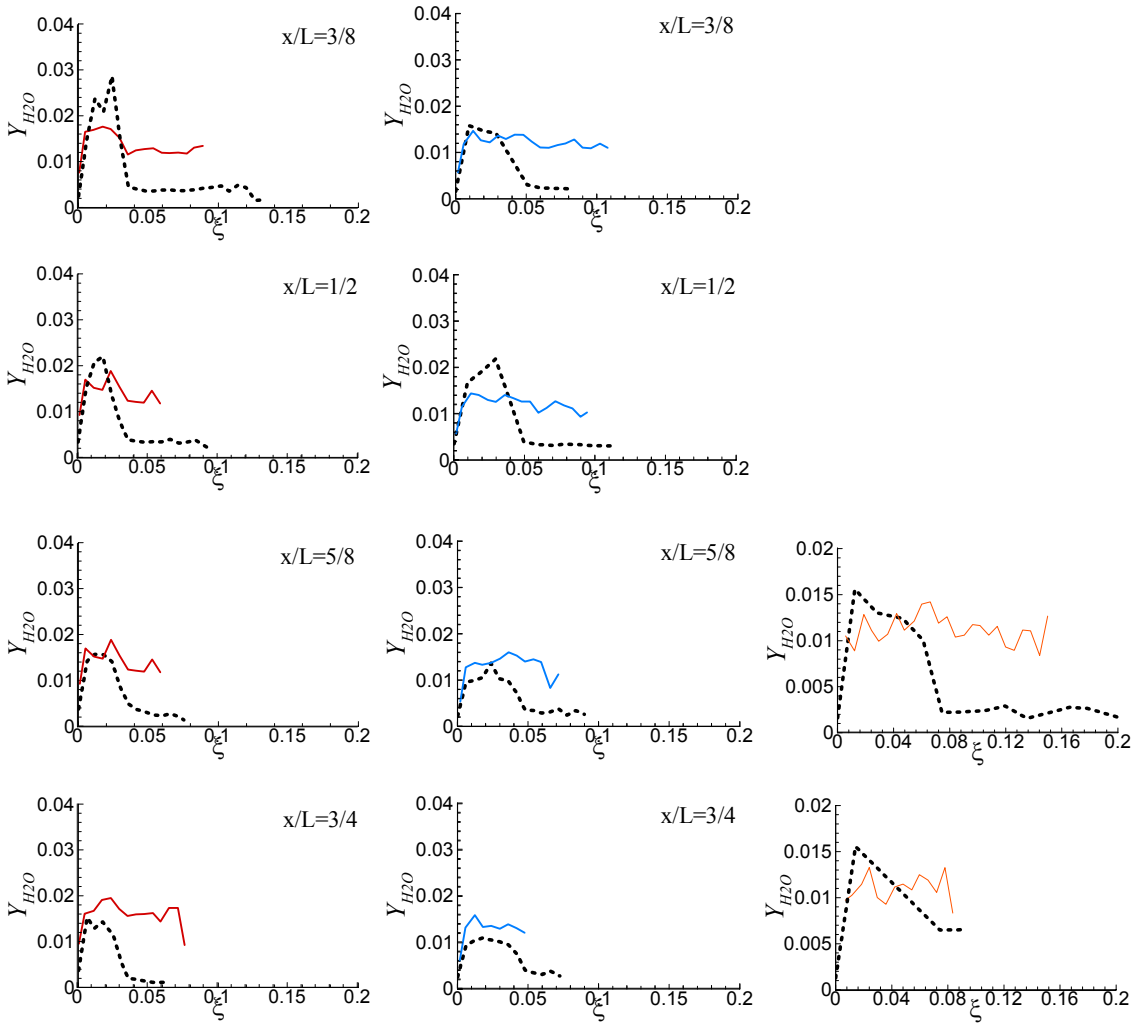

Figure 3.8 Conditional rms of H_2O mass fraction profile, ODT result against experimental data for flame A, B and C. (dashed line: ODT result; color solid line: experimental data)

Figure 3.8 presents a comparison between the computational and experimental results of the conditional rms of the H_2O mass fraction. As the primary product of hydrogen-air combustion, H_2O is representative of the major species, which displays a similar structure as temperature in either experimental or computational values. Again, in the base of flame A rms is not as well-predicted as in far field of downstream by ODT, particularly the over-estimated of the local peak value of rms. Agreement on the shape of rms H_2O mass fraction profile is quite good for flame B than flame A. This might be attributed to radiation effects

on diluted flames, which are not predicted with ODT. Moreover under-predicted of rms of H_2O mass fraction at all shapes in entire range f downstream distance would rather to be considered as a higher- calibration value in experiment, which is consistent with the temperature results.

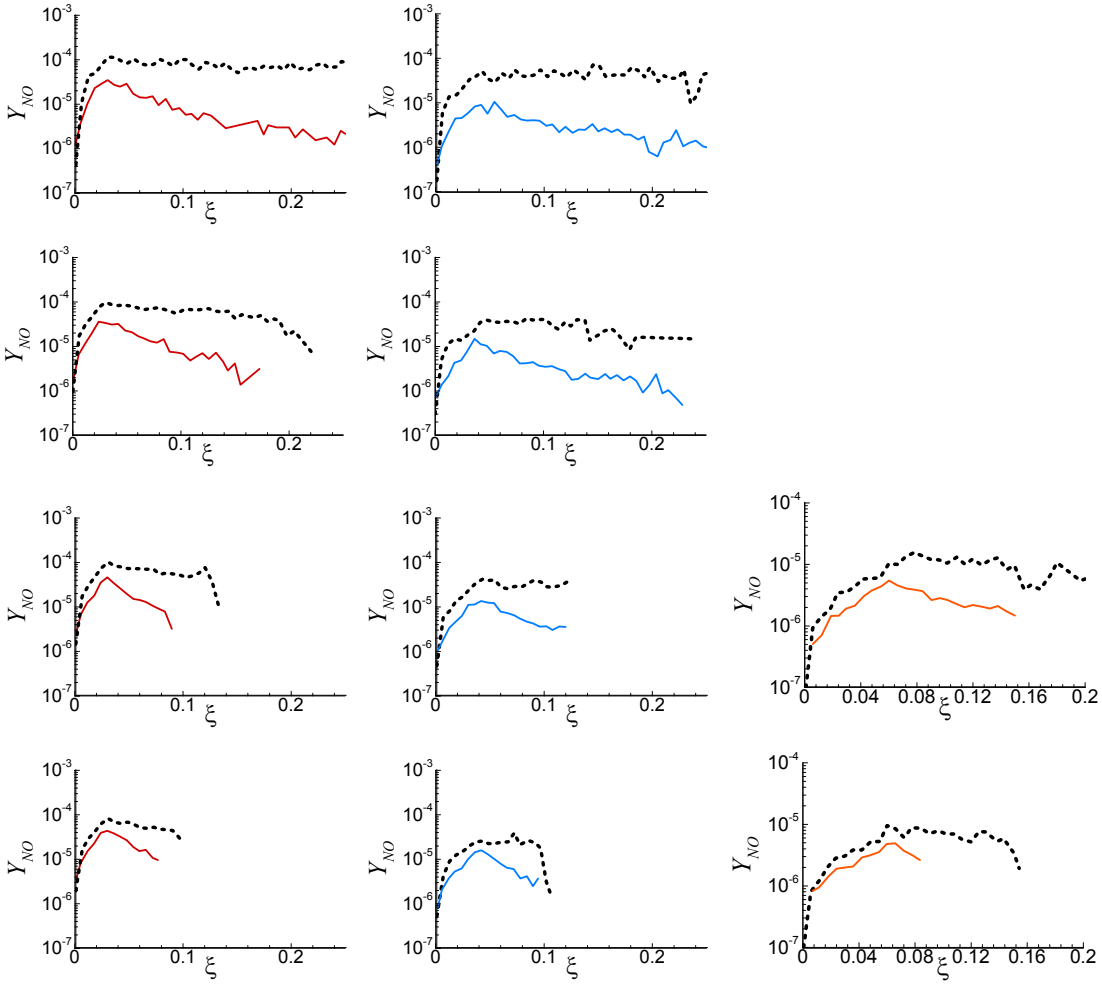

Figure 3.9 Conditional rms of NO mass fraction profile, ODT result against experimental data for flame A, B and C. (dashed line: ODT result; color solid line: experimental data)

Rms of NO mass fraction prediction is more in agreement with the measurements compare with previous scalar rms simulation results. Fig. 3.9 shows that computational results of rms NO mass fraction reproduce the general shape of measurements, but over-predicted them slightly except at very lean conditions. Again, at further downstream a better agreement is obtained. The prediction may be according to several correlations. First the ODT model of the residence time of NO may affect the final numerical result. At the mean time, although dilution reduces radiative loss, and as indicated in the publication of the experiment scalar data (Barlow 2003), in the most dilute case radiation has only a small influence on thermal NO production, radiation has still affected the NO production, particularly at the low dilution case. In the current ODT model no radiation sub-model is included. Therefore, some inaccurate prediction is expected from the computation. However, when we compare the ODT simulation result with the prediction in another paper (Barlow, Smith, Chen & Bilger 1999) which included a radiation sub-model, they did not even provide the rms result of NO, while poor simulation of means value is observed compared with ODT results of Fig. 3.3. Secondly, near field of flames is not predicted as good as far field using current 1D turbulence model. Then entrainment conditions, which include not only turbulent flows, are more complicated to predict properly than downstream distance.

Fig. 3.10 shows measured and computed conditional rms results of OH mass fractions for flame A, B and C at the same downstream conditions plotted above. The agreement between ODT and experimental data is satisfactory, including the evolution of OH profiles as a function of downstream distance. The calculation results capture the experimental value even better than the simulation of conditional means. Rms result of OH mass fraction

is consistent with the rule that maximum rms value corresponds to the maximum value of conditional means gradient. Furthermore, Fig. 3.10 shows that ODT is able to simulate the fluctuation of turbulent scalars, even for the intermediate species, which is with more difficult to capture the small magnitude.

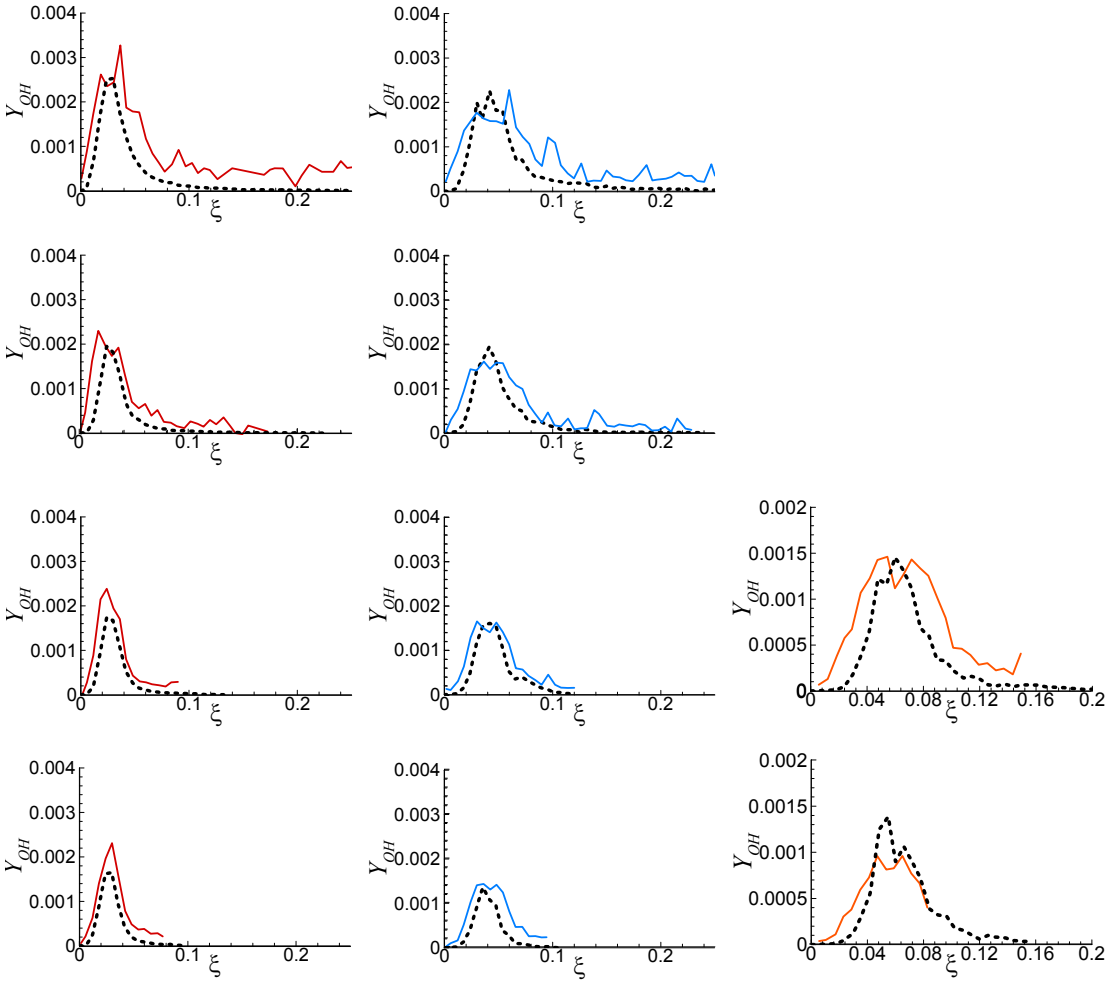

Figure 3.10 Conditional rms of OH mass fraction profile, ODT result against experimental data for flame A, B and C. (dashed line: ODT result; color solid line: experimental data)

Figs. 3.11 and 3.12 show the conditional rms of H_2 and O_2 radial profile as the function of mixture fraction. At the base of the flame calculated rms shows a much higher fluctuation than measured profile for both species. However, further downstream reactants rms profiles are in good agreement with measurements. In the entrainment of flame those fluctuations are possibly caused by lack of data and difficulty of prediction in near field, as indicated before about the complicated flow condition near the nozzle. It is shown to be dominant reason for all the inability of accurately capture of near-field statistics.

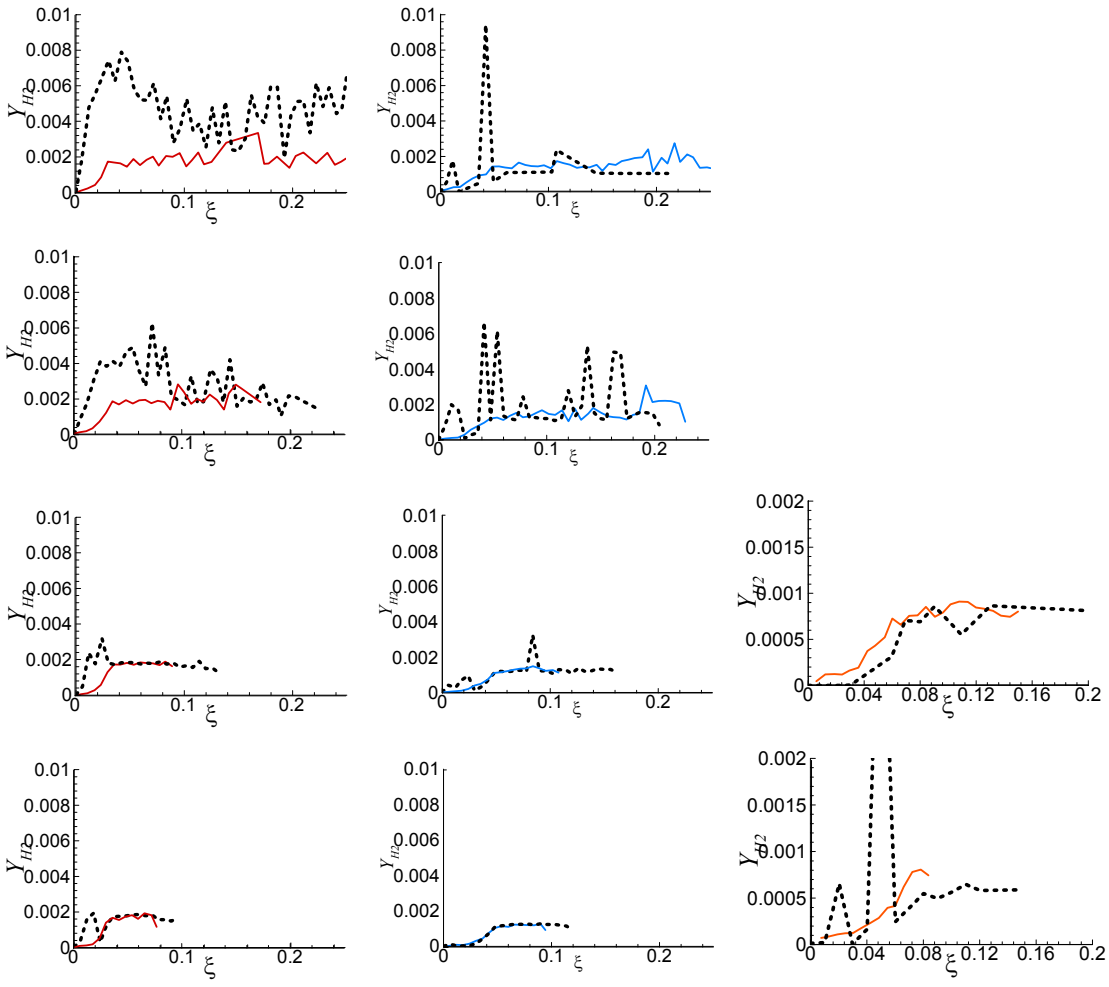

Figure 3.11 Conditional rms of H_2 mass fraction profile, ODT result against experimental data for flame A, B and C. (dashed line: ODT result; color solid line: experimental data)

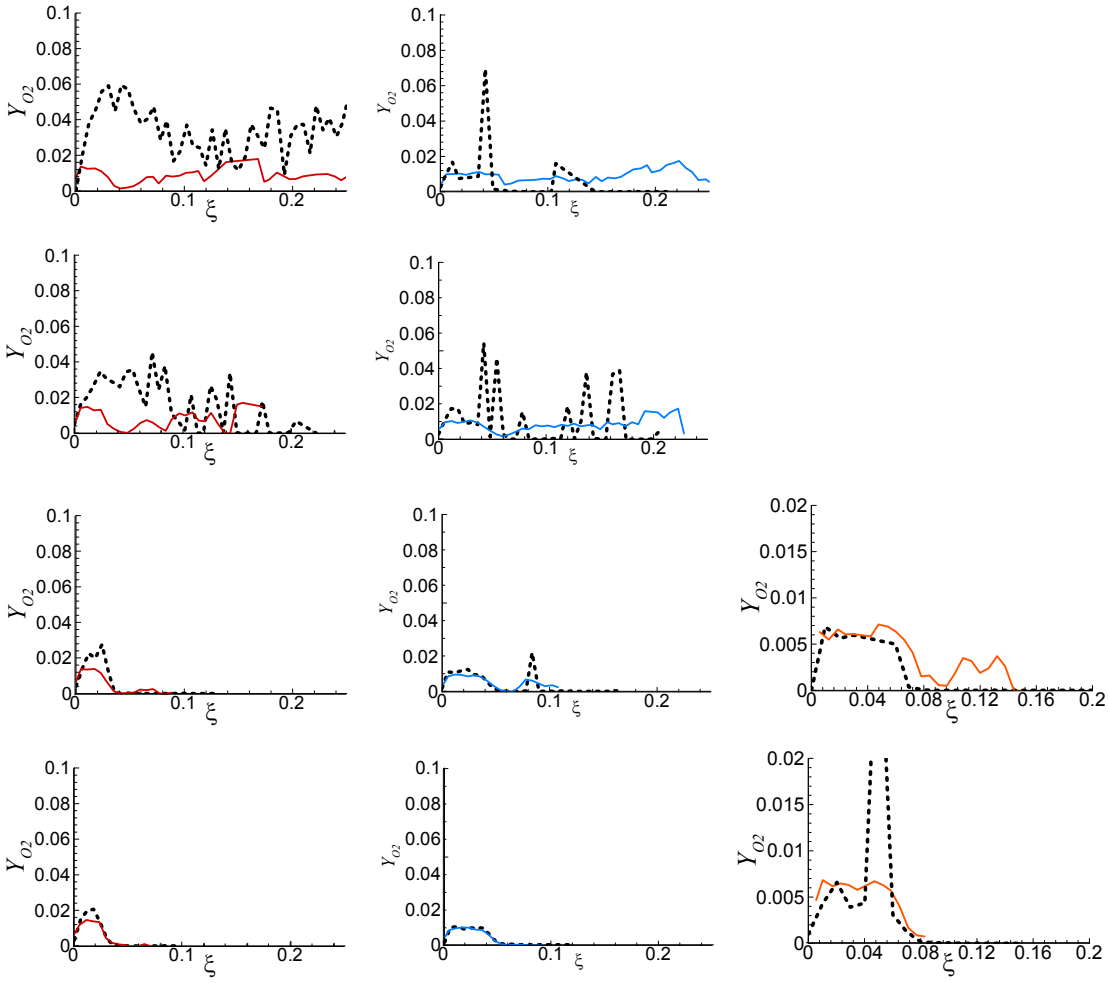

Figure 3.12 Conditional rms of O_2 mass fraction profile, ODT result against experimental data for flame A, B and C. (dashed line: ODT result; color solid line: experimental data)

We have represented the comparison of computational result and measurement of most important statistic conditional means and rms for the scalars. Several rules can be found from these axial profiles. The comparisons between the two data sets of computation and experiment show identifiable trends as a function of the downstream distance and the mixture fraction. Similar agreements are found among flame A, B and C. The rms result is captured greatly especially for intermediate species, such as NO and OH, although, it is not matched with experimental data as well as statistics mean result for some species.

3.3.3 Prediction of Flow Entrainment

It is more difficult to predict well for near field profiles of scalars than in far field in both conditional means and rms results, since near-field boundary conditions is more complicated to specify. Nonetheless, comparisons between computational and experimental results show identifiable trends as a function of the downstream distance. In the computational result, near field prediction is either higher or lower than measurement in many scalar profiles, particularly in the conditional rms of H_2 and O_2 mass fraction in Figs. 3.11 and 3.12. At the locations x/L=1/8 and 1/4, computed data showing a fluctuation along the entire mixture fraction range. But at downstream location of x/L=3/8 and 1/2, better agreement between simulation and measurement is obtained although no significant attempt at matching the further downstream location is done.

Chapter 4

Finite-Rate Chemistry Effect on Autoignition of Hydrogen with Preheated Air in Turbulent Jet Flames

The autoignition of non-homogeneous mixture of hydrogen-nitrogen jet in heated air is studied computationally using the ODT model. The emphasis is placed on the role of finite-rate chemistry effect on this transient problem with evolving interaction between chemistry and molecular and turbulent transport. At the same time the effect of pressure and turbulent intensity on non-homogeneous autoignition delay time and temperature and mixture fraction on ignition kernels locations and propagation are investigated as well.

The detailed chemical mechanism applied to this H_2-air turbulent non-homogeneous media is listed in Table 4.1, which is based on CHEMKIN library (Kee, Miller & Jefferson 1983; Kee, Warnatz & Miller, 1983, Kee, Grcar, Smooke & Miller 1985). While two-dimensional autoignition simulation, somewhat simpler geometries than three-dimensional turbulence, is used in computational work adequate capture of fluid dynamics, chemistry and molecular transport is expected since autoignition is a highly localized phenomenon. In study, we will also use the Bilger mixture fraction for conditional statistics as defined in Chapter 2.

Table 4.1 Hydrogen-Air Mechanism. Rate constants are in the form $k_f = A\ T^{\beta} \exp(-E_a/RT)$; units are moles, cm, sec, K, and kcal/mol. Third body coefficients in reactions 5, 6, 7, 8, 9 and 15 enhancement factors are 0.12 for H_2O and 0.25 for H_2.

	Reaction	A	β	E_a
1	$H+O_2 \Leftrightarrow O + OH$	1.92×10^{14}	0.0	16.44
2	$O+H_2 \Leftrightarrow H + OH$	5.08×10^{4}	2.67	6.29
3	$OH+H_2 \Leftrightarrow H + H_2O$	2.16×10^{8}	1.51	3.43
4	$OH + OH \Leftrightarrow O + H_2O$	1.23×10^{4}	2.62	-1.88
5	$H_2 + M \Leftrightarrow H + H + M$	4.57×10^{19}	-1.4	104.4
6	$O + O + M \Leftrightarrow O_2 + M$	6.17×10^{15}	-0.50	0.0
7	$O + H + M \Leftrightarrow OH + M$	4.72×10^{18}	-1.0	0.0
8	$H + OH + M \Leftrightarrow H_2O + M$	2.25×10^{22}	-2.0	0.0
9	$H + O_2 + M \Leftrightarrow HO_2 + M$	6.17×10^{19}	-1.42	0.0
10	$HO_2 + H \Leftrightarrow H_2 + O_2$	6.63×10^{13}	0.0	2.13
11	$HO_2 + H \Leftrightarrow OH + OH$	1.69×10^{14}	0.0	0.87
12	$HO_2 + O \Leftrightarrow OH + O_2$	1.81×10^{13}	0.0	-0.4
13	$HO_2 + OH \Leftrightarrow H_2O + O_2$	1.45×10^{16}	-1.0	0.0
14	$HO_2 + HO_2 \Leftrightarrow H_2O_2 + O_2$	3.02×10^{12}	0.0	1.39
15	$H_2O_2 + M \Leftrightarrow 2\ OH + M$	1.20×10^{17}	0.0	45.5
16	$H_2O_2 + H \Leftrightarrow H_2O + OH$	1.00×10^{13}	0.0	3.59
17	$H_2O_2 + H \Leftrightarrow H_2 + HO_2$	4.82×10^{13}	0.0	7.95
18	$H_2O_2 + O \Leftrightarrow OH + HO_2$	9.55×10^{6}	2.0	3.97
19	$H_2O_2 + OH \Leftrightarrow H_2O + HO_2$	7.00×10^{12}	0.0	1.43

4.1 Run conditions

The investigation of the autoignition process of hydrogen-air mixture in turbulent non-homogeneous mixture is implemented numerically using the ODT model. The initial

configuration consists of 2D segregated fuel jet with heated air in the co-flow. The oxidizer (the air) is hot enough to play the role of an energy source, so that the temperature of the mixture formed by diffusion of heat and reactants will be high enough to get self-ignition in the scalar mixing layer between fuel and oxidizer. The fuel is 30% hydrogen and 70% nitrogen by volume at 300 K. The oxidizer is heated air (volume ratio of oxygen to nitrogen: 21:79) at prescribed temperatures given in Table 4.2. In the present study, the stoichiometric value of the mixture fraction is 0.498. The other initial conditions are also shown in Table 4.2.

Table 4.2 Summary of run conditions for four different cases

	A	B	C	D
Pressure (atm)	1	1	3	3
Reynolds number	5000	10000	5000	10000
Air temperature (K)	980	980	1030	1030

As shown in Table 4.2, the mixture pressure, which is considered constant throughout the runs, and corresponding initial air temperature are different for four cases. Since the ignition temperature exhibits an S-shaped pressure dependence similar to that observed in explosion limits of homogeneous hydrogen-air mixtures (Kreutz &Law 1996), the initial air temperature is set high enough to result in autoignition within the second ignition limits. Two different sets of oxidizer temperatures and corresponding pressures result in comparable shortest ignition delay times for homogeneous mixtures. Different Reynolds numbers based on the internal diameter for identical pressures are used to investigate turbulent transport effects on the autoignition process. The coflow air velocity is 1.0 m/s for all the cases.

4.2 Homogeneous Autoignition

To demonstrate the importance of unsteady dissipation on autoignition, it is necessary to examine the homogeneous mixture autoignition process. The particular relevance to this study is the consideration of the dependence of ignition delay and chemistry on mixture composition and temperature. The homogeneous ignition is implemented using the SENKIN code (Lutz et al 1996) for two different fixed pressures and preheat temperatures for air. The autoignition delay is, then, studied for a range of mixture fractions extending from an all oxidizer mixture to an all fuel mixture. The initial mixture composition is determined from adiabatic mixing of the fuel and air mixtures at the prescribed mixture fraction which is implemented using EQUIL code (Lutz et al 1996). Figs. 4.2 and 4.3 show the homogeneous autoignition delay time as a function of the mixture fraction at 1 atm and 3 atm pressure, respectively. As shown in Figs. 4.2 and 4.3 the shortest ignition delay time for these two homogeneous cases are similar, which makes the non-homogeneous cases at the same conditions comparable with each other. Autoignition of hydrogen-air system at high pressure up to 7 MPa (Cain 1997) was studied, where ignition temperature is found to be independent of pressure. The two different run conditions of homogeneous turbulent autoignition are shown in Table 4.3.

Table 4.3 running condition of homogeneous autoignition

Figure	Pressure (atm)	Fuel temperature (K)	Air temperature (K)
4.2	1	300	980
4.3	3	300	1030

As shown in Fig. 4.2 for the atmospheric case, the shortest ignition delay time is less than 10^{-3} sec, and takes place at ξ=0.05. A broad range of mixture fraction from 0.03 to 0.1 is observed corresponding to short ignition delay time less than 0.001 sec for the 1 atm case. Fig. 4.2 shows that the first ignition appears at ξ=0.06, which means the onset of autoignition occurs at lean conditions. This is consistent with the previous result that the ignition kernels are identified as the region near the maximum temperature (Kreutz & Law 1996). Although the ignition delay time varies very little when mixture fraction is in the range of 0.02 to 0.13, the delay time changes by 4 orders of magnitude in the remaining range. Below ξ=0.02 autoignition is delay by the lack of chemical reaction activities and at ξ>0.12, the autoignition delay time is increased primarily because of reduced mixture temperature.

Fig. 4.3 shows the ignition delay time as the function of mixture fraction at the higher pressure (3 atm) of homogeneous ignition case, which is also governed by second ignition limit, corresponding to a higher cross over temperature. A preheat temperature on the oxidizer mixture of 1030 K is used for the case of 3 atm to get similar ignition delay time with the atmospheric case. It is important to note that, with a preheat temperature of 980 K, the ignition process for the mixture at 3 atm is not similar to the previous case in Fig. 4.3; the short delay time is observed in a relatively narrow range of mixture fraction. The shortest ignition delay time is less than 10^{-3} sec and occurs at ξ=0.03. Therefore, the possibility of ignition kernels appearance is smaller than atmospheric case. The adiabatic pure mixing temperature as a function of the mixture fraction is also included in both homogeneous ignition delay plots for reference.

4.3 Result and Discussion of Autoignition Process in Non-Homogeneous Mixture

The fuel jet and coflow oxidizer in the geometry is shown in Fig. 4.1 before the mixing process without reaction. There is 2 ms pure mixing process before initial time setting 0 ms so that the autoignition process is actually investigated in the partially premixed regime. Fig. 4.4 shows radial temperature profiles at different time of the autoignition process for Case A. The location, X=0, corresponds to the centerline of the jet. At 0.09 ms of autoignition the first kernels appear at two locations at the fuel-oxidizer interface where the mixture fraction is varied from fuel rich to lean. Next, at 0.2 ms these two kernels do not dissipate and continue to propagate, but no new kernels have been generated in addition to these two kernels. At 0.5 ms, new kernels have appeared and started to propagate to both fuel lean and fuel rich sides of the jet. At the latest time shown in Fig. 4.4, ignition kernels begin to merge with neighboring kernels and the new resulting kernels continue to propagate.

Fig. 4.5 shows the radial temperature profiles at the higher Reynolds number case. The figure shows more interfaces between fuel and oxidizer, which are generated prior to the onset of autoignition. At 0.06 ms two ignition kernels have already formed at the interface of fuel and oxidizer streams. More kernels are observed at later times. In total, there are six ignition kernels at 0.1 ms, and, nine kernels at 0.3 ms. The ignition kernels continue to grow and propagate as shown in Case A. There are two mechanisms that are responsible for the increase in the number of kernels in the system. First, turbulent events increase fuel-oxidizer interfaces through mixing, which evolve into kernels. Second, the existing kernels are split into many kernels by triplet map (turbulent advection). From 0.3 ms different

kernels begin to merge with each other. At 0.5 ms no more ignition kernels are generated and the temperature fluctuations between each neighboring kernel are becoming weaker, which means the kernels are merging together. At a later condition of 1 ms shown in Fig 4.5, relatively small (in size) kernels tend to dissipate, while larger kernels continue to propagate and eventually merge with neighboring kernels. The only difference between Cases A and B is that the latter case has a higher Reynolds number of 10,000 which is double that of Case A, which results in a stronger turbulence intensity. This can be easily seen in the initial temperature profile solely from pure mixing between jet fuel and coflow air. The autoignition processes for both Cases A and B are similar while B shows more fuel-oxidizer interfaces and ignition kernels according to turbulence effects. The effect of turbulence intensity on ignition delay time will be discussed later.

Fig. 4.6 shows the temperature profile as a function of radius at different time for autoignition process for Case C. The trends of kernel ignition and growth shown in Fig. 4.6 are similar to those in Fig. 4.4; but a much longer delay is observed, about 0.8 ms for Case C, which is larger in one order than Case A. The kernels grow relatively slowly in Case C, which is probably caused by the higher pressure. Higher pressure cases have narrow ignition kernels, leading to decreased chances for kernels propagation and growth. At the same time high pressure results in high viscosity, which dissipates more turbulence. That makes the temperature profile of Case C is more like a laminar flow than a turbulent one. The high pressure will result in high diffusion, which dissipates more radical pool in the mixture. This is possibly the reason for the longer ignition delay time and the slower kernels propagation in the higher pressure cases.

Fig. 4.7 shows radial temperature profiles at different stages of the autoignition process for Case D. The first ignition kernel is observed at 0.4 ms, at the approximately the same time as Case C. Due to the stronger turbulence intensity, Fig. 4.7 shows increased fuel-oxidizer interfaces compared to Case C. However, the propagation rate of ignition kernels in Case D is much slower than in Case B, which has the same Reynolds number with D. The temperature variation of Case D has a similar trend to C but not B, which means that the pressure plays a more important role in autoignition delay than turbulence intensity, at least in the present study.

From Figs. 4.4-4.7, we can summarize the approximate autoignition delay time, τ_{ig}, of four different cases with their dominant properties in Table 4.4.

Table 4.4 Summary of Ignition delay time for the 4 cases

	A	B	C	D
τ_{ig} (ms)	0.09	0.06	0.6	0.3
Pressure (atm)	1	1	3	3
Reynolds number	5000	10000	5000	10000

Table 4.4 shows that among the conditions at the same pressure, the ignition delay time remains unchanged. However, results of Table 4.4 show at atmospheric pressure self-ignition is easier to take place compared with at higher pressure, or ignition delay time is increased with the pressure. This result demonstrates that autoignition delay time is almost entirely governed by pressure, with delayed ignition at higher pressures and same Reynolds

in Cases B and D, respectively, very little changes of ignition delay time are found for A, B and C, D by pair. Compared with other thermal properties, turbulence has a relatively small effect on the ignition time, which also shown in Mastorakos et al (1997), but a fairly important effect on the eventual evolution of these kernels. Stronger turbulence intensity increases the mixing process by increase mixture interfaces and ignition kernels as we seen in Fig. 4.5. At the same time, ignition can be delayed because of increased scalar dissipation, and hence diffusive losses, at the ignition location (Im, Chen & Law 1998). Too many kernels will delay ignition by annihilating each other. Therefore, the dependence of the ignition on turbulence is shown to be non-monotonic. In the present study, ignition delay time is decreased with Reynolds number. Since two pairs of Reynolds number have the same values, respectively, the same trends of delay variation with turbulent intensity are expected. In stronger or weaker turbulence, different trends may be found (Im, Chen & Law 1998). So that turbulence effects on ignition delay is non-monotonic and complex, or the variation in ignition delay due to the corresponding variation in turbulence intensity appears to be quite small, or even independent of Reynolds number (Hilbert & Thévenin 2002) although stronger turbulence can cause more ignition kernels and extinction at the same time.

4.3.1 Finite-Rate Chemistry Effects on Autoignition

In the four different cases we considered, the scalars displayed similar trends in autoignition process; although the delay time scale is different due to the pressure. When emphasis is placed on scalars fluctuations in mixture fraction space, additional insight is achieved. So,

in the following discussion only the result of case A will be presented to investigate the principle of autoignition in this non-premixed hydrogen-air mixture. Similar results can be found in the other three cases.

One useful tool for autoignition analysis is the presentation of data in terms of scatter plot of scalars vs. the mixture fraction. It provides the straightforward measure of scalar distribution as a function of Bilger mixture fraction at different stages of autoignition. The statistics are based on around 400 data points over the entire volume for each of the 4 cases considered. Fig. 4.8 shows a scatter plot of temperature as a function of mixture fraction at different time for case A. Initially, the temperature profile displays the pure mixing profile of oxidizer (980 K) and fuel (300 K) where mixture temperature varies linearly with ξ. At a later time, 0.13 ms, when ignition kernels have already appeared, temperature increases above the pure mixing values for the range of ξ from 0 to 0.2, indicating that ignition kernels take place first at fuel lean conditions. At 0.2 ms, combustion is established for a broader range of the mixture fraction. At the same time the reactant at very lean condition has been fully burnt out, and the temperature profile displays a shape that is typical of turbulent flames as shown in Fig. 4.8. Beside the ignited lean parts, the mixture temperature remains at pure mixing values at other ranges of mixture fractions. The local peak value of temperature is higher and shifts towards the stoichiometric mixture fraction.

At 0.4 ms, more mixture has ignited and involved in the high-temperature combustion process. The mixture at very fuel lean side is mostly burnt out. There are two separate curves in this plot. One corresponds to the pure mixing temperature profile. The other

corresponds to a turbulent flame temperature profile, showing similar trends to conditional means of temperature in Chapter 3. At 0.8 ms, more data points are shown in the flame temperature profile, while less of the data points remain at pure mixing conditions and towards the fuel-rich side of the mixture. The location of local peak temperature has shifted to near ξ=0.5, almost at the mixture fraction of stoichiometric conditions of 0.498. At much later time, e.g. 2 ms, most mixture is ignited and burnt out and the resulting scatter plots are similar to a turbulent flame scatter plot. However, there still exists little unignited mixture on the fuel-rich side where temperature remains at the pure mixing value. This result illustrates that fuel rich side of lower initial temperature needs a relatively longer time to ignite. At 2 ms, the mixture is already at high-temperature combustion process rather than low-temperature autoignition process. The reacting mixture displays a range of mixture fractions that are favorable to the onset of ignition; the preferred range of mixture fraction evolves in time as combustion switches from the ignition kernels to propagating fronts. This range corresponds to temperature profile changes as peak temperature increases and shifts closer to stoichiometric conditions.

Fig. 4.9 shows a scatter plot of the product, H_2O as a function of the mixture fraction at different ignition stages for case A. Initially, no H_2O is present for the entire range of the mixture fraction, because ignition has not started yet. At 0.13 ms, some H_2O is generated at fuel lean conditions, corresponding to the same range of mixture fraction represented by higher temperatures in Fig. 4.9 at the same time. As the only product in hydrogen-air chemical reaction, H_2O displays the same trend with temperature, which is characterized by an increase in peak value and a shift towards stoichiometric mixture conditions. At 0.2 ms,

as shown in Fig. 4.10, the peak value of H_2O mass fraction has increased to 0.09 at ξ=0.3, where peak value of temperature happened at the same time. At this time there is seldom H_2O existing beyond the region $0<\xi<0.3$, where reacting mixture is not ignited and propagation of existing ignition kernels is still limited. At 0.4 ms H_2O mass fraction is observed in a broader range of the mixture fraction with larger peak values, which continues to shift towards stoichiometric conditions. At 0.8 ms the turbulent flame product profile is almost established except at fuel rich condition, where ignition has not yet occurred. One interesting phenomenon is that all the mixture at fuel lean conditions has burnt out; but, more extinction and unburnt mixture can be found at fuel rich conditions. The unburnt mixture can be found as late as 2 ms as shown in Fig. 4.9, where some scatter points show relatively low to zero value at fuel rich side.

Fig. 4.10 shows scatter plots of H_2 mass fraction as a function of Bilger mixture fraction at different time for case A. At 0 ms, the figure shows pure mixing profiles for H_2. After the fuel ignited and burnt out at very lean conditions, more fuel mass fraction decrease to zero from lean side extending to stoichiometric conditions. The flames evolve from predominantly fuel lean conditions towards fuel rich conditions as a function of time according to more fuel involved in the chemical reaction and burnt over with time. At 0.4 ms, the shape of H_2 scatter plot has changed into turbulent flame profile on the fuel-lean side. There are some scatter points beyond zero and the pure mixing curves caused by differential diffusion effects. At a later time, more H_2 is shown to be ignited and burnt out while the curve of H_2 mass fraction of turbulent flame is established at 0. There still exists some extinguished and unburnt H_2 at fuel rich condition at 2 ms.

Fig. 4.11 shows scatter plot of O_2 mass fraction at different time. Initially a pure mixing O_2 mass fraction profile is shown at 0 ms before any chemical reaction occurs. Then O_2 mass fraction begins to decrease from the fuel-lean side towards the fuel-rich side with time. At 0.2 ms, the range of ignited O_2 has expanded from very lean condition towards stoichiometric conditions. Because of differential diffusion, the pure mixing curve of O_2 mass fraction is broader than at the initial time. At 0.4 ms, the ignited oxygen is found in fuel rich, or oxidizer lean conditions, while some O_2 mass fraction at fuel lean conditions is shown as un-ignited and remains at pure mixing values. All O_2 in the range of mixture fraction 0 to 0.25 has ignited at 0.4 ms while the edge of this range shifts to 0.35 at 0.8 ms, and 0.5 at 2 ms. Therefore ignition always occurs at fuel lean condition first. As flame propagation, the oxidizer in fuel rich side also ignites but always later than on fuel lean side. At the latest time shown in Fig. 4.11, all the oxygen is ignited in fuel lean side. At the same time even though oxidizer is deficient there still left unignited O_2 in fuel rich side, indicates that temperature plays a significant role of influence on autoignition location and delay time, which always happen first at highest temperature. Mixture fraction plays a relatively minor effect on locations or delay time in this case.

Finally, intermediate species of OH mass fraction scatter plot is shown as as function of mixture fraction at different time in ignition process in Fig. 4.12. Initially, OH concentration is zero or insignificant in the mixture. After ignition kernels appear some intermediate species are generated with temperature increasing at very lean conditions. More OH mass fraction is obtained in a wider range of mixture fraction when the peak value of temperature keeps increasing. OH mass fraction has reached its maximum value

near stoichiometric condition but a little shift towards fuel lean side. When OH established its profile in the whole range at 0.4 ms most of them are between 0.004 and 0.008 at the range of mixture fraction from 0.25 to 0.5. For this range of OH mass fraction at later time, the magnitude of OH mass fraction stages continue to decrease while the mixture is evolving to burn out. Intermediate species mass fraction expresses more about current reaction chemical activity than present combustion products. Here OH mass fraction is a characteristic of chemical activity of the system. So that OH mass fraction is expected to be zero at the beginning and towards the end of reactions. We can expect that at very late time, OH mass fraction will decrease to zero in the entire range of mixture fraction when the combustion process is completed.

We have discussed scatter plots of all the thermochemical scalars including temperature, reactant (H_2, O_2), product (H_2O) and intermediate species (OH) varying at different stages in this hydrogen-air autoignition process. All of them are affected by finite-rate chemistry and have followed the principle of autoignition. Finally all scalars profiles show the typical turbulent flame profiles which are consistent with our previous result. Thus, the mixture has evolved from low-temperature self-ignition process to high-temperature combustion process. All the plots represented here are generated from case A. Nonetheless similar plots for other three cases can be obtained as well.

Fig. 4.13 shows the conditional means of temperature as a function of the Bilger mixture fraction for Case A. The temperature profiles at different stages of the autoignition and high-temperature combustion process, 0, 0.09, 0.1, 0.13, 0.2, 0.3, 0.8 and 1 ms, are

represented in one plot. At 0 ms the curve shows the temperature profile at pure mixing condition. At 0.09 ms the self-ignition begins from fuel lean conditions, where higher mixing temperatures are found. Then, the peak value of temperature is increased with time while shifting towards the value of the mixture fraction near stoichiometric conditions, since the ignition-assisted combustion near stoichiometric conditions finds optimum proportions of fuel and oxidizer to burn. Therefore, the temperature profile contained the maximum value in entire range of ξ in the combustion process would and should display it at stoichiometric condition. After that there is no shift for local peak to rich or lean side any more since the system is in equilibrium conditions. This can be also verified in conditional PDF and progress variables profiles as discussed later.

4.3.2 Autoignition process in different mixture fraction

Conditional PDFs of scalars is presented to understand the scalar quantity changes as a function of the mixture fraction during ignition and subsequent combustion processes. Conditional PDF of temperature, H_2O, H_2, O_2 and OH mass fraction are presented for five different ranges of mixture fraction from lean to rich conditions, respectively, as shown in Table 4.5.

Table 4.4 Different mixture fraction ranges running in conditional PDF

$0<\xi<0.2$	$0.2<\xi<0.4$	$0.4<\xi<0.6$	$0.6<\xi<0.8$	$0.8<\xi<1$
very fuel lean	fuel lean	stoichiometric	fuel rich	very fuel rich

4.3.2.1 Conditional PDF of the Progress Variable

The progress variable, c, is defined as:

$$c \equiv \frac{T - T_u(\xi)}{T_{ad} - T_u(\xi)}$$

Where T_u is the temperature of adiabatically mixed fuel and oxidizer at the mixture fraction, ξ; $T_{ad}(\xi)$ is the adiabatic flame temperature of the mixture staring from initial state at $T_u(\xi)$. Both T_u and T_{ad} are computed prior to the simulation and tabulated for look up as a function of the locally evaluated mixture fraction**,** ξ. Progress variable measures the extent of burning. From the definition, the value of progress variable is zero for unburnt mixture and 1 for a fully burnt mixture.

The mixture temperature is between unburnt temperature and adiabatic flame temperature when the mixture is partially burnt. At that time progress variable varies from 0 to 1 as the function of burnt mixture increases. Progress variable is a measure of the progress of burning process as a function of the mixture temperature.

Figs. 4.14 to 4.18 show the conditional PDF (probability density function) of progress variable at different stages of autoignition and subsequent high-temperature combustion process from fuel deficient to sufficient conditions for Case A. The PDF staying at zero of progress variable means at initial condition all reactants do not have any chemical reaction. In the end of combustion process ideally all progress variable should stay at 1 which

reflects reactants have fully burnt out and changed into product. Therefore, progress variable can be treated as a characteristic of chemical reaction procedure.

Fig. 4.14 shows the PDF of the progress variable within the range of very lean mixture fraction between 0 and 0.2. At 0.09 ms, the progress variable began to have value other than zero, which means mixture began to burn, or ignite at round that time. The PDF profile shifts from 0 to 1. At 0.13 ms PDF has value at all the bins shown in the figure. Subsequently, the PDF is increased in the bins near 1 while decreased in the bins near zero. The figure shows that most chemical reactions are completed before 1 ms; but there is still unburnt mixture left as shown with progress variable values at zero. Since at very lean condition, the fuel is very deficient there should be extra unburnt oxidizer left at this condition.

Figs. 4.15-4.18 show other PDFs of the progress variable profiles at fuel lean to very fuel rich, including the stoichiometric conditions, respectively. The PDF of progress variable initially changes at very lean conditions (0.09 ms), which is consistent with ignition delay time for the entire mixture. Then, this period of time is increased with the range of mixture fraction which corresponds to initial mixture temperature decreasing, where the fuel lean condition is characterized by a shorter delay time than fuel rich condition. This length of time is consistent with the autoignition delay time in the mixture, since progress variable is in the proportion to the mixture temperature. The transient process is fairly rapid and therefore, is harder to capture at discrete times. The post-processing is similar for different ranges of mixture fraction, or all mixture ranges eventually to evolve fully burnt products

(no extinction); although this process require longer time to complete at richer mixtures. In both very fuel lean and very fuel rich conditions, some unburnt reactants are left in the mixture because of deficient fuel and oxidizer, respectively, even at very late time. Next, emphasis is placed on the PDF of each thermal scalar including temperature, reactant and product mass fraction, at different mixture fraction ranges and time.

4.3.2.2 Conditional PDF of Temperature and Species

Figs. 4.19-4.23 show the very lean conditional PDF profiles of temperature, H_2O, H_2, O_2 and OH, respectively, in which the PDF of scalars at different ignition time are provided. Initially most mixtures are heated oxidizer at 980 K; no products and intermediate species in the mixture. Then, ignition kernels appear with a little amount of H_2O found and a higher temperature values at 0.09 ms. Note that at Fig. 4.4, ignition kernels are found at 0.09 ms first, consistently with the onset of ignition at this very fuel lean condition ($0<\xi<0.2$). The temperature increases rapidly after ignition is initiated and the ignition process is almost completed within 0.2 ms. At this condition, fuel mass fraction is very low compared with oxidizer mass fraction. At 0.2 ms, H_2 mass fraction is significantly reduced in the reacting mixture, indicating that most chemical reaction and product generation is completed at that time; while O_2 mass fraction is relatively stable with a little decrease in time because of the deficiency of fuel. OH mass fraction continues to increase until 0.2 ms; then, it drops very quickly during 0.2 to 0.3 ms and no OH is present towards the end of reaction. At very fuel-lean conditions no much fuel exists to provide enough reactant in combustion, which results

in the combustion process completed relatively early. So that in Figs. 4.19-4.23, the PDF shapes of the thermochemical scalars at 2 ms are similar with those at 0.2 ms.

At fuel-lean condition ($0.2<\xi<0.4$), as shown in Figs 4.24-4.28, there is more cold fuel and less heated oxidizer in the mixture first, which leads to an initial temperature at approximately 700 K. The PDF of the temperature profile has a higher value of up to 1000 K at approximately 0.17 ms. Consistently with the change in temperature PDF values, the PDF of H_2O mass fraction yields non-zero values at around 0.17 ms. From 0.2 ms another local peak of temperature PDF is observed between 1500 K and 2000 K, which corresponds to the premixed flame temperature at similar conditions of the mixture fraction. These two local peaks of temperature lead to two corresponding peaks in H_2O PDF profile at the same time. Prior to 2 ms all the PDF of temperature is found at the range of flame temperature (around second peak) with highest value of 2000 K. At the same time, the PDF values for H_2O are non-zero at the range $0.06<\xi<0.13$ (around the second peak). There is little OH generated at 0.17 ms and continues to increase until 0.4 ms. Then it shifts to lower value to zero with time. Fig 4.28 shows that OH has zero value during the initial and final stages of reaction in the mixture. It displays largest values at 0.4 ms, which means the system has high chemical activity at that time. At fuel lean conditions, most of the reacting mixture has ignited.

Figs. 4.29 and 4.30 show the PDF of temperature and H_2O at near stoichiometric conditions ($0.4<\xi<0.6$), where highest flame temperatures and maximum products are expected. Due to the lower initial mixture temperature of the stoichiometric condition, the autoignition

delay time is about 0.3 ms, which is longer than the previous two leaner mixture fraction ranges discussed earlier. Fig. 4.33 shows that the PDF of OH is almost zero at 0.3 ms, indicating that there is little chemical activity; although, H_2O is present at that time. At a later time, two local peaks of temperature PDF profile are present; and corresponding peaks of the H_2O PDF profile are obtained. The first peak corresponds to ignition kernels; while the second corresponds to already established flames. The ignition kernels tend afterwards to propagate along the interface of fuel and oxidizer, resulting in the second temperature peak in turbulent combustion. The first peak decreases while the second peak increases with time in both temperature and H_2O PDF profiles. Finally a large portion of the mixture has values for H_2O mass fraction in the range of 0.1 to 0.15 and most PDF of the temperature is concentrated between 1500 K and 2200 K. It is impossible to find the temperature PDF profile displayed in such a high range in any conditions other than stoichiometric conditions. The PDFs of H_2 and O_2 distribution during the autoignition and subsequent high-temperature stages are shown in Figs. 4.31 and 4.32, respectively. The figures show that the PDFs of H_2 and O_2 begin to decrease at around 0.3 ms with time. At stoichiometric conditions all the fuel and oxidizer are supposed to be burnt out in the combustion process. At 2 ms, there is very little reactant left in the mixture.

From the above discussion, it may be concluded that the autoignition delay time is most influenced by the initial temperature of the mixture. The initial increase in the temperature in the mixture occurs at very lean conditions ($0<\xi<0.2$). This result is consistent with the conclusion in Echekki & Chen (2003), where autoignition is initiated at discrete kernels by radical build-up in high-temperature, lean mixtures, and at relatively low dissipation rates.

However, the magnitude of the temperature and product generation in the autoignition process strongly depends on the mixture fraction. The results show that the maximum temperature and product concentration are obtained near stoichiometric conditions. The lowest temperature and product concentration were observed where fuel or oxidizer is very deficient. In the fuel-rich and very fuel-rich conditions, the initial mixture temperature is even lower than previous cases. Moreover the proportion of fuel to oxidizer is larger than the stoichiometric value; a slow autoignition process is expected. At fuel rich conditions, the PDF of H_2 mass fraction does not change significantly compared with other scalars, particularly when very little oxidizer exists in the mixture. All the PDF results of thermochemical scalars: temperature, H_2O, H_2, O_2 and OH, at fuel-rich and very fuel rich conditions are shown in Figs. 4.34-4.43, where similar conclusions can be made.

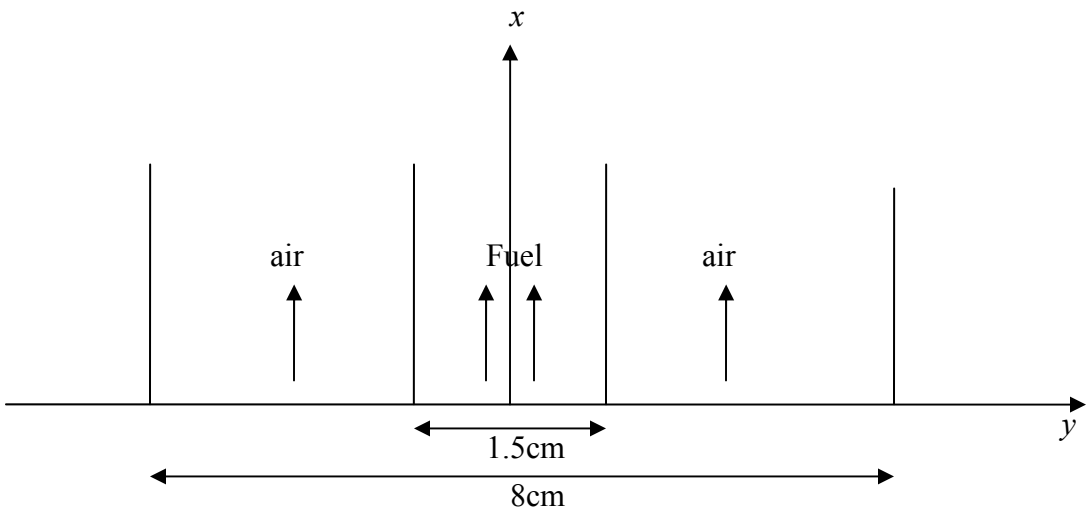

Figure 4.1 2D domain of initial running condition

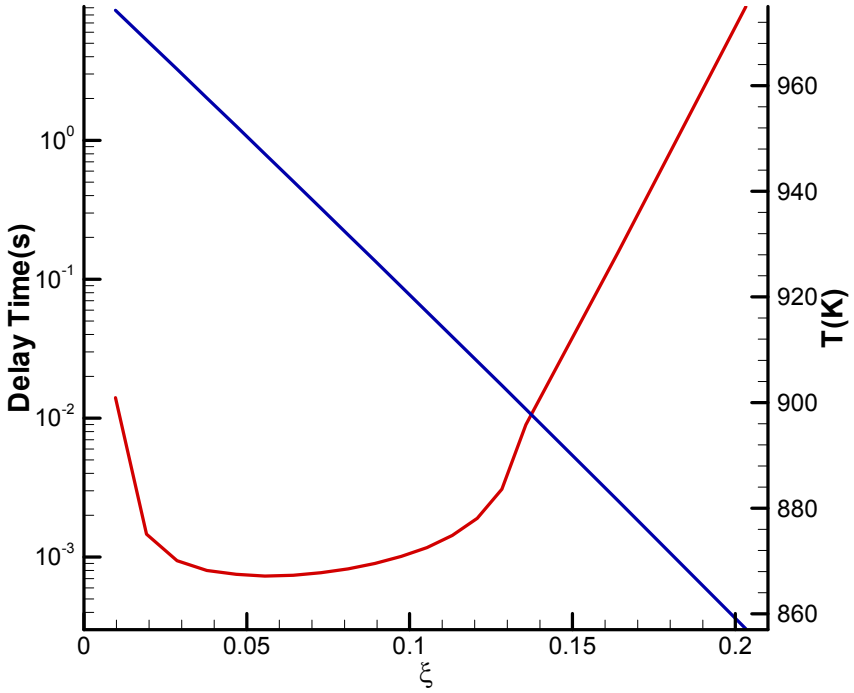

Figure 4.2 Autoignition delay time, mixture temperature vs. mixture fraction at P=1atm

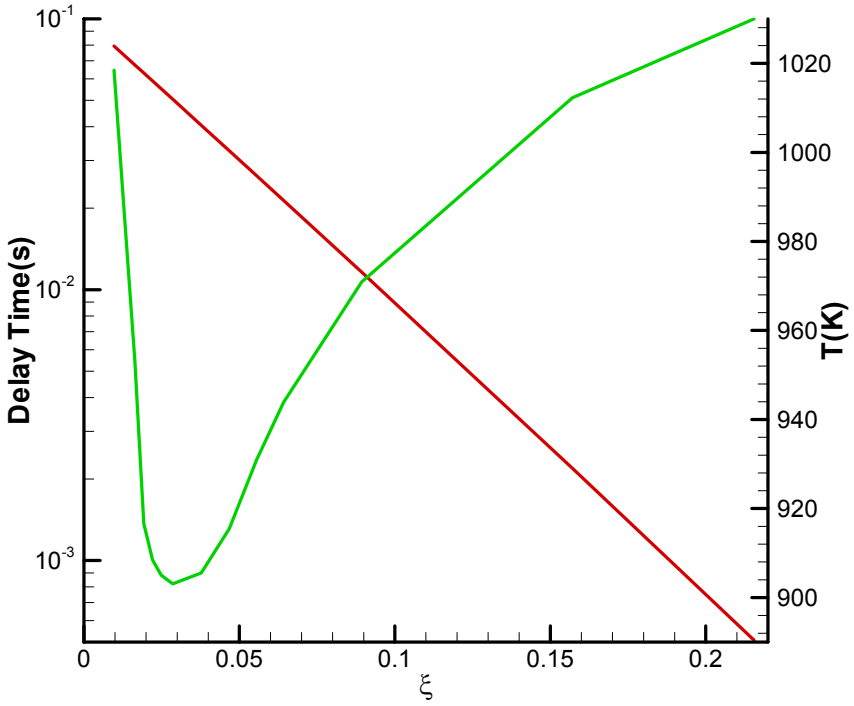

Figure 4.3 Autoignition delay time, mixture temperature vs. mixture fraction at P=3atm

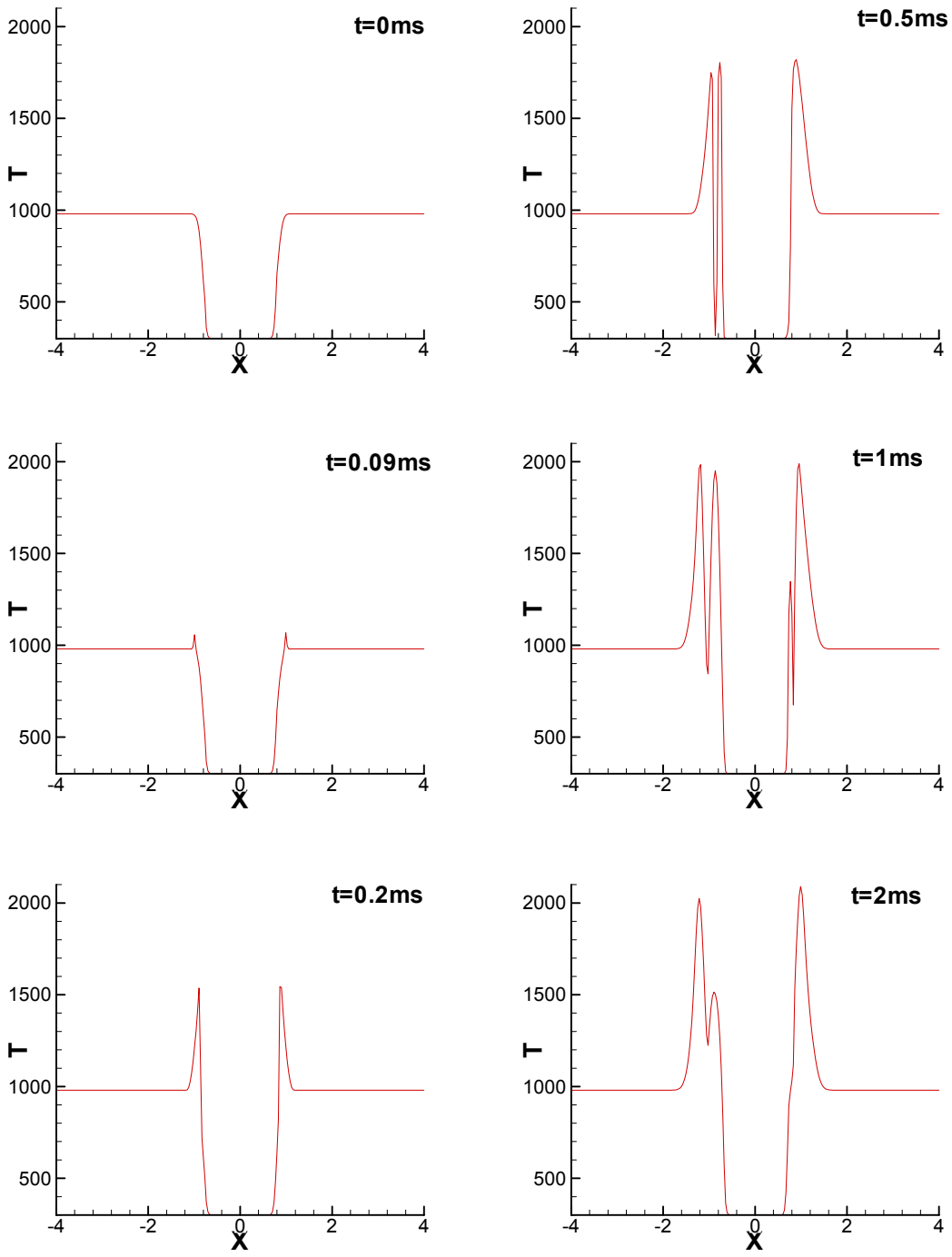

Figure 4.4 Autoignition delay time for case A (P=1atm, Re=5000)

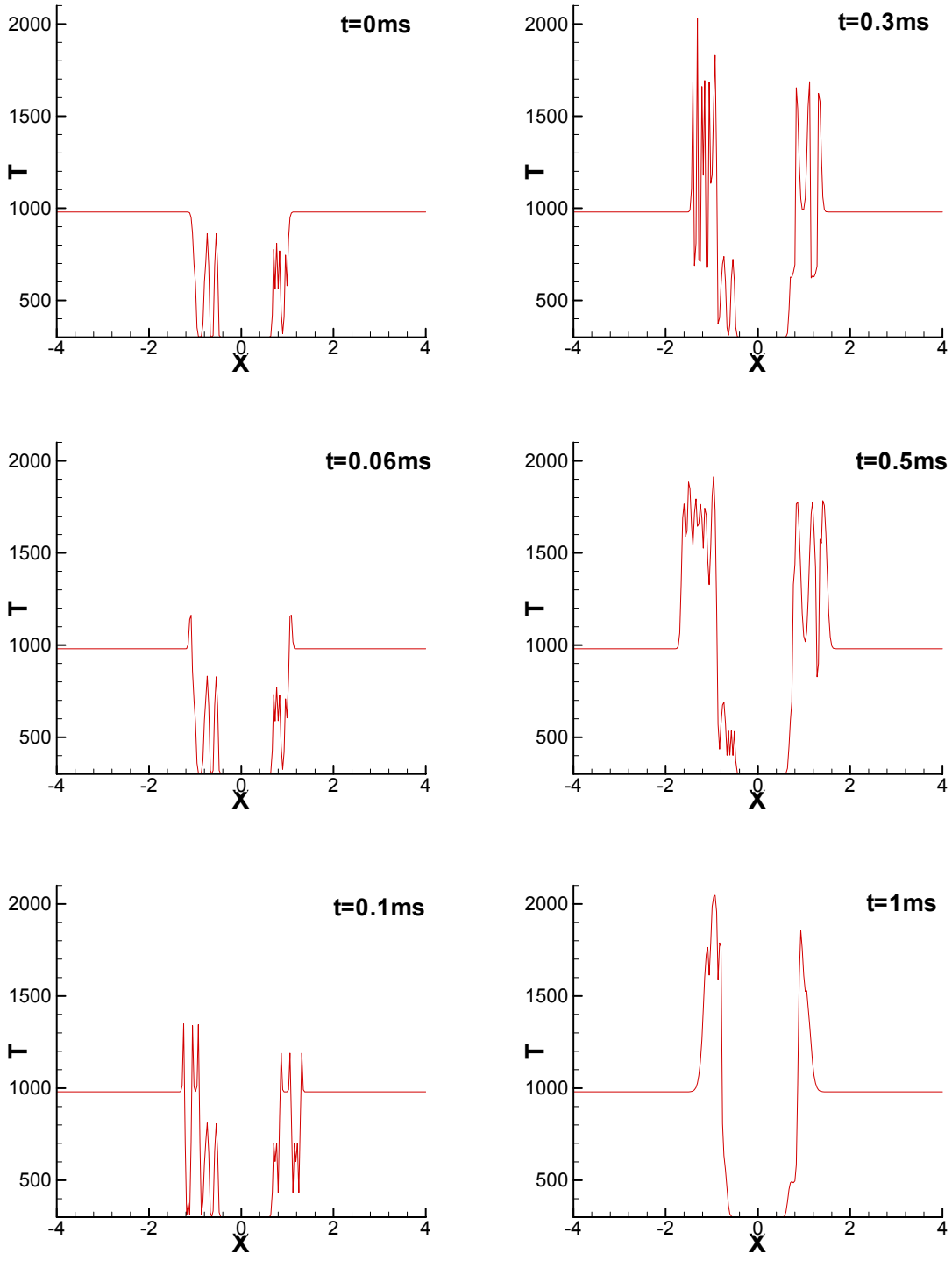

Figure 4.5 Autoignition delay time for case B (P=1atm, Re=10000)

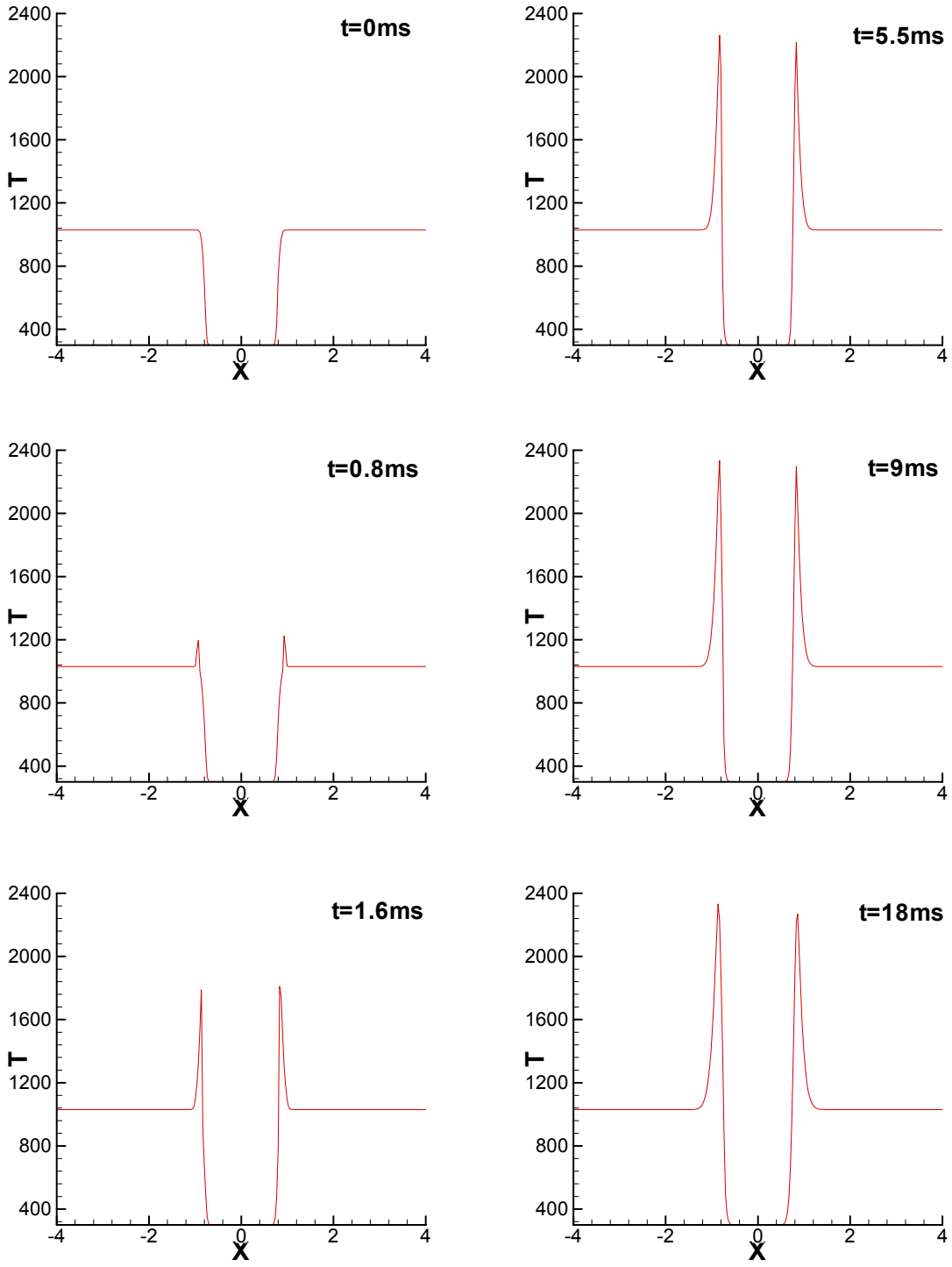

Figure 4.6 Autoignition delay time for case C (P=3atm, Re=5000)

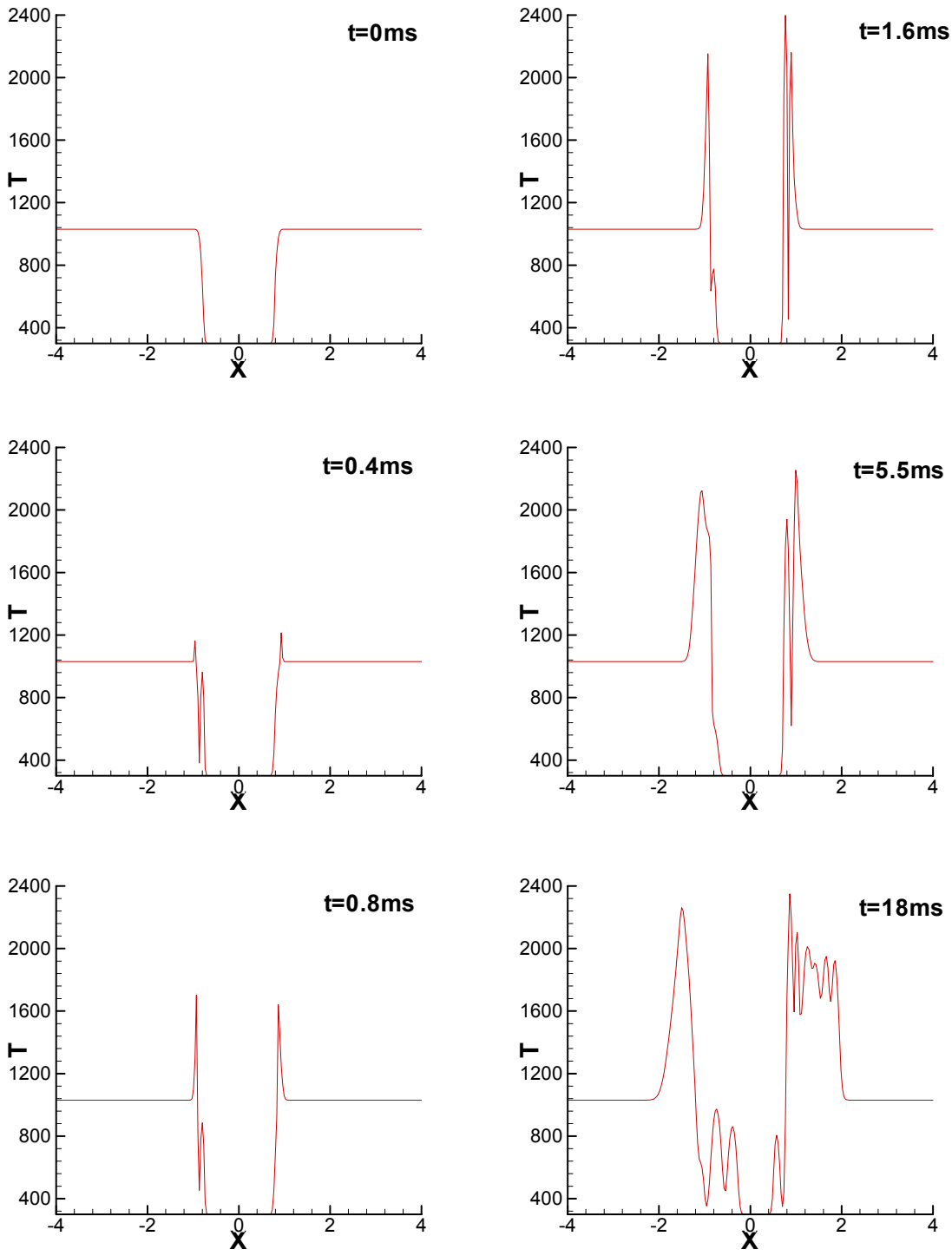

Figure 4.7 Autoignition delay time for case D (P=3atm, Re=10000)

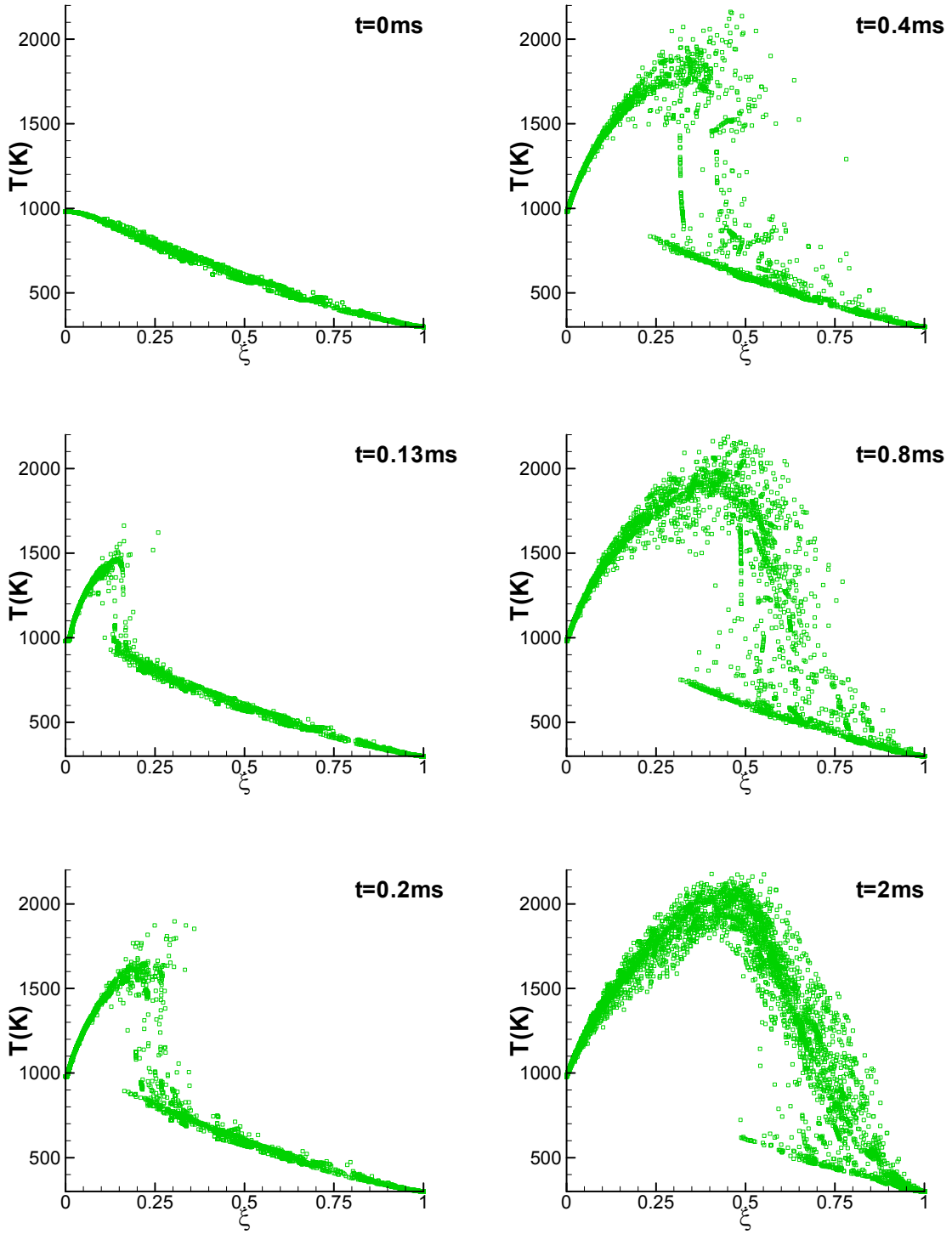

Figure 4.8 Scatter plots of temperature vs. mixture fraction for case A

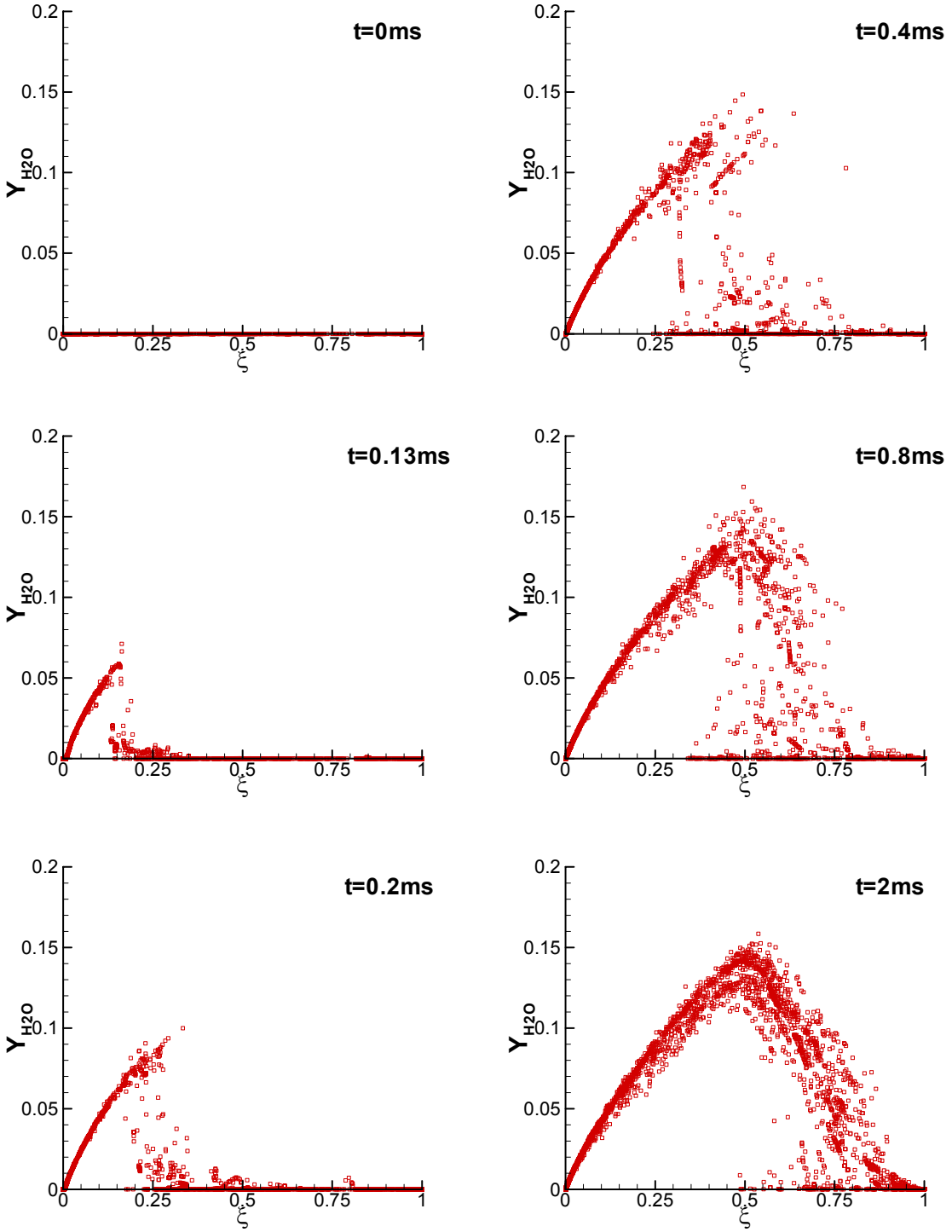

Figure 4.9 Scatter plots of H_2O mass fraction vs. mixture fraction for case A

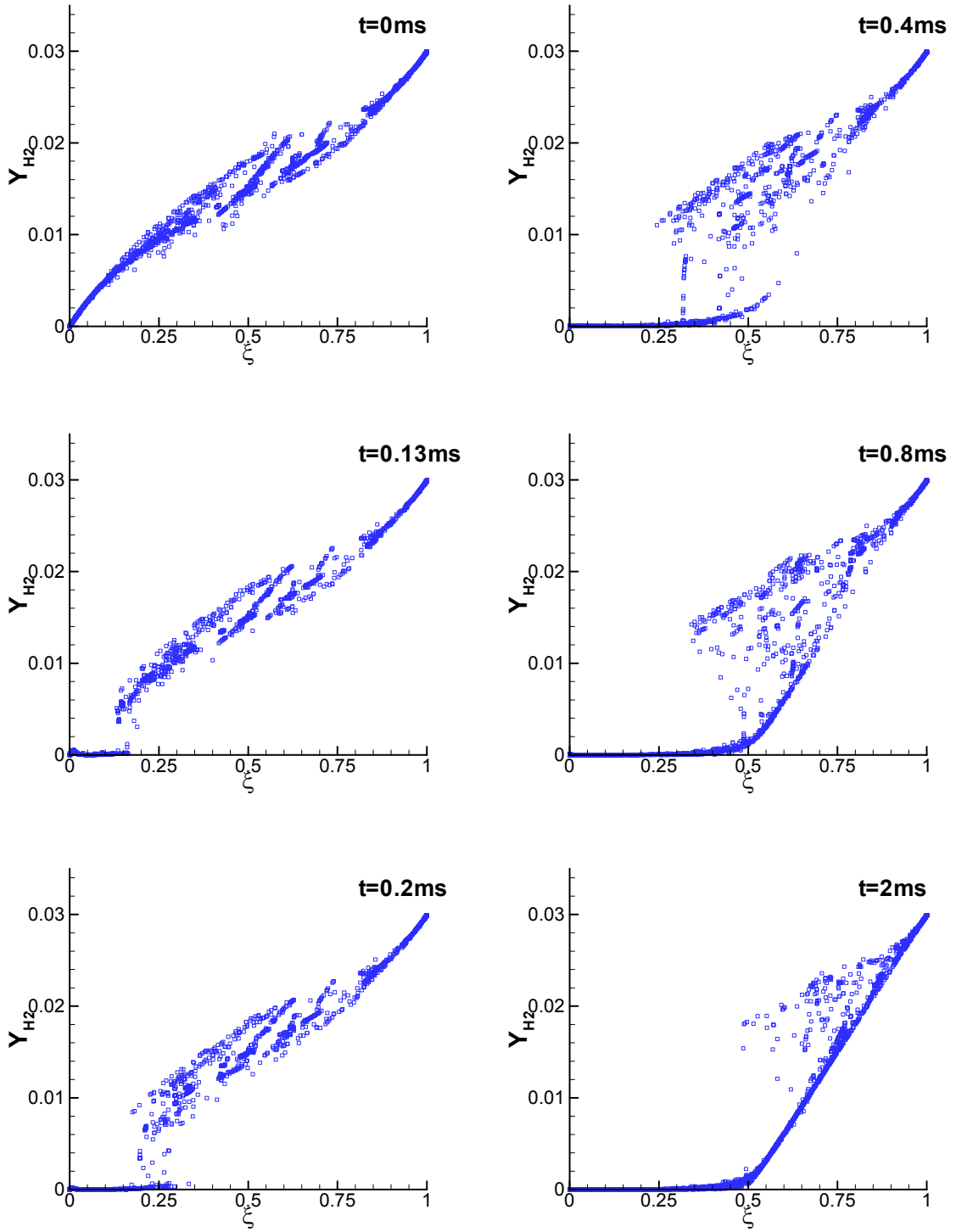

Figure 4.10 scatter plots of H2 mass fraction vs. mixture fraction for case A

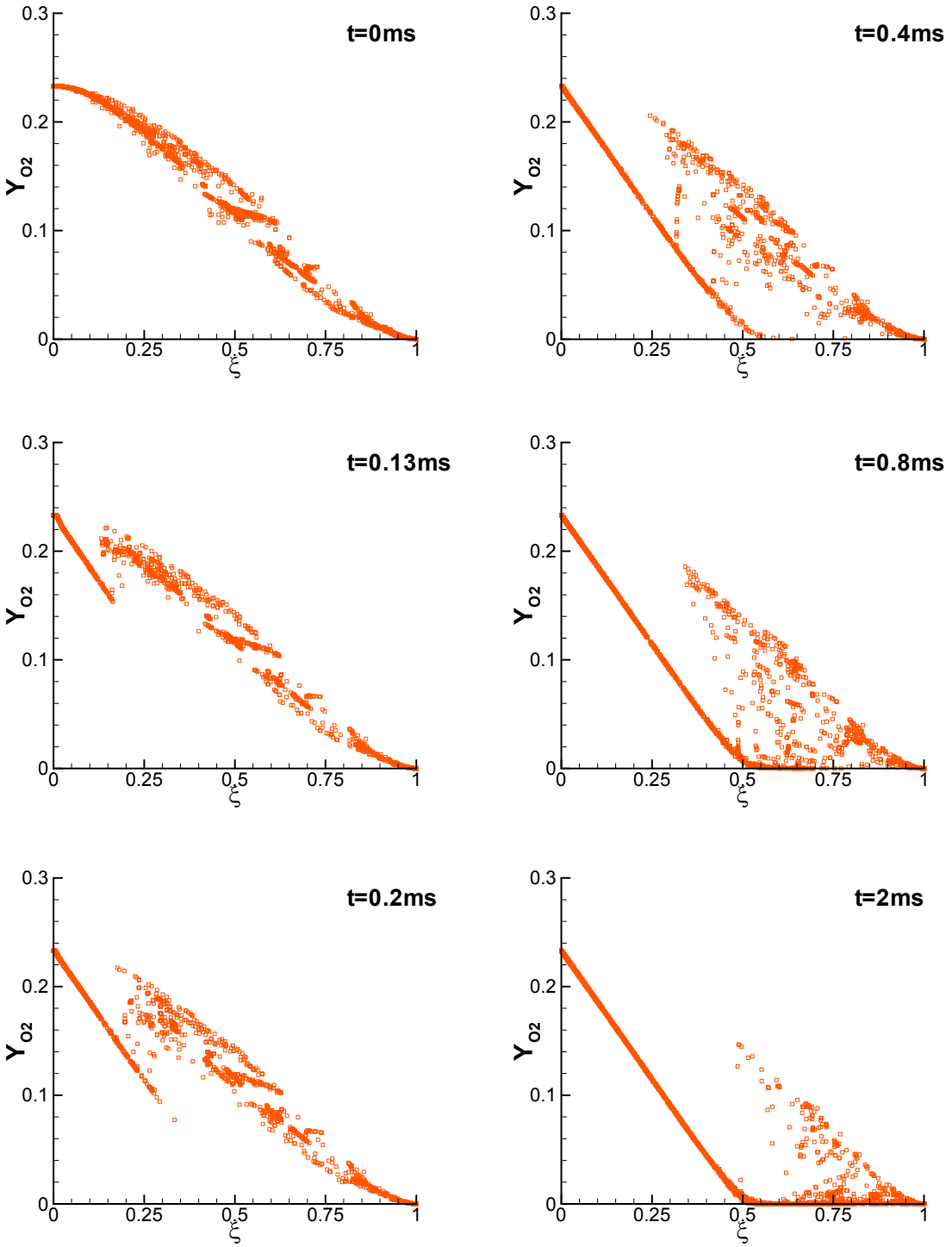

Figure 4.11 scatter plots of O2 mass fraction vs. mixture fraction for case A

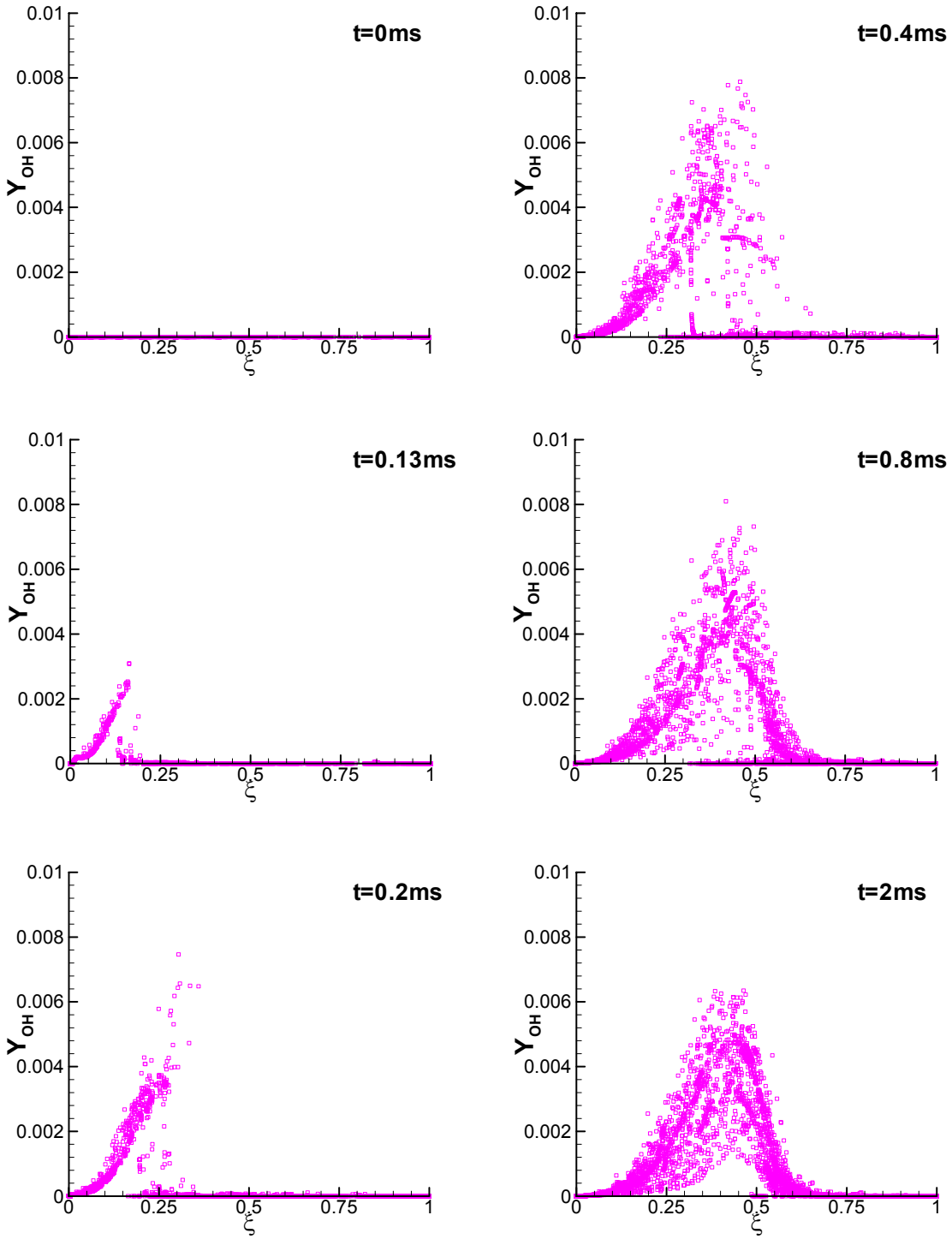

Figure 4.12 scatter plots of OH mass fraction vs. mixture fraction for case A

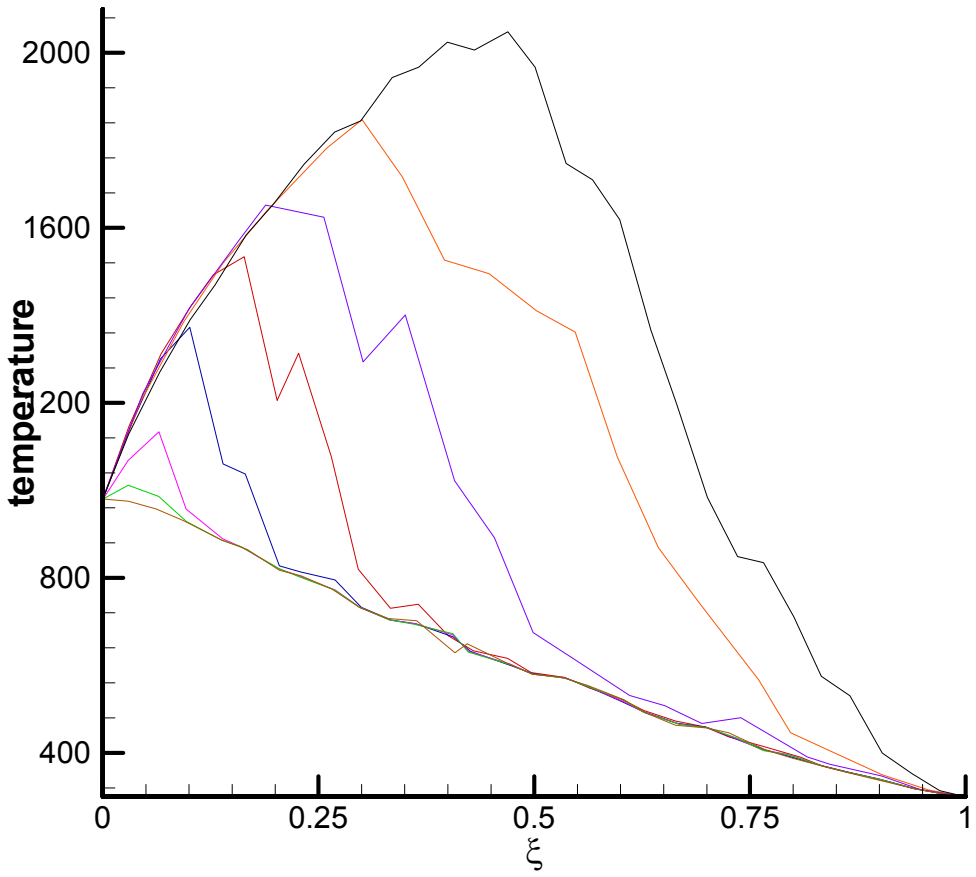

Figure 4.13 Temperature conditional means for case A (p=1atm, Re=5000)
Time=0, 0.09, 0.1, 0.13, 0.2, 0.4, 1, 3 ms

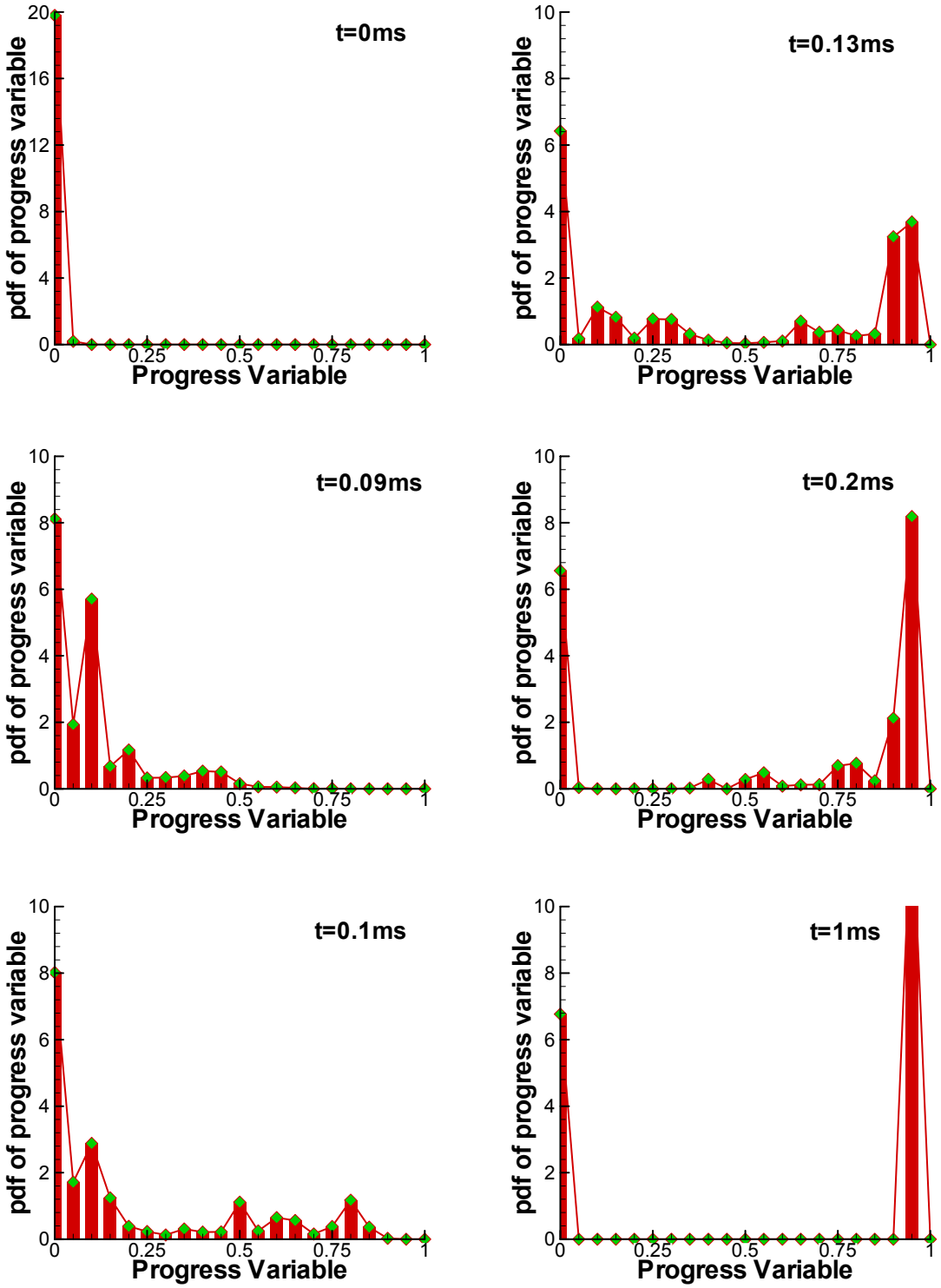

Figure 4.14 pdf of progress variables in the range of mixture fraction $0<\xi<0.2$

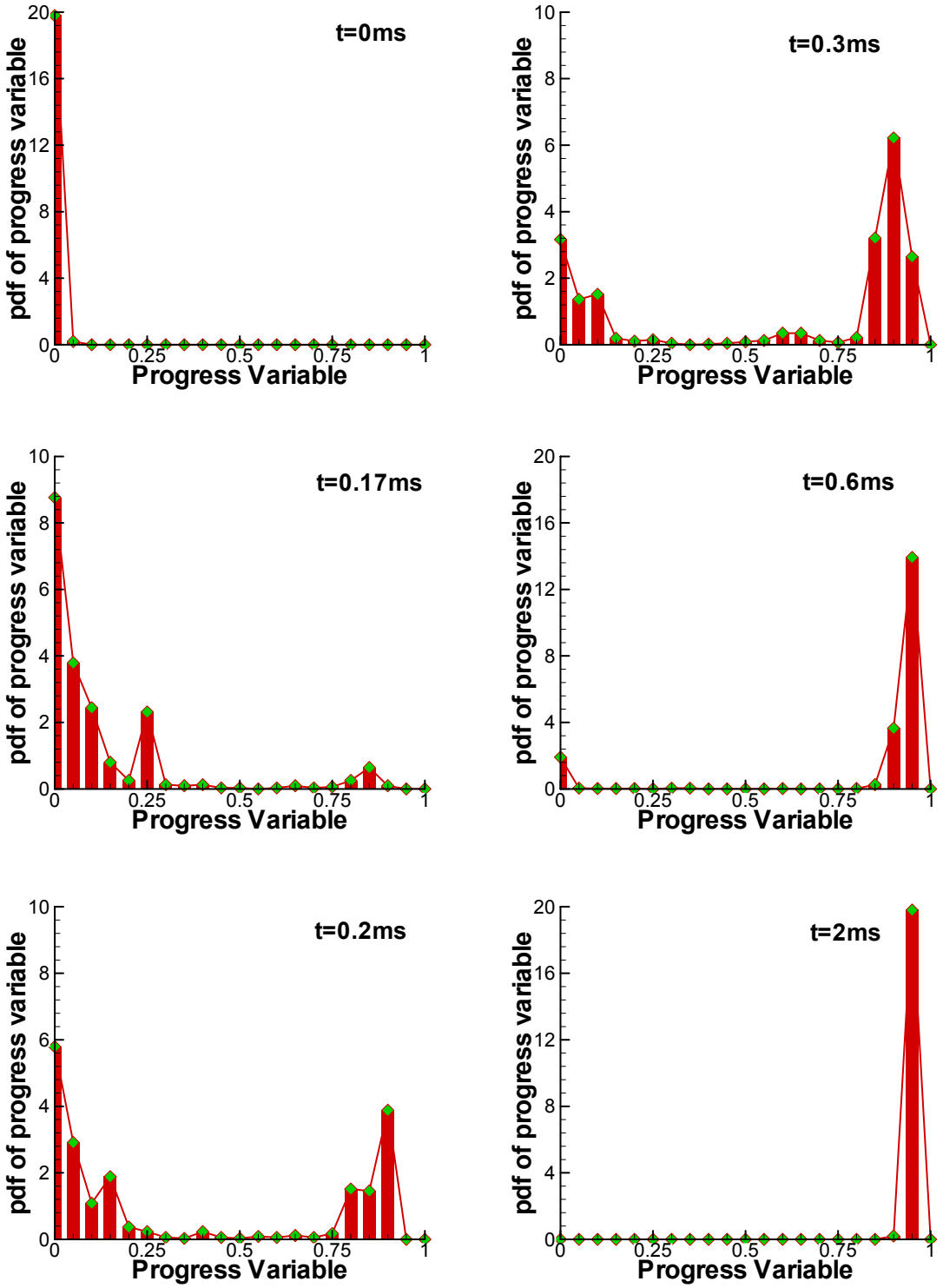

Figure 4.15 pdf of progress variables in the range of mixture fraction $0.2<\xi<0.4$

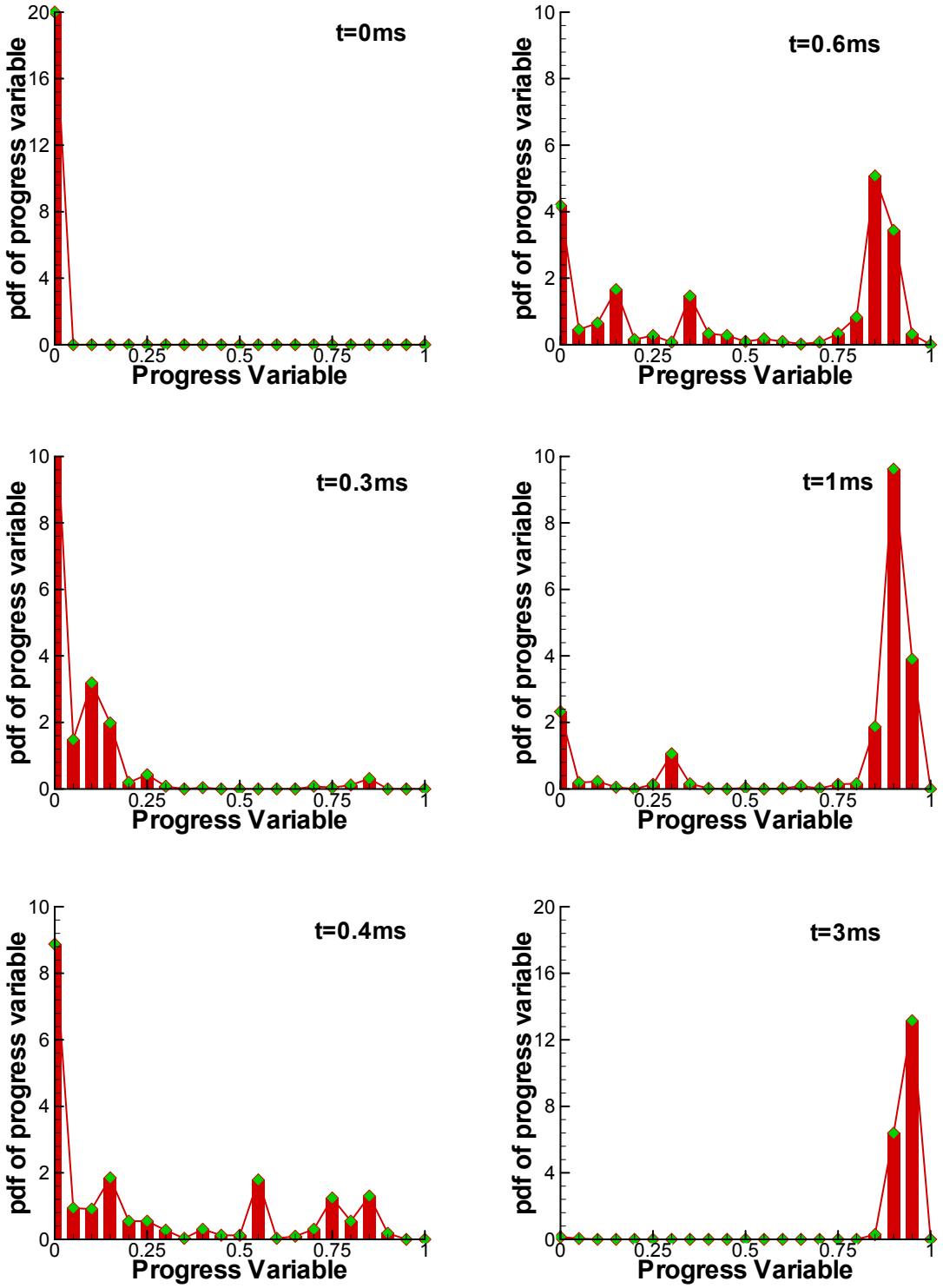

Figure 4.16 pdf of progress variables in the range of mixture fraction $0.4<\xi<0.6$

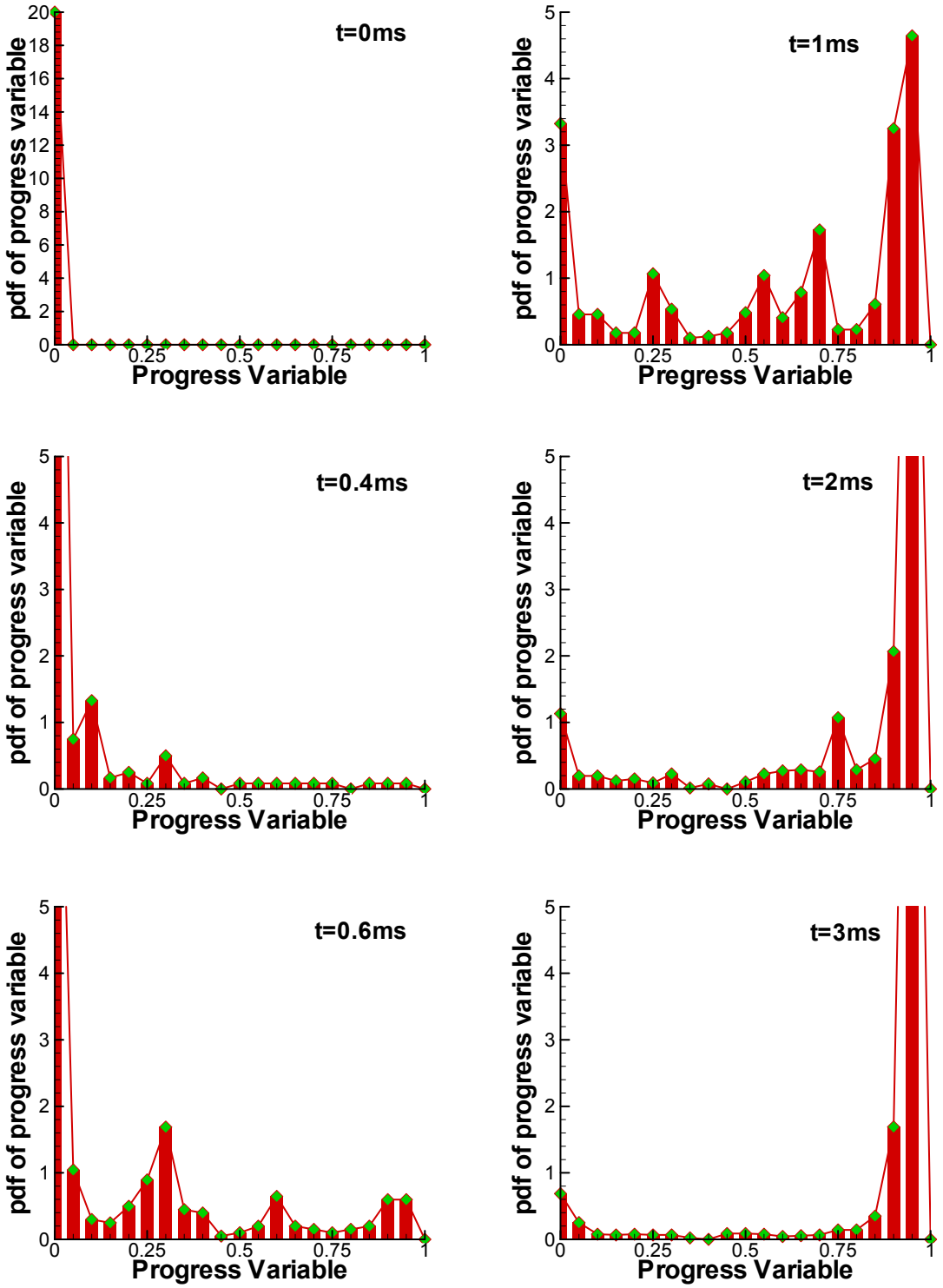

Figure 4.17 pdf of progress variables in the range of mixture fraction $0.6<\xi<0.8$

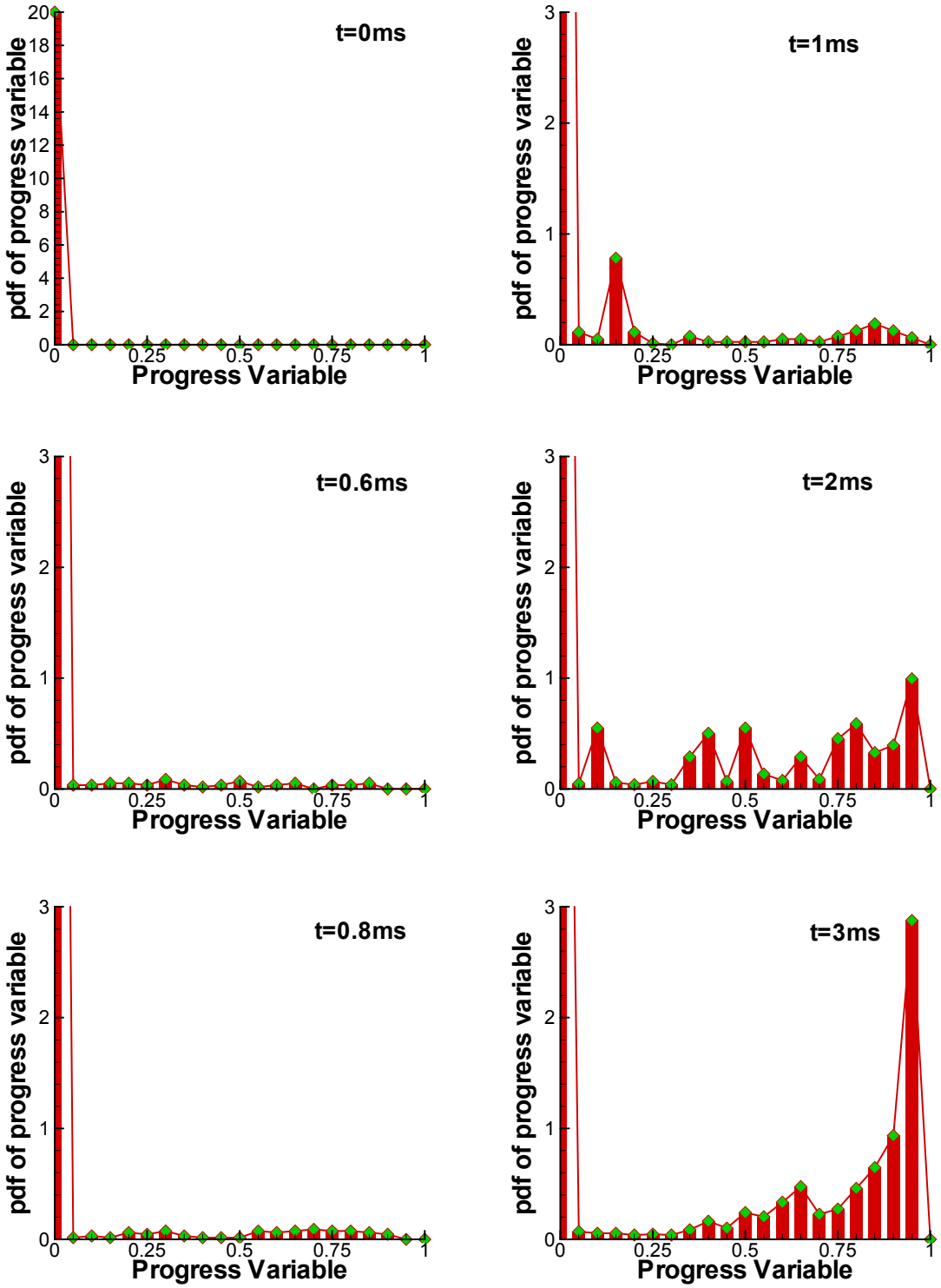

Figure 4.18 pdf of progress variables in the range of mixture fraction 0.8<ξ<1

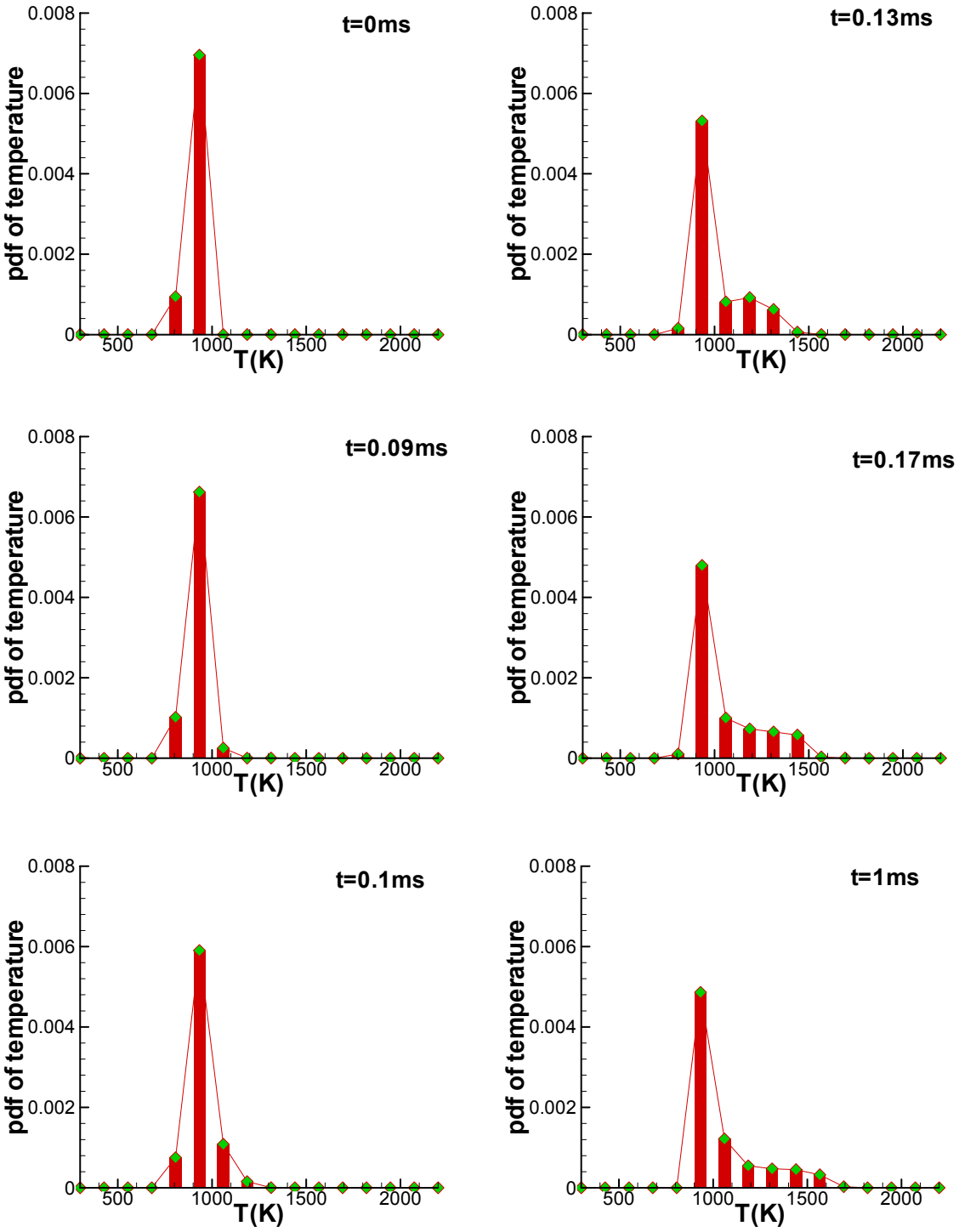

Figure 4.19 pdf of temperature in the range of mixture fraction $0<\xi<0.2$

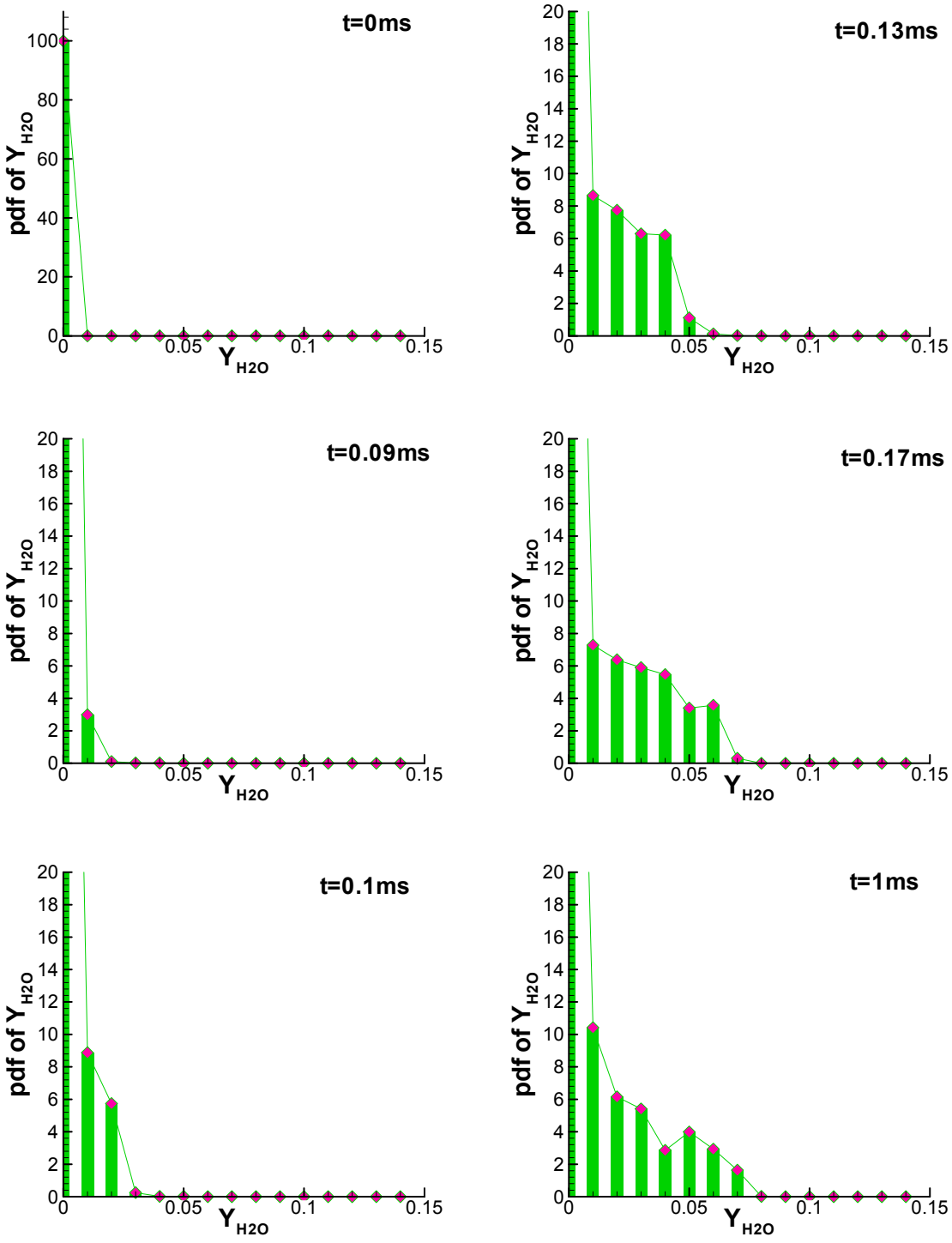

Figure 4.20 pdf of H_2O mass fraction in the range of mixture fraction $0<\xi<0.2$

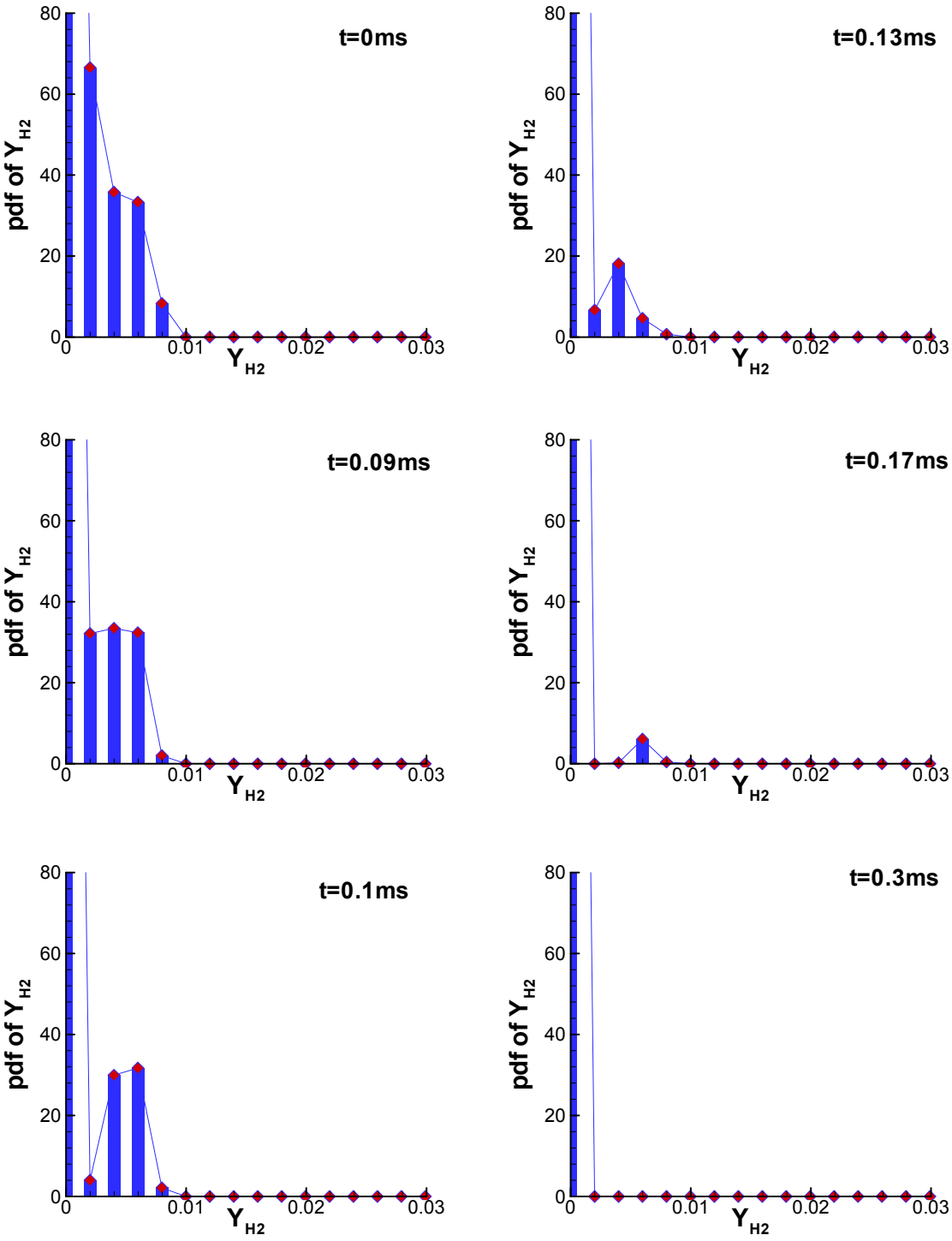

Figure 4.21 pdf of H_2 mass fraction in the range of mixture fraction $0<\xi<0.2$

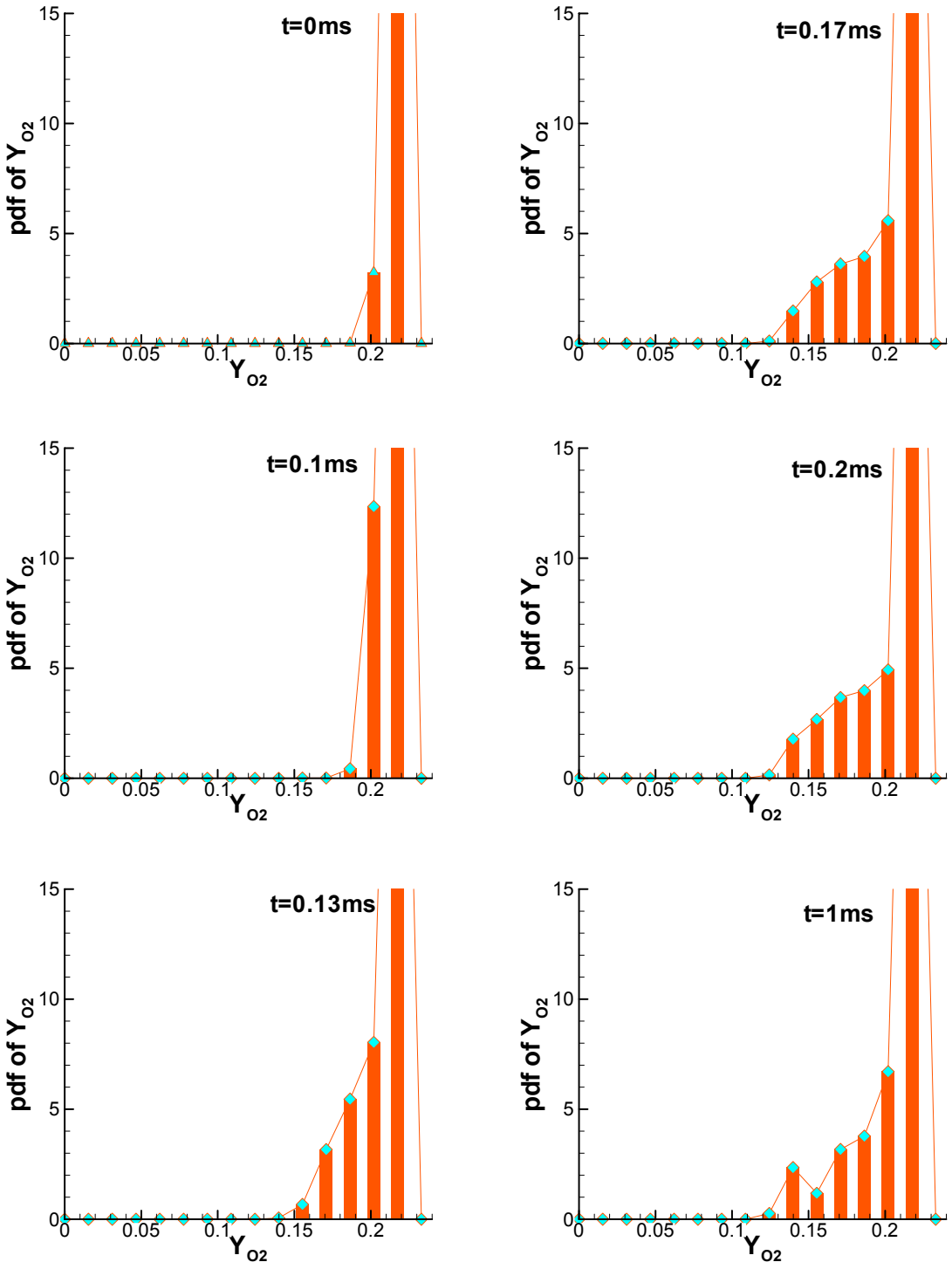

Figure 4.22 pdf of O_2 mass fraction in the range of mixture fraction $0<\xi<0.2$

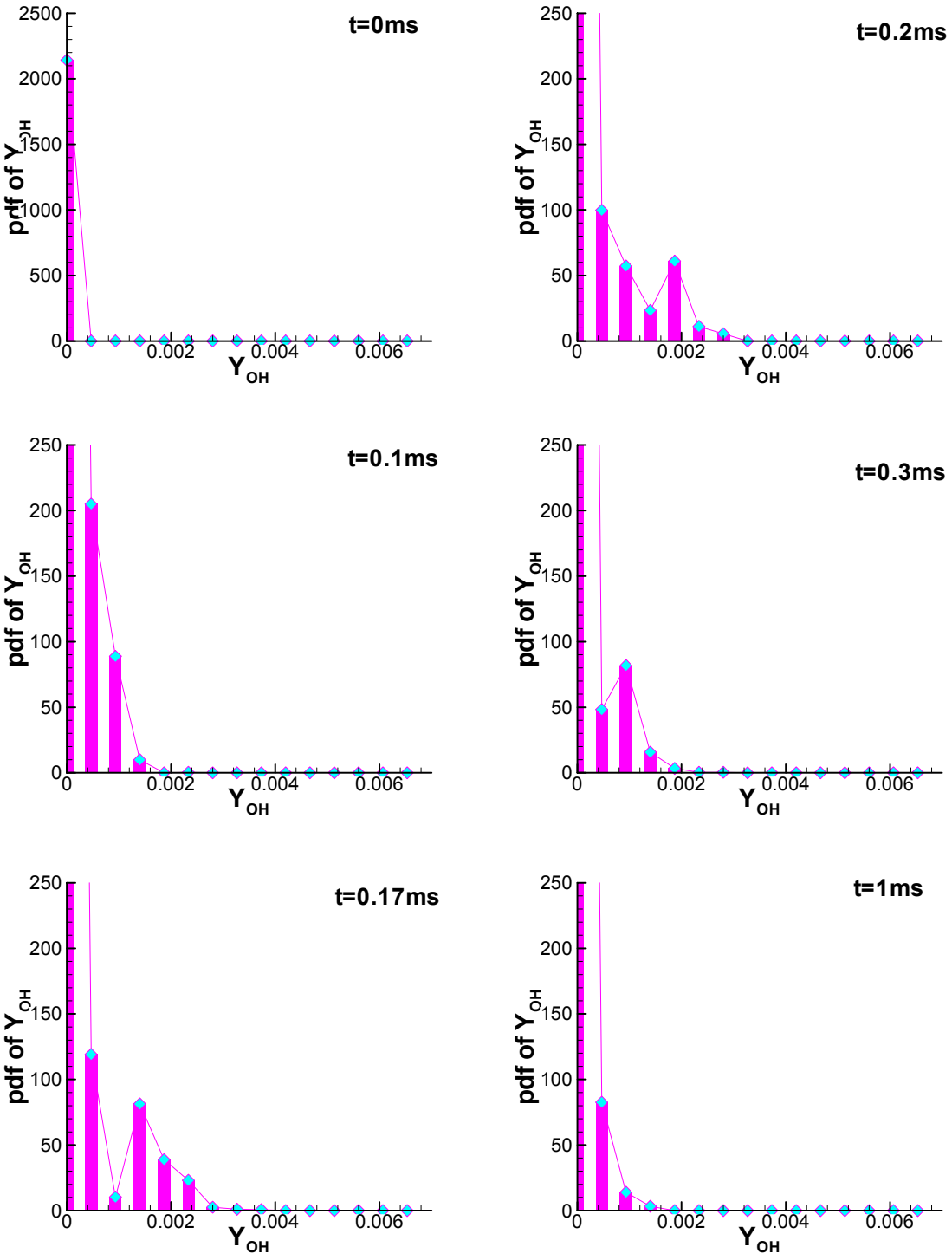

Figure 4.23 pdf of OH mass fraction in the range of mixture fraction $0<\xi<0.2$

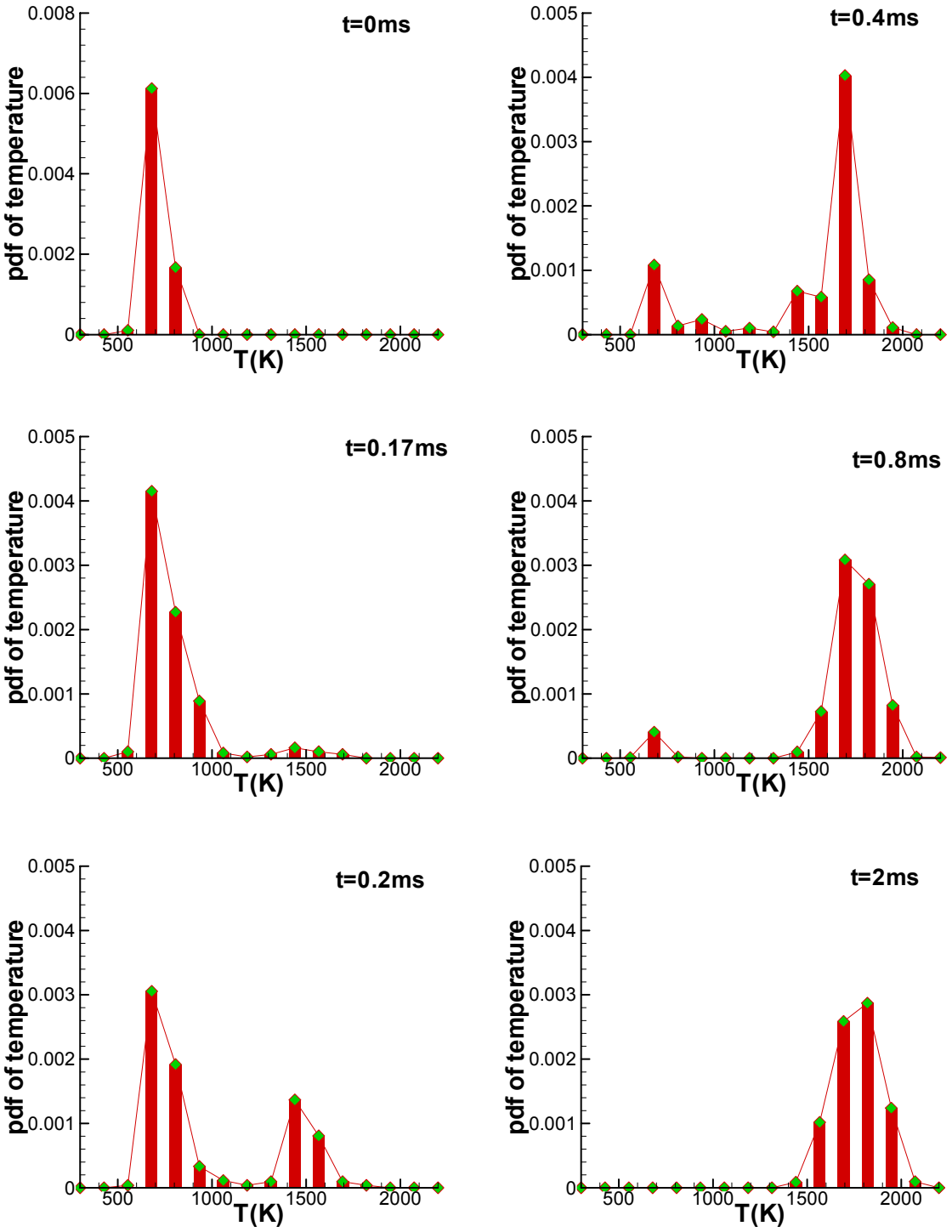

Figure 4.24 pdf of temperature in the range of mixture fraction $0.2<\xi<0.4$

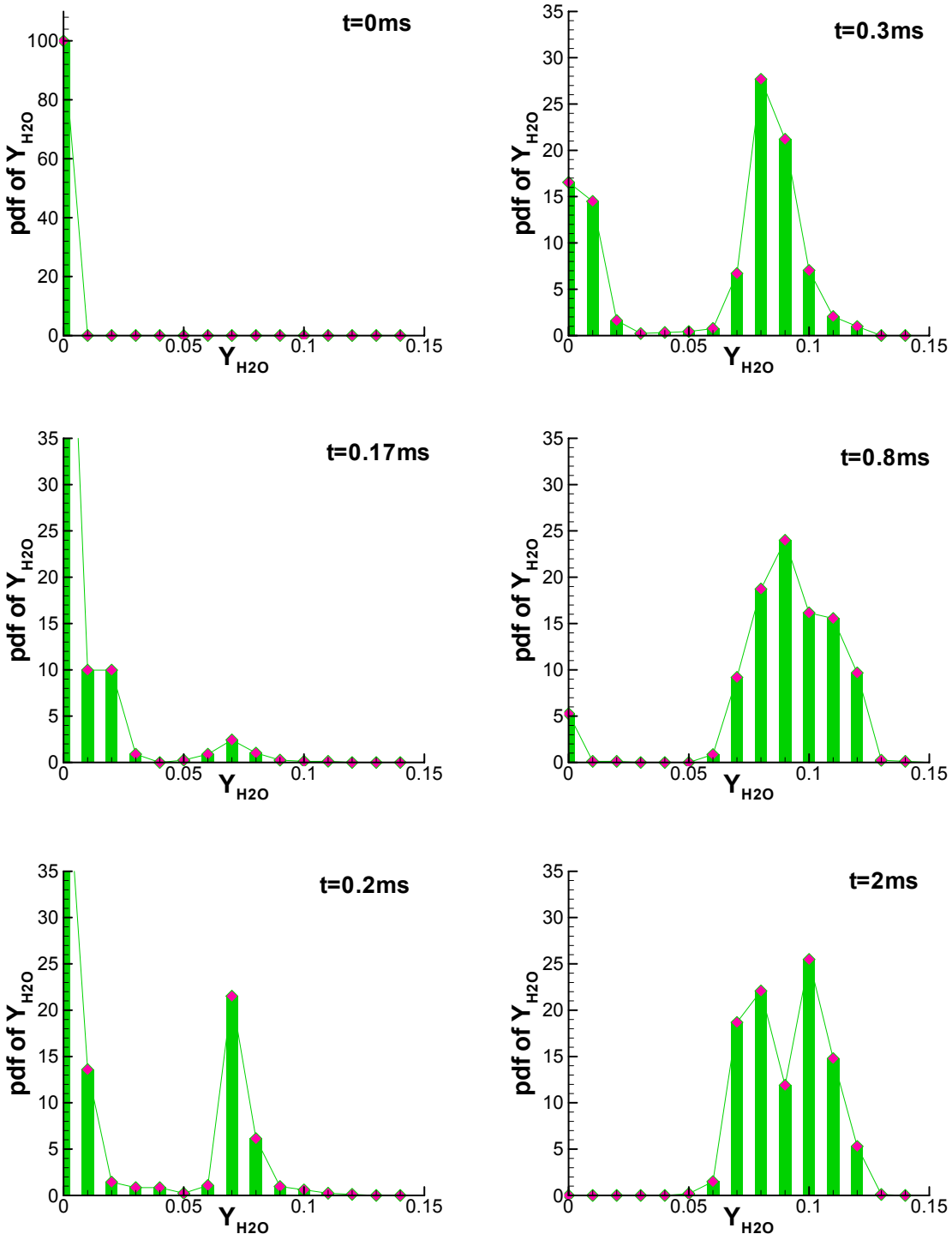

Figure 4.25 pdf of H_2O mass fraction in the range of mixture fraction $0.2<\xi<0.4$

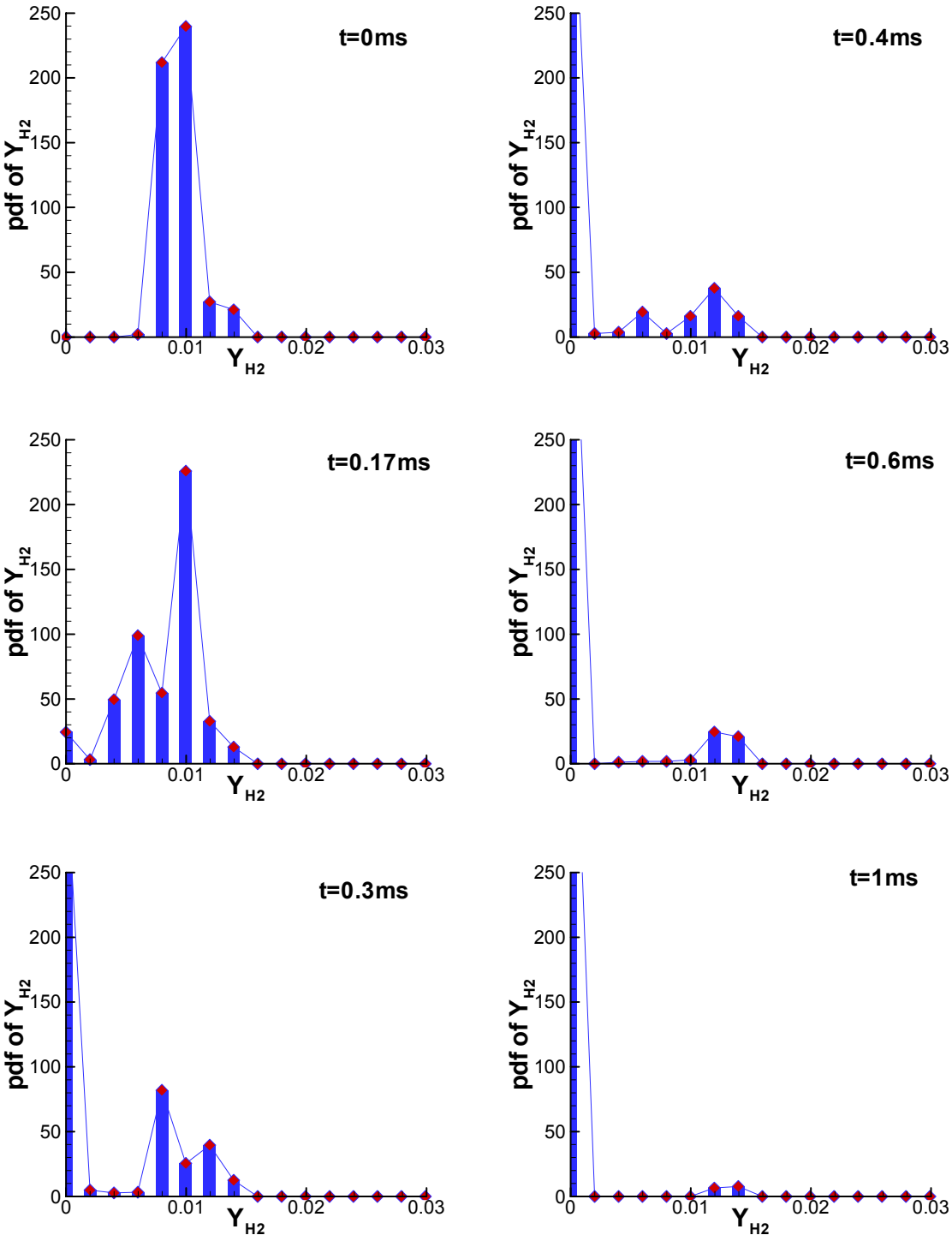

Figure 4.26 pdf of H_2 mass fraction in the range of mixture fraction $0.2<\xi<0.4$

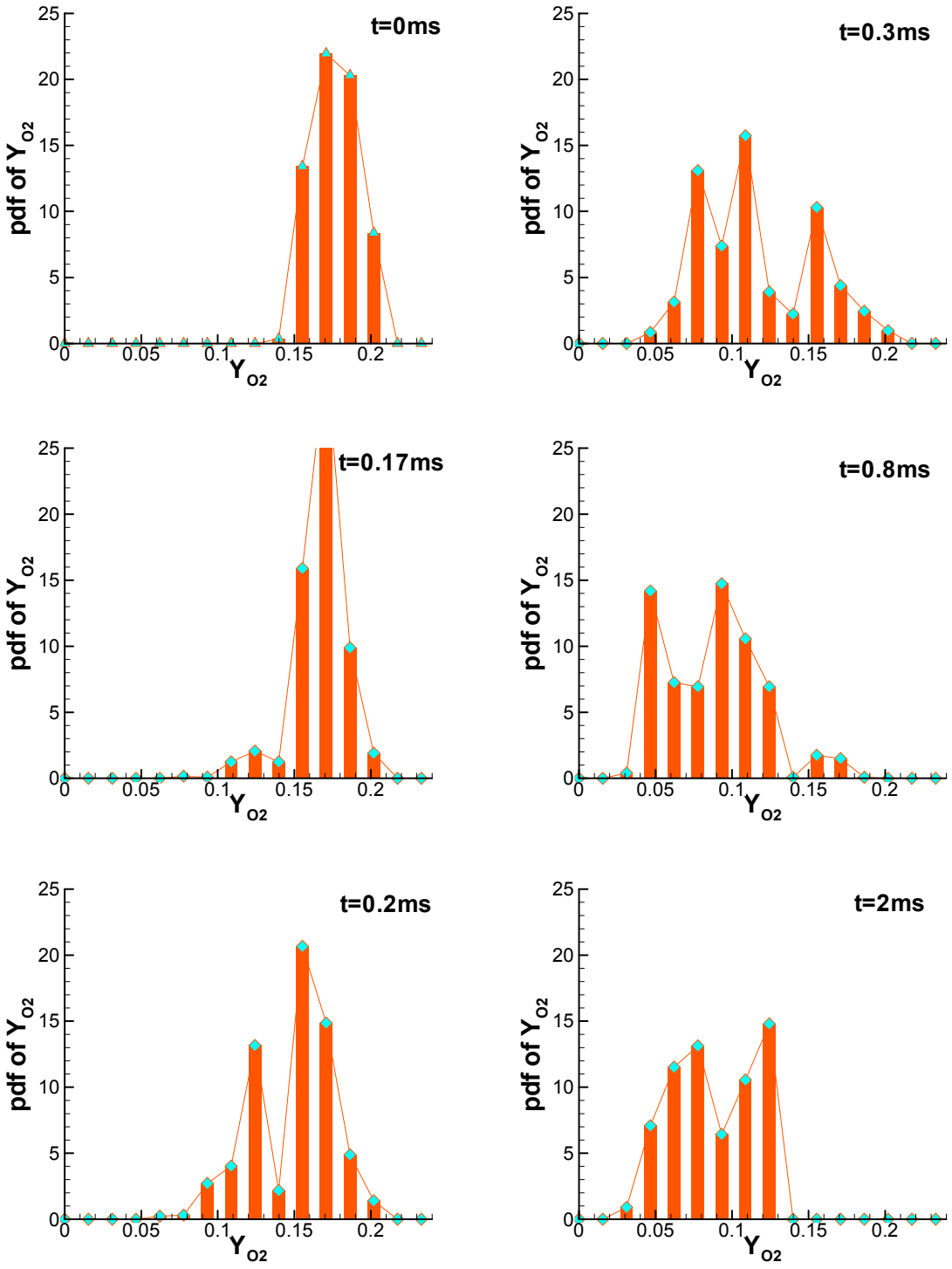

Figure 4.27pdf of O_2 mass fraction in the range of mixture fraction $0.2<\xi<0.4$

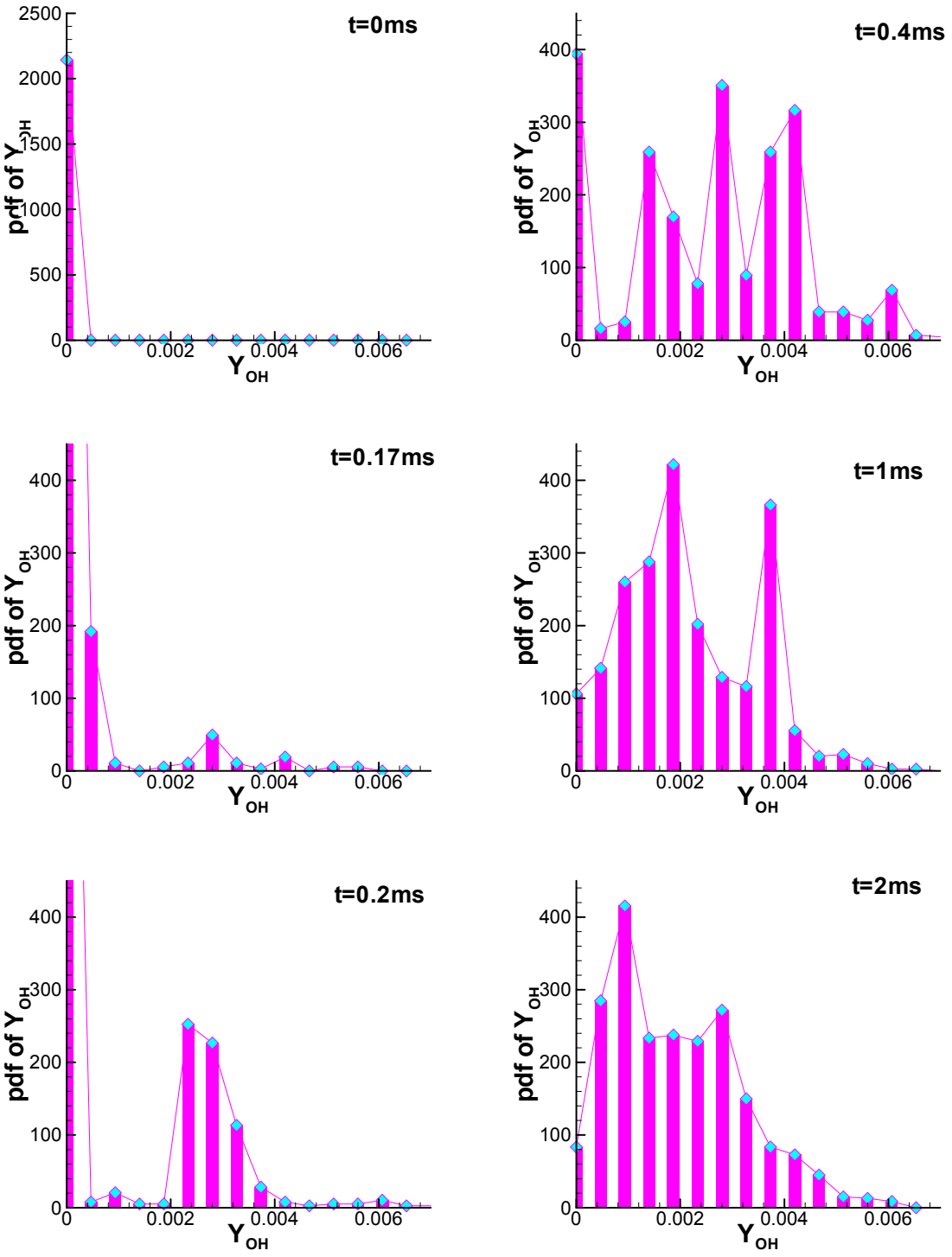

Figure 4.28 pdf of OH mass fraction in the range of mixture fraction $0.2<\xi<0.4$

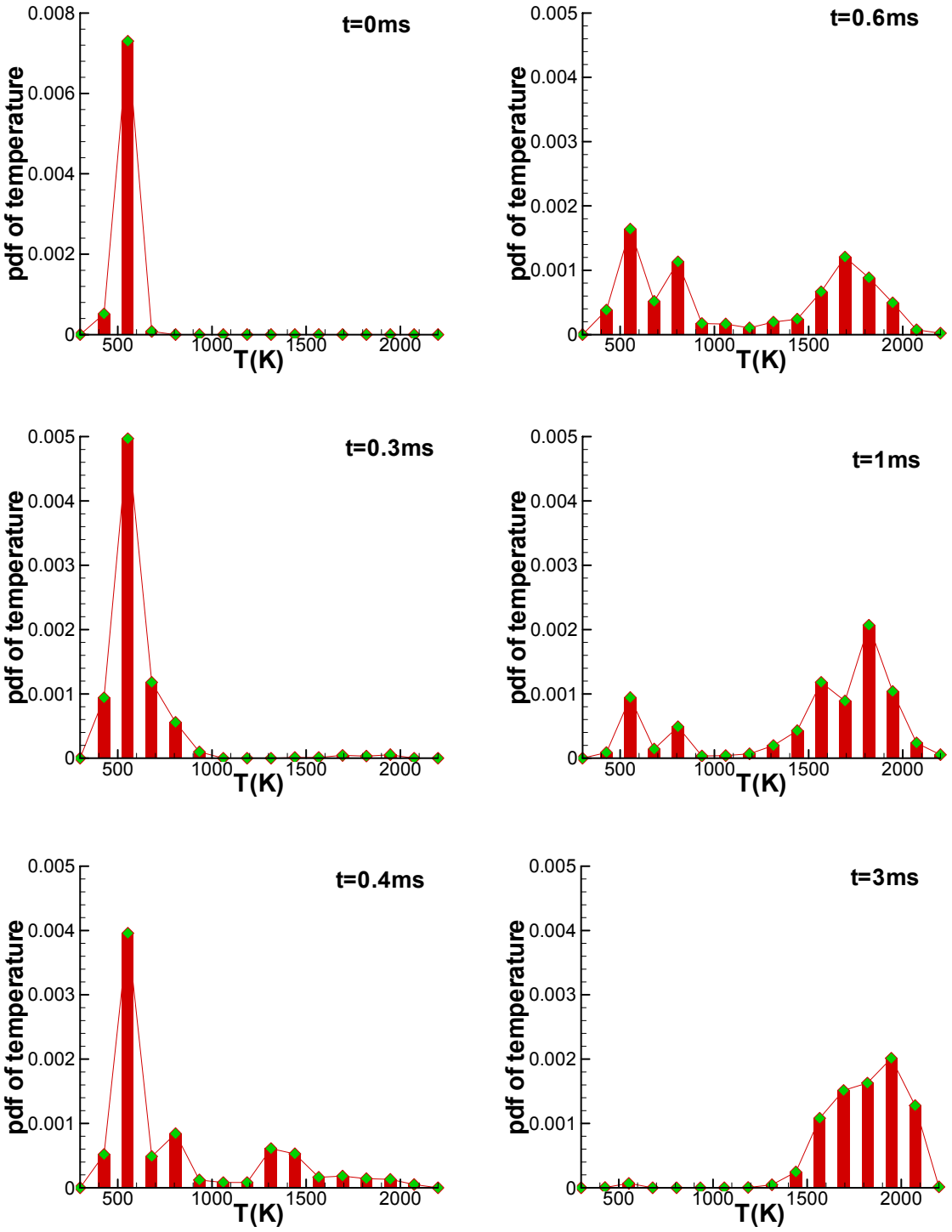

Figure 4.29 pdf of temperature in the range of mixture fraction $0.4<\xi<0.6$

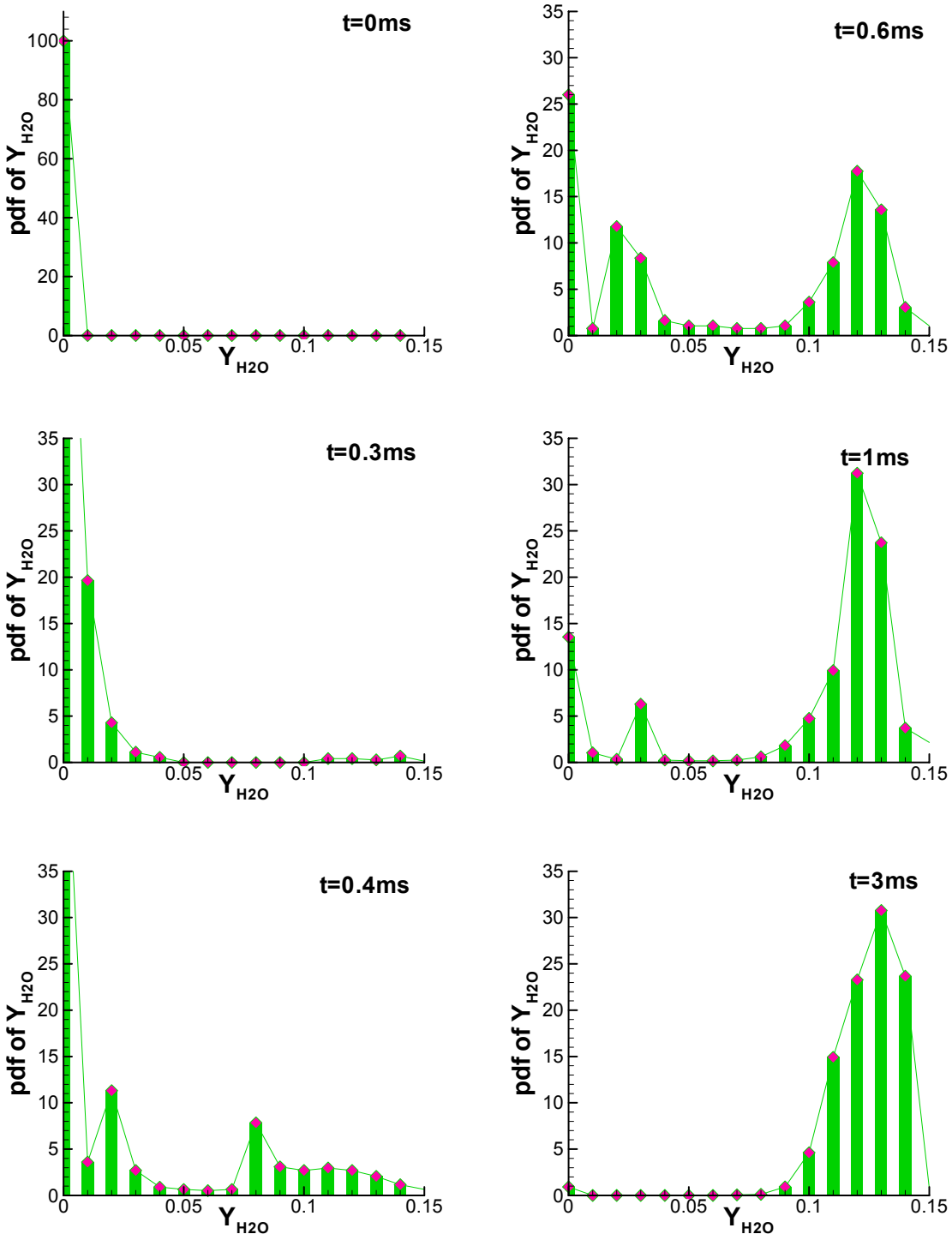

Figure 4.30 pdf of H_2O mass fraction in the range of mixture fraction $0.4<\xi<0.6$

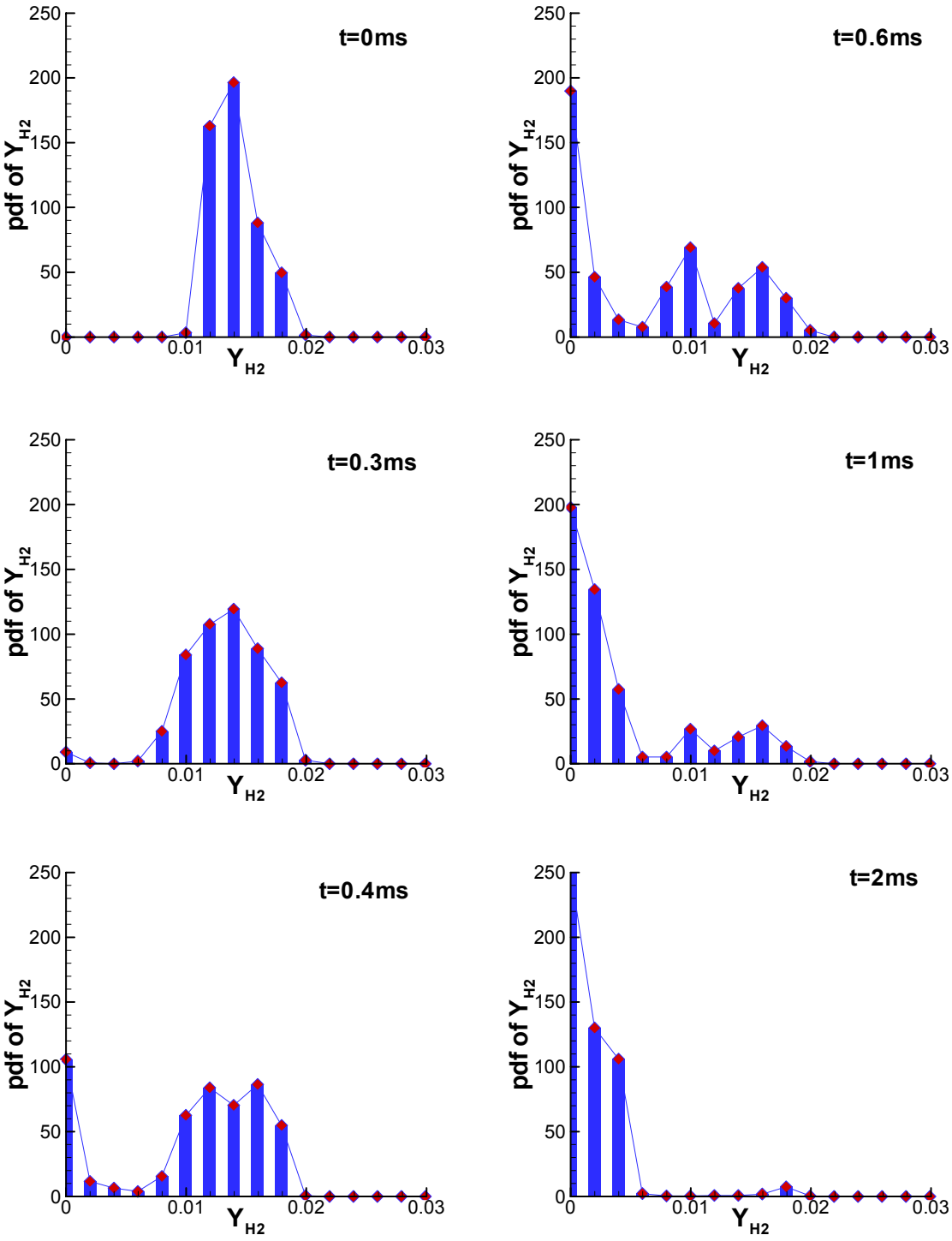

Figure 4.31 pdf of H_2 mass fraction in the range of mixture fraction $0.4<\xi<0.6$

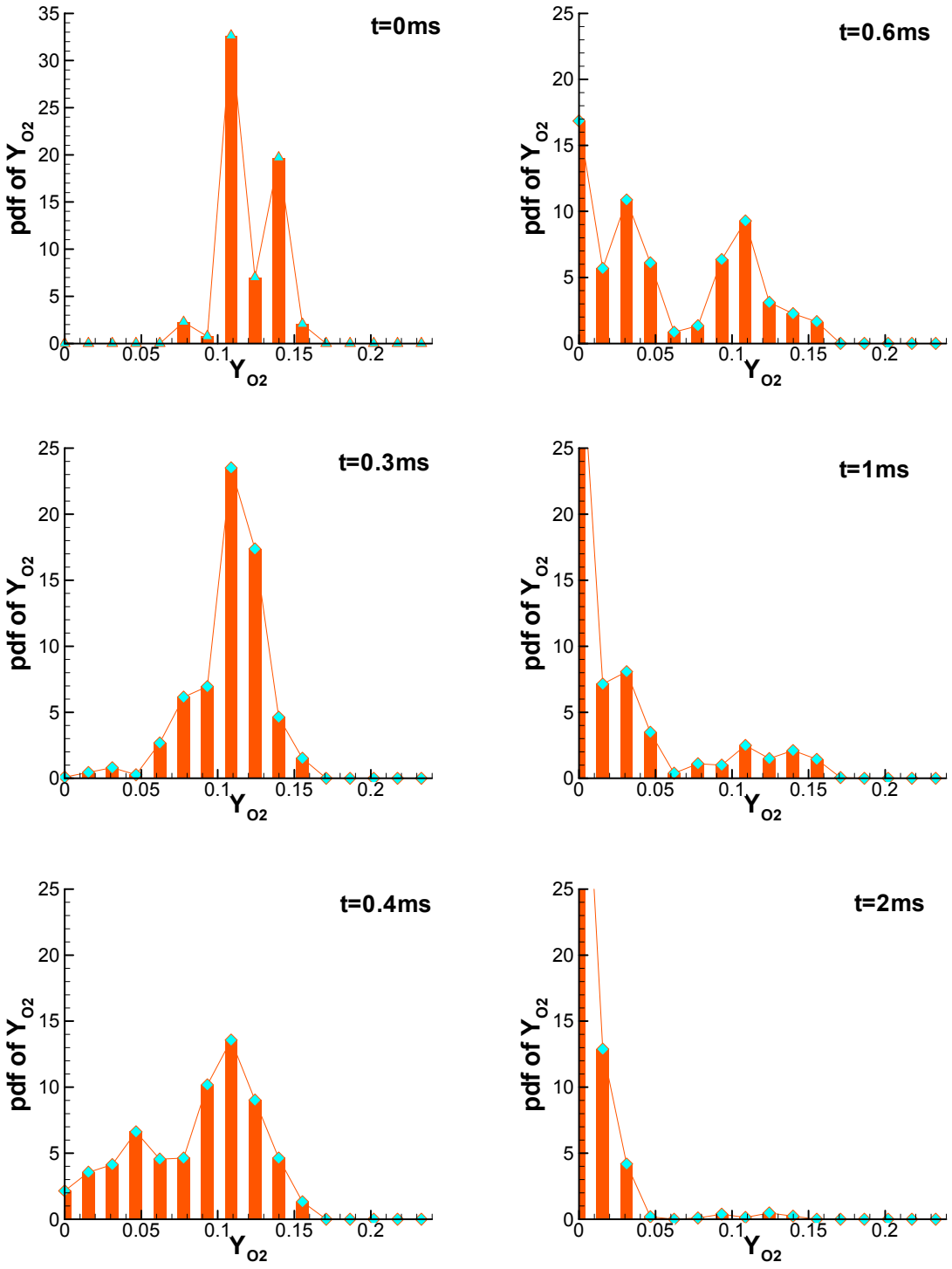

Figure 4.32 pdf of O_2 mass fraction in the range of mixture fraction $0.4<\xi<0.6$

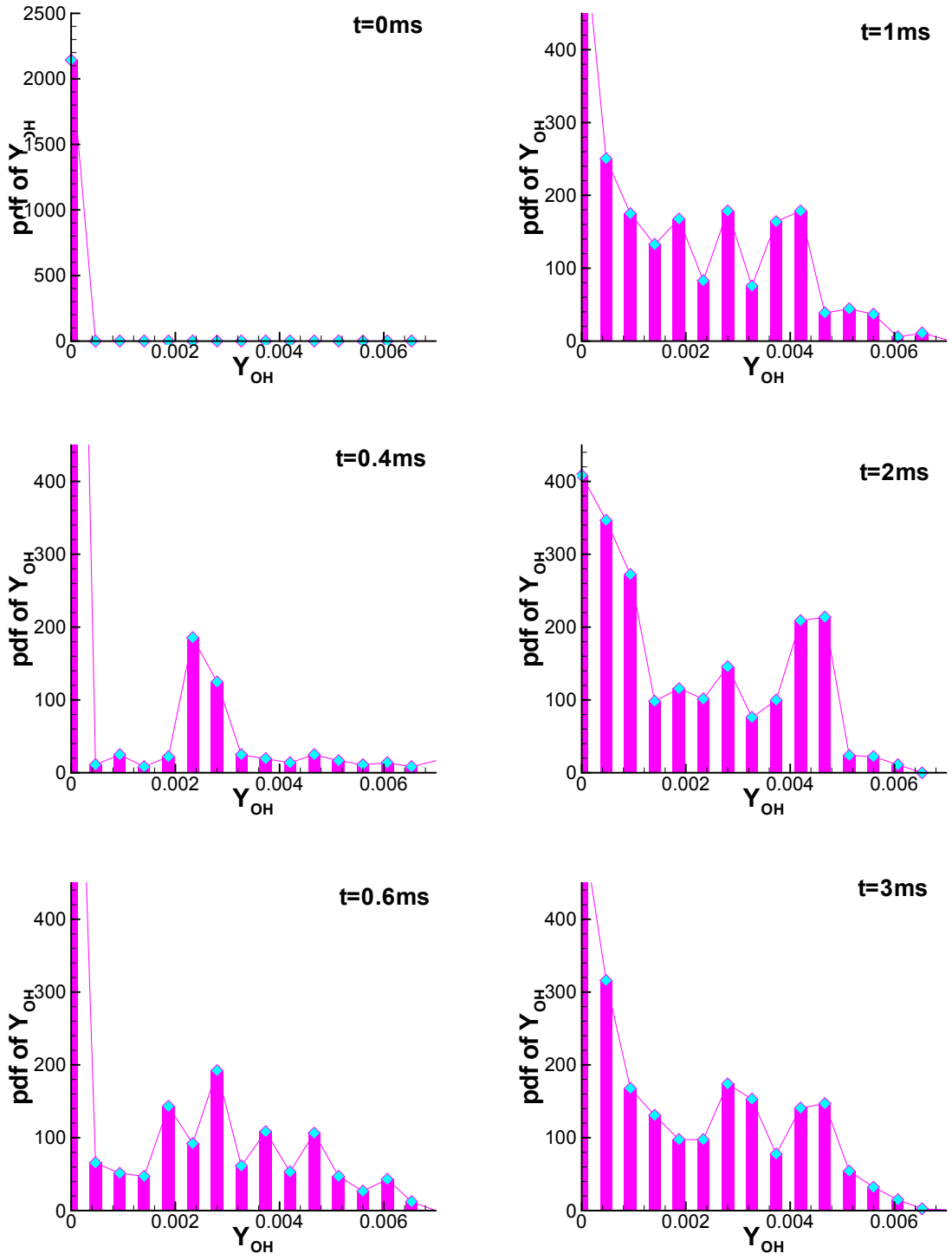

Figure 4.33 pdf of OH mass fraction in the range of mixture fraction $0.4<\xi<0.6$

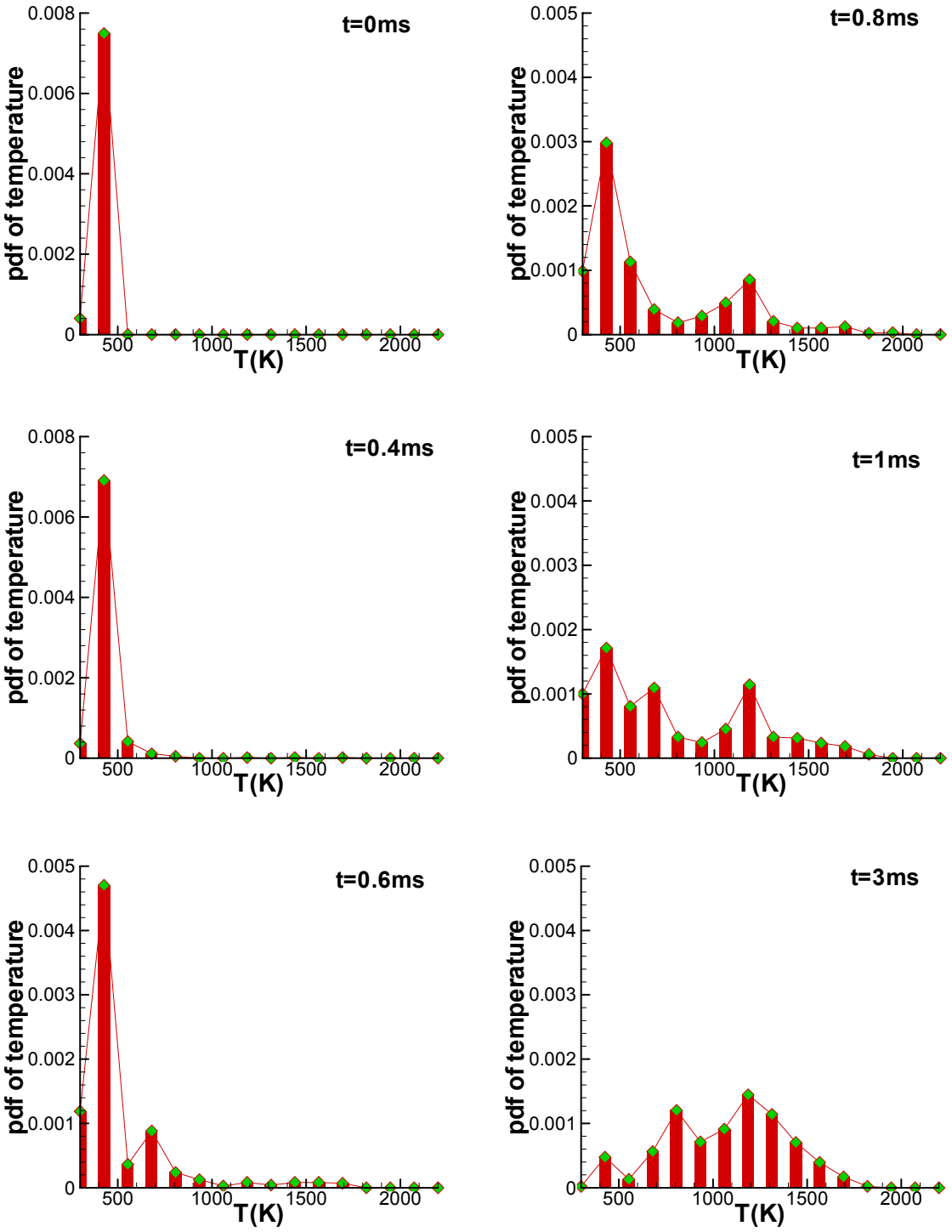

Figure 4.34 pdf of temperature in the range of mixture fraction $0.6<\xi<0.8$

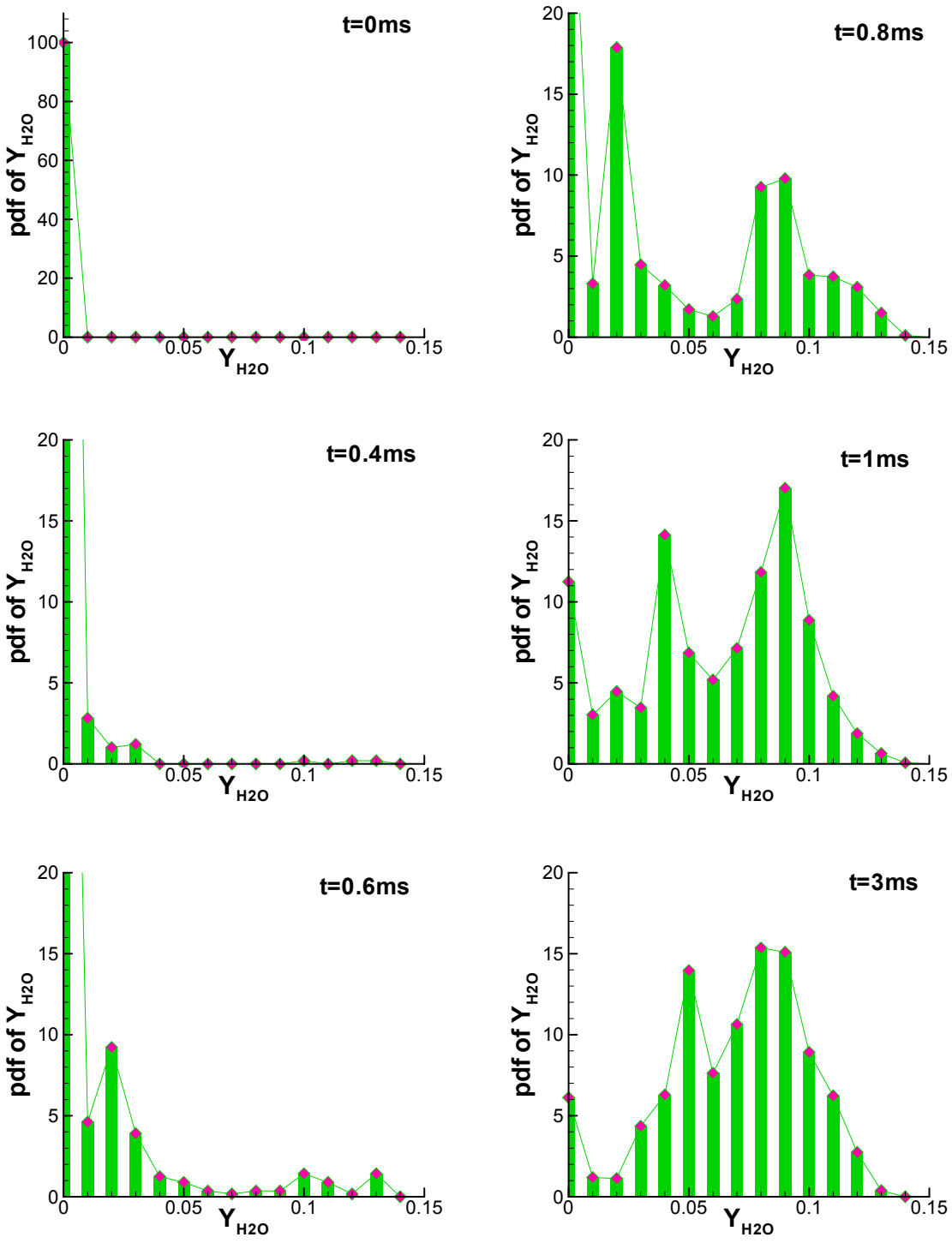

Figure 4.35 pdf of H_2O mass fraction in the range of mixture fraction $0.6<\xi<0.8$

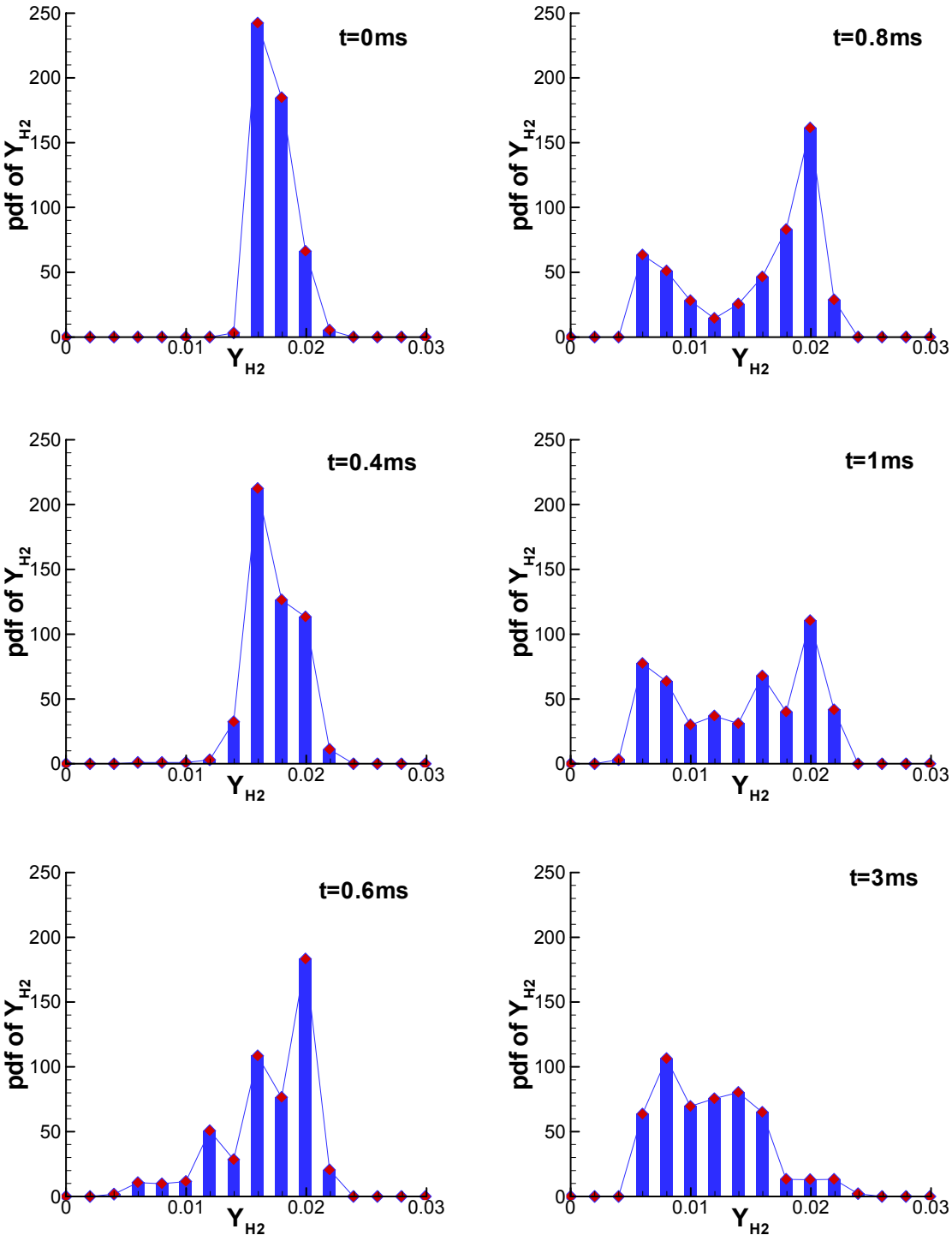

Figure 4.36 pdf of H_2 mass fraction in the range of mixture fraction $0.6<\xi<0.8$

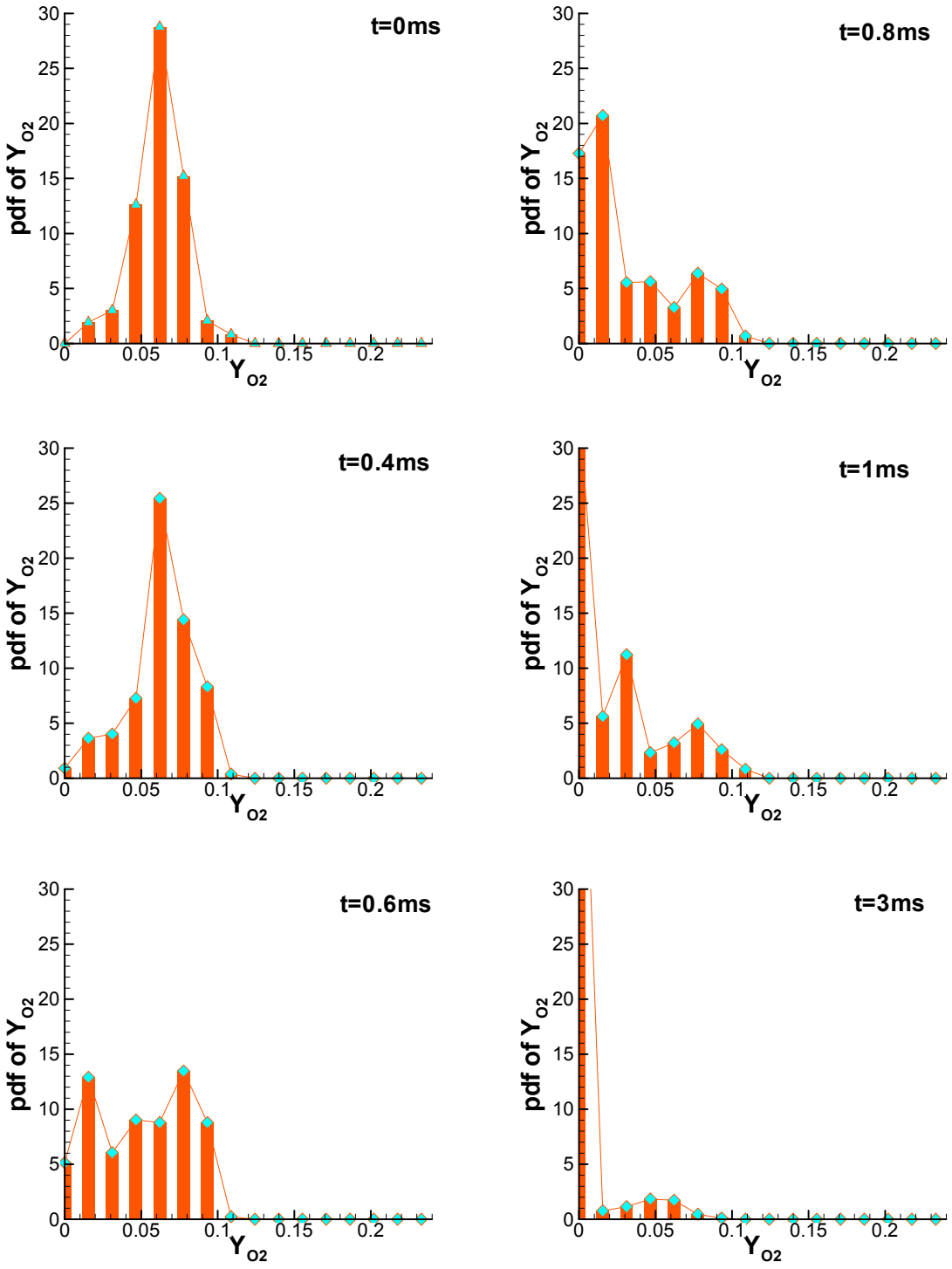

Figure 4.37 pdf of O_2 mass fraction in the range of mixture fraction $0.6<\xi<0.8$

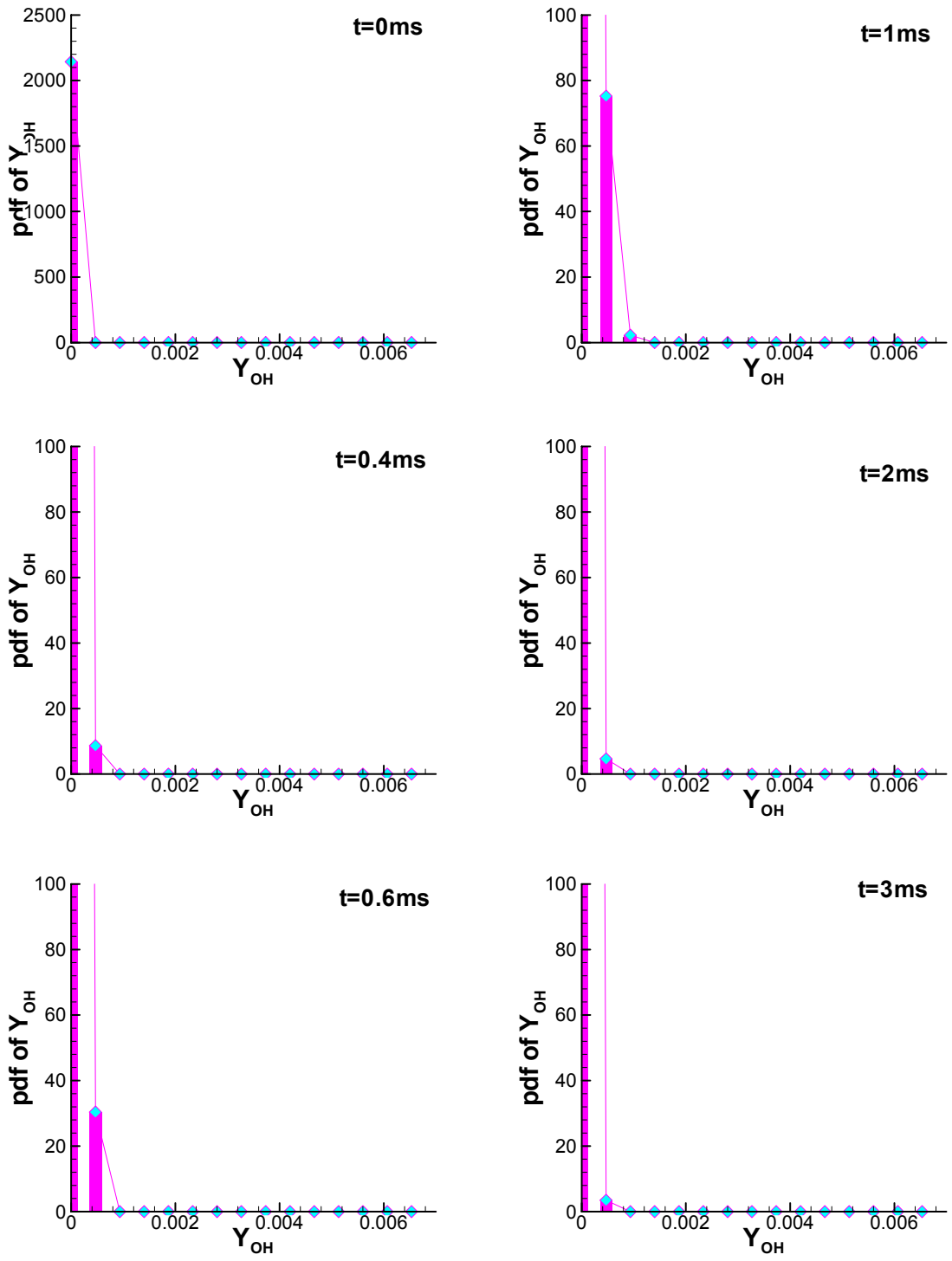

Figure 4.38 pdf of OH mass fraction in the range of mixture fraction $0.6<\xi<0.8$

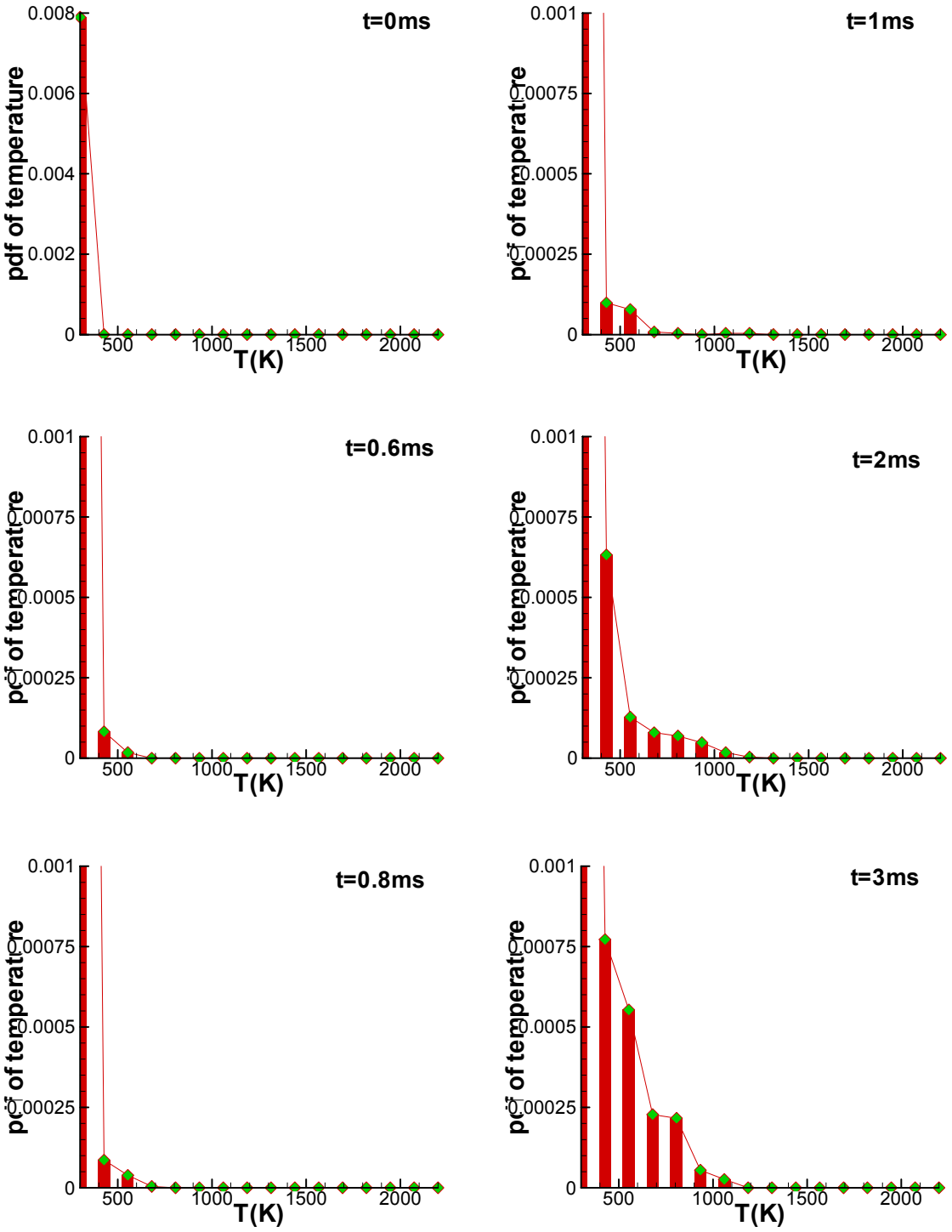

Figure 4.39 pdf of temperature in the range of mixture fraction $0.8<\xi<1$

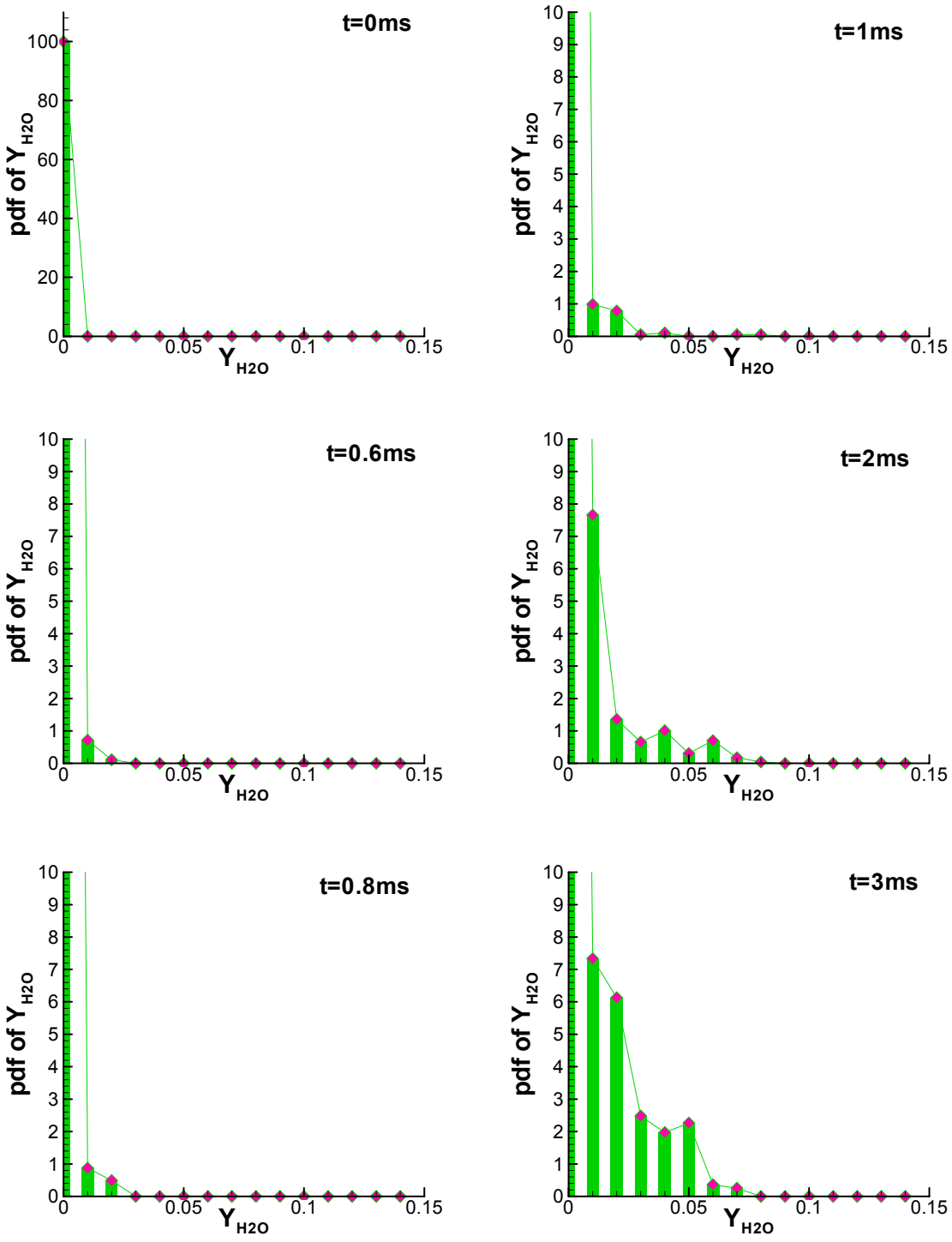

Figure 4.40 pdf of H_2O mass fraction in the range of mixture fraction $0.8<\xi<1$

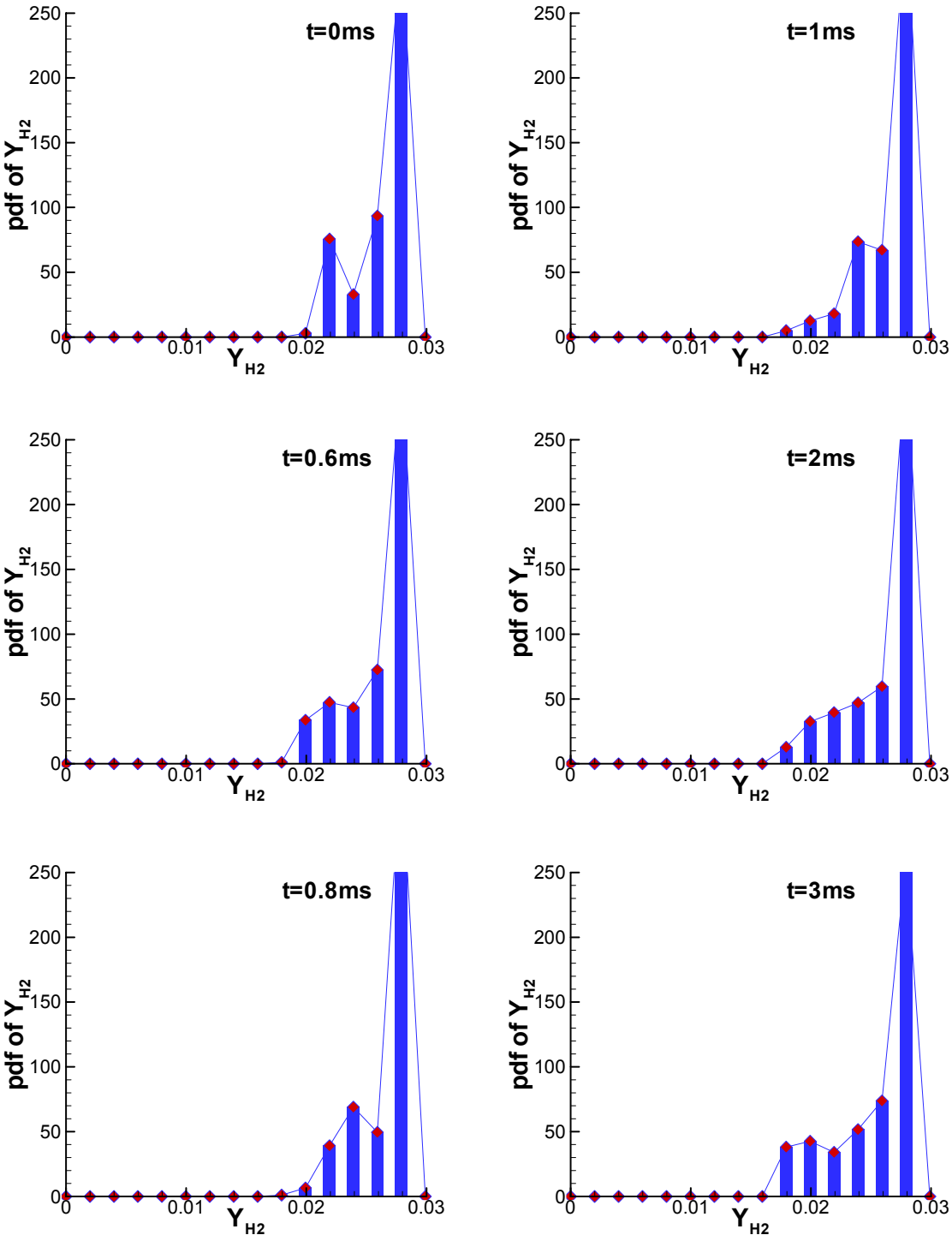

Figure 4.41 pdf of H_2 mass fraction in the range of mixture fraction $0.8<\xi<1$

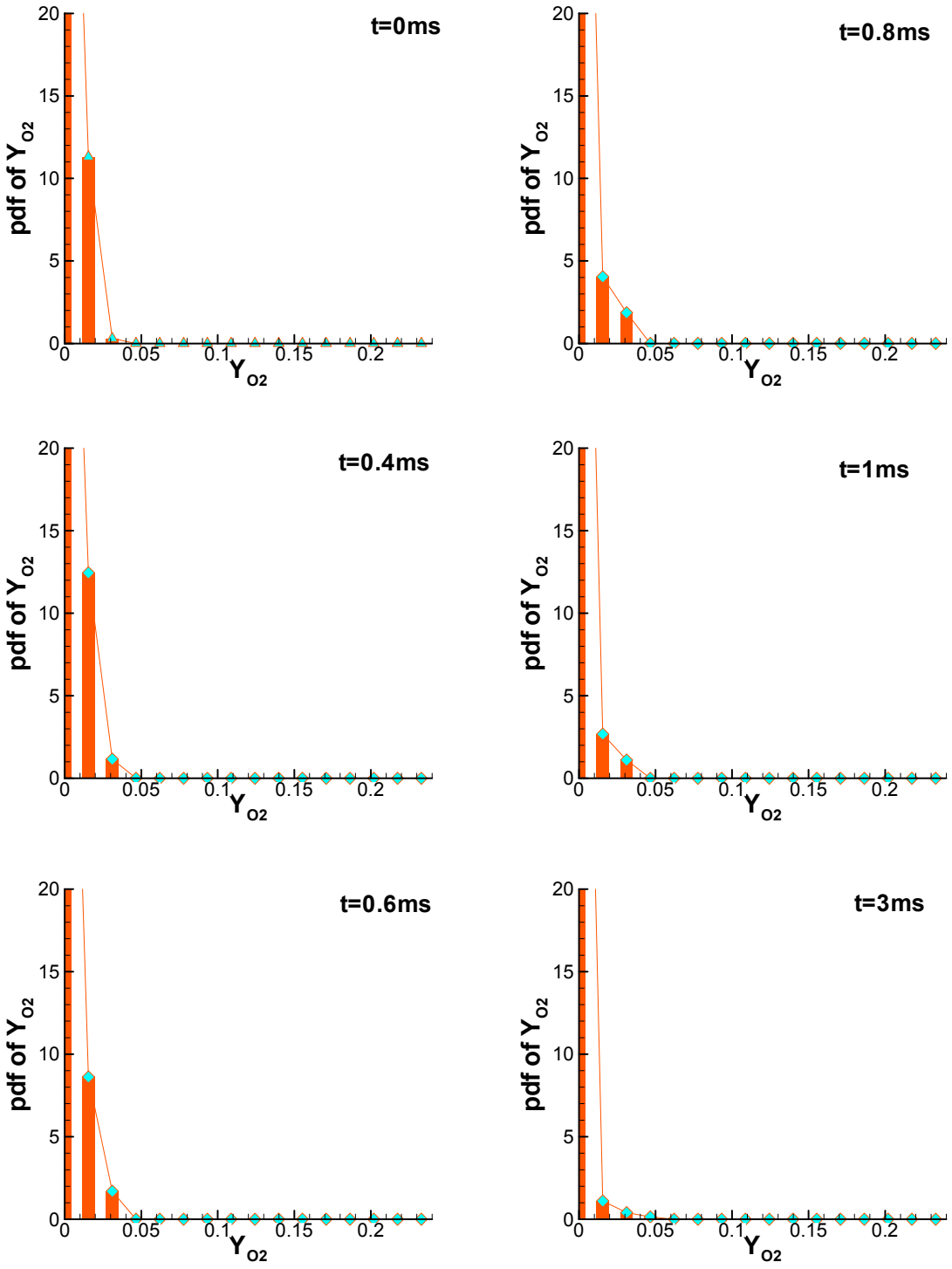

Figure 4.42 pdf of O_2 mass fraction in the range of mixture fraction $0.8<\xi<1$

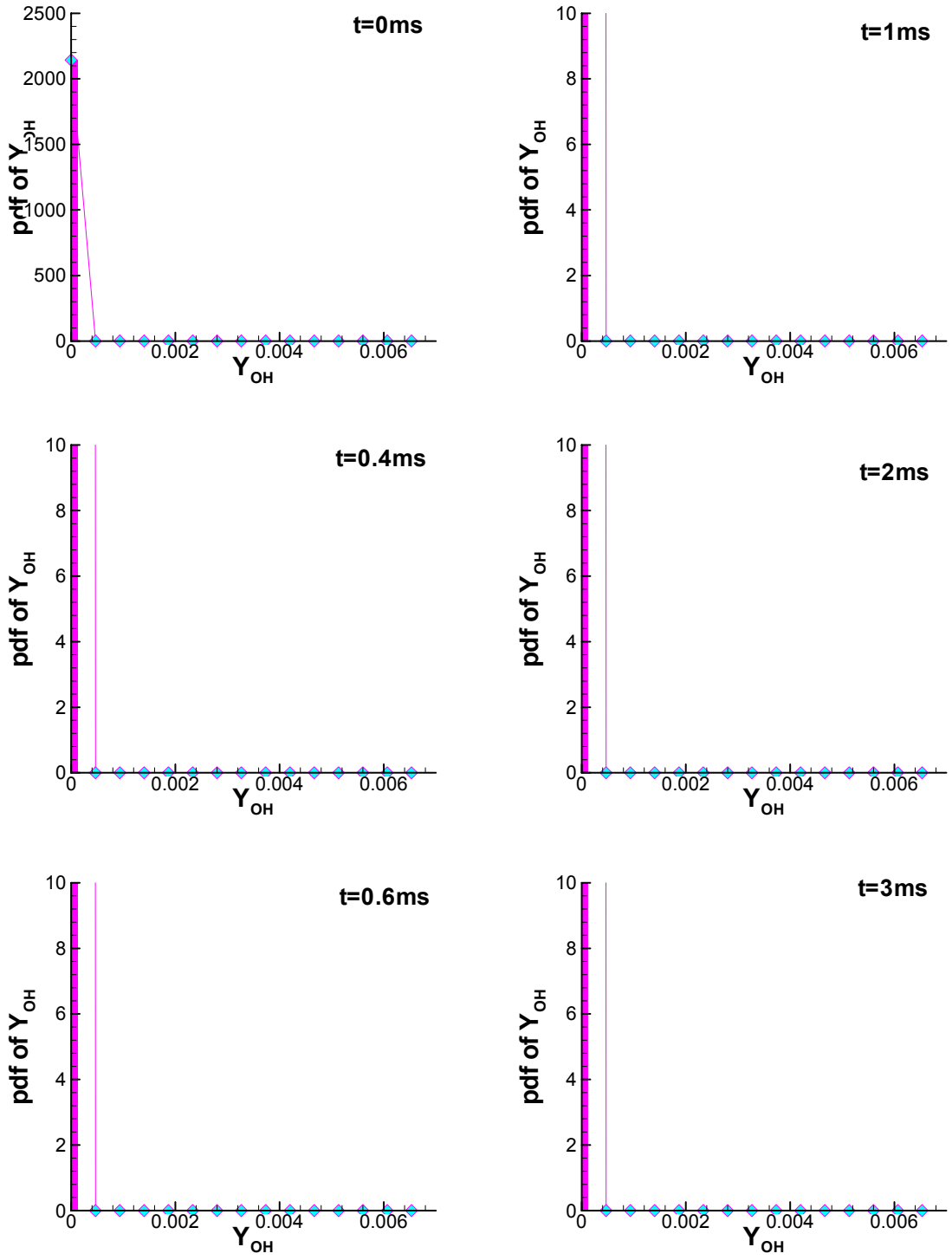

Figure 4.43 pdf of OH mass fraction in the range of mixture fraction $0.8<\xi<1$

Chapter 5

Conclusions

5.1 Finite-Rate Chemistry Effects on Jet Diffusion Flames of Hydrogen-Air with Helium Dilution

Finite-rate chemistry effects on hydrogen-air jet diffusion flames with helium dilution of the fuel stream were investigated. The numerical simulation results implemented using the One-Dimensional Turbulence model were compared with existing experimental data and reference adiabatic equilibrium conditions. Three different dilutions of the fuel stream with helium and different downstream distances were considered. Finite-rate chemistry effects are characterized by important departure from fast chemistry, equilibrium profiles, which are characteristic of reactant and product profiles in hydrogen-air flames. They are found to be most prominent in the near-field, where the flame is laminar-like and molecular diffusion is important. They are increased with the degree of helium dilution, which also results in an important reduction of flame temperatures. These effects are also more prominent for intermediates species, including the minor species NO. Here, the results show that the peak values of temperature and associated NO formation decrease with helium dilution as well.

The model shows satisfactory-to-very-good agreement with experimental data through means and rms of temperature and species statistics. Rms profiles are only available through a handful of combustion models. Computed and measured profiles of

thermochemical scalars are a strong function of degree of dilutions and flow Reynolds numbers; while, peak values of temperature and intermediate species OH and NO decrease with increased dilution volume in the fuel at the same downstream locations. Axial profiles of scalars for each flame also show their dependence on downstream conditions. OH mass fraction decreases with the downstream distance either in diluted or undiluted flames. Finite-rate chemistry effects are studied particularly in temperature profiles. Downstream locations reduce these effects, as the mixture is provided adequate time to completely burn. Near-field predictions of scalar profiles do not provide the best agreements with experimental data due to difficulty of implementing the proper inlet conditions in the computations. However, no modification of the model parameters are made for the different conditions studied; they correspond to the values adopted in earlier computations of other flames.

5.2 Finite-Rate Chemistry Effects on Autoignition of Hydrogen-Air Mixture

The problem of autoignition in non-homogeneous mixtures in turbulent flows remains a considerable challenge for both modeling and computations. During autoignition, important transitions in the dominant chemistry and the interactions between ignition kernels and turbulence result in a complex, transient evolution of the reacting mixture. Finite-rate chemistry effects are manifested in the complex dependence of the volumetric burning rate on turbulence conditions. On one hand, turbulence increases the number of interfaces separating the segregated mixtures of fuel and oxidizer. The increased number of interfaces increases the potential number of ignition kernels. However, through this intensification of

interfaces, the rate of dissipation also increases. The rate of dissipation may deplete these ignition kernels of important radicals, and may result in failed autoignition kernels. The coupling between turbulent transport and chemistry is also affected by the thermodynamic conditions, including the mixture pressure. Pressure acts to modify the rates of reactions and may favor third-body reactions to be more prominent. It also increases the rate of molecular diffusion through its effects on the diffusion coefficient.

Finite-rate chemistry effects on the autoignition process of a non-homogeneous hydrogen-air mixture in a scalar and shear-mixing (jet) layers was studied using One-Dimensional Turbulence and a detailed mechanism of Hydrogen-air chemistry. The simulations were implemented for a range of pressure and Reynolds numbers to identify the effects of turbulence intensity and mixture properties on the dominant self-ignition chemistry. To identify the proper run conditions for the mixture, homogeneous autoignition runs were also implemented. These runs results in the choice of different preheat temperatures for the oxidizer and pressure conditions that yield similar ignition delay times. Two pressure conditions were selected: 1 and 3 atmospheres. The atmospheric case yields a much broader range of mixture fractions that are characterized by similar delay times; while the homogeneous chemistry simulations at 3 atm result in a narrower corresponding range.

In non-homogeneous autoignition process, the variation in ignition delay due to the corresponding variation in turbulence intensity is found to be non-monotonic. Turbulent events can increase the ignition kernels, which propagate after ignition; but at the same time, too many kernels delay ignition by the mutual annihilation (merger) of the different

propagating ignition fronts each. So the overall influence of turbulent stirring events on ignition delay is quite small. However, the ignition delay time is observed to be strongly associated with pressure for non-homogeneous autoignition, where transport contributes to both the dissipation of turbulence (i.e. its decay downstream of the inlet of the jet) and dissipation of ignition kernels (through increased molecular diffusion of intermediate species characterizing the radical pool). The higher pressure within the second ignition limit corresponds to a longer ignition delay time at the same or even higher initial temperature conditions. It is because higher pressure will increase the heat release rate and differential diffusion to dissipate more radical pool, while it results in higher viscosity, which dissipates more turbulence.

The local peak value of temperature is shown to increase with time during autoignition and the subsequent high-temperature combustion process, which is characterized by heat release and increases in temperature. As ignition progresses from relatively lean mixtures to richer mixtures, the peak of the temperature conditional (based on the mixture fraction) mean while shifts towards stoichiometric conditions. The ignition kernels always occur first at the higher temperatures at fuel-lean conditions. However, the maximum temperature product and intermediate species are observed at stoichiomtric conditions at later times. A progressive evolution from pure mixing behavior to burnt conditions evolves from lean to richer mixtures.

Additional characteristics of the ignition process have been identified through additional statistics based on conditional pdf's of the reaction progress variable, temperature, and species.

Reference

Balakrishnan, G., Smooke, M. D. and Williams, F. A., *Combust. Flame* 102: 329-340 (1995)

Barlow, R. S. and Carter, C. D., *Combust. Flame* 97: 261-280 (1994).

Barlow, R. S. and Carter, C. D., *Combust. Flame* 104: 288-299 (1996).

Barlow, R. S., Smith, N. S. A., Chen, J.–Y. and Bilger, R. W., *Combust. Flame* 117: 4-31 (1999).

Barlow, R. S., Sandia H2/H3 Flame Data – Release 2.0, http://www.ca.sandia.gov/TNF, Sandia National Laboratories (2003).

Bikas, G. and Peters, N., *Combust. Flame* 126: 1456-1475 (2001).

Bilger, R. W., Starner, S. H. and Kee, R.J., *Combust. Flame* 80: 135-149 (1990).

Blouch, J. D. and Law, C. K., *Combust. Flame* 132: 512-522 (2003).

Brown, P. N., Byrne, G. D. and Hindmarsh, A. C., *SIAM J. Sci. Stat. Comput.* 10: 1038-1051 (1989).

Bushe, W. K. and Steiner, H., *Phys. Fluids*, Vol. 11, No. 7 (1999).

Cain, T. M., *Combust. Flame* 111: 124-132 (1997).

Chekholv, A. and Yakhot, V., *Phys. Rev.* E **51**, R2739-R2742. (1995).

Chen, J.-Y., Chang, W.-C. and Koszyknwski, M., *Combust. Sci. Tech*., 110-111: 505-529 (1995).

Colucci, P. J., Jaberi, F. A. and Givi P., *Phys. Fluids*, Vol. 10, No. 2 (1998).

Constantin, P., Lax, P. D. and Majda, A., *Commun. Pure Appl. Math.* **38**, 715-724. (1985).

Cook, A. W., Riley, J. J. and Kosály, G., *combust. Flame* 109: 332-341 (1997).

De Gregorio, S., *J. Stat. Phys.* **59**, 1251-1263 (1990).

Desjardin, P. E. and Frankel, S. H., *Combust. Flame* 104: 343-357 (1996).

Desjardin, P. E. and Frankel, S. H., *Combust. Flame* 109: 471-487 (1997).

Echekki, T., Kerstein, A.R., Dreeben, T.D., and Chen, J.Y., *Combust. Flame* 125: 1083 (2001).

Echekki, T. and Chen, J. H., *Combust. Flame* 134 (2003).

Echekki, T., Kerstein, A. R. and Chen, J. Y., *Proceedings of the Third Joint Meeting of the U.S. Sections of the Combustion Institute*, Chicago, March 16-19, 2003.

Hilbert, R. and Thévenin, D., *Combust. Flame* 128: 22-37 (2002).

IM, H. G., Chen, J. H., and Law, C. K., *Twenty-Seventh Symposium (International) on Combustion/The Combustion Institute*, pp.1047-1056(1998).

Kee, R. J., Miller, J. A. and Jefferson, T. H., Sandia National Laboratories Report SAND83-8209 (1983).

Kee, R. J., Warnatz, J. and Miller, J. A., Sandia National Laboratories Report SAND 83-8209 (1983).

Kee, R. J., Grcar, J. F., Smooke, M. D. and Miller, J. A., Sandia National Laboratories Report SAND85-8240 (1985).

Kerstein, A. R., *Combust. Flame* 75: 397-413 (1989).

Kerstein, A. R., *Combst. Sci. and Tech.* **60**, 391-421 (1988)

Kerstein, A. R., *Phys. Fluids A* 3(5): 1110-1114 (1991A).

Kerstein, A. R., *J. fluid Mech.* 231:361-394 (1991B).

Kerstein, A. R., *J. Fluid Mech.* 240: 289-313 (1992).

Kerstein, A. R., *J. fluid Mech.* 392:277-334 (1999A).

Kerstein, A. R., *Dyn. Atmos. Oceans* 30(1): 25-46 (1999B).

Kops, S. M. de B. and Riley, J. J., *Proceedings of 1999 ASME/JSME Fluids Engineering Division Summer Meeting* July 18-23, 1999, San Francisco, California, USA.

Kreutz, T. G. and Law, C. K., *Combust. Flame* 104: 157-175(1996).

Libby, P. A. and Williams, F. A. *Turbulent Reacting Flows*, Academic Press Inc, San Diego CA, 1994.

Lutz, A. E., Kee, R.J., Grcar, J. F., and Rupley, F. M., Sandia National Laboratories Report SAND 96-8243 (1996).

Mastorakos, E., Baritaud, T. A., and Poinsot, T. J., *Combust. Flame* 109: 198-223 (1997).

McMurtry, P. A., Menon, S. and Kerstein, A. R., *Proceedings of the 24th Symposium (International) on combustion* (The combustion Institute, Pittsburgh, 1992), p. 271.

Peters, N., *Turbulent Combustion*, Cambridge University Press, Cambridge, 2000.

Zhang, S. and Echekki, T., *Proceedings of the Third Joint Meeting of the U.S. Sections of the Combustion Institute*, Chicago, March 16-19, 2003.